ADVANCED OPTICAL MATERIALS
www.advopticalmat.de

Recent Advances in Solid-State Lighting Devices Using Transition Metal Complexes Exhibiting Thermally Activated Delayed Fluorescent Emission Mechanism

Gilbert Umuhire Mahoro, Julio Fernandez-Cestau, Jean-Luc Renaud, Pedro B. Coto, Rubén D. Costa, and Sylvain Gaillard**

This review focuses on the state-of-the-art of solid-state lighting devices (SSLDs)—that is, organic light-emitting diodes (OLEDs) and light-emitting electrochemical cells (LECs)—prepared with transition metal complexes featuring thermally activated delayed fluorescence (TADF) mechanism. First, the TADF mechanism is briefly introduced, as well as the experimental and theoretical methods applied to study TADF in transition metal complexes. Second, the review presents an exhaustive overview of OLED and LEC devices incorporating organometallic TADF emitters. For each type of device, the description of TADF is organized by respective elements focusing on each emission color, that is, blue, green/yellow, orange/red and, if existing, white. Finally, insights and future potential development of organometallic TADF emitters for lighting devices are comprehensively discussed. Overall, this review complements recent ones focused on TADF small molecules applied to the SSLD field.

1. Brief Introduction to TADF and Its Use in Thin-Film Lighting

1.1. Concepts, History, and Emitters

In the luminescent process, a molecule that has been promoted to an electronically singlet excited state decays into its electronic ground state by emitting a photon. This radiative process is named fluorescence. However, the singlet excited state can also decay via intersystem crossing (ISC) to triplet excited states, from which radiative relaxation can also occur—that is, phosphorescence (**Figure 1**).

Hence, fluorescence and phosphorescence processes are the most encountered radiative pathways for luminescent materials. However, if the triplet excited state lives long enough as well as the energy gap between the singlet and triplet excited states is small enough, a reverse intersystem crossing (RISC) is accessible at room temperature (RT). Here, the singlet excited state is repopulated from the triplet excited state and the so-called thermally activated delayed fluorescence (TADF) is observed (Figure 1).

While the search and implementation of TADF molecules for lighting applications is an apparently novel topic, the concept of TADF is a well-known emissive process. Indeed, the pioneering works proposing RISC as the base of a delayed fluorescence (DF) mechanism date back to 1929 by Delorme and Perrin,[1] 1941 by Lewis and co-workers,[2] and 1961 by Parker and Hatchard.[3] At that time, this process was just a mere curious behavior. However, Adachi and co-workers demonstrated in 2009[4] that the TADF mechanism will be key toward a new generation of highly efficient solid-state lighting devices (SSLDs), including organic light-emitting diodes (OLEDs)[5,6] and light-emitting electrochemical cells (LECs).[7]

The differences with respect to mechanism, photophysical features, and molecular design between TADF and conventional fluorescence/phosphorescence emitters applied to SSLDs were recently discussed by Huang et al. in 2014[5] and Yersin et al. in 2017,[8] while the outstanding theoretical and computational advances were discussed by Penfold et al. in 2018.[9] In short, several reasons explain the high interest of TADF-emitters for SSLD technologies. The most important is a potential 100% internal quantum efficiency (IQE) that can be reached for electroluminescence (EL)—that is, conversion into light of all excitons generated by electron-hole recombination.[10] Indeed, electroluminescence in SSLD is obtained from excitons generated by charge recombination leading to a 3:1 ratio population of triplet and singlet excitons.[11] In the case of phosphorescent molecules, the 75% of triplet excitons can be directly converted into light

G. U. Mahoro, Prof. J.-L. Renaud, Dr. S. Gaillard
Laboratoire de Chimie Moléculaire et Thio-organique (LCMT)
Normandie Univ, ENSICAEN, UNICAEN, CNRS
Caen 14000, France
E-mail: sylvain.gaillard@ensicaen.fr
G. U. Mahoro, Dr. J. Fernandez-Cestau, Dr. R. D. Costa
IMDEA Materials Institute
Calle Eric Kandel 2, Getafe, Madrid 28906, Spain
E-mail: ruben.costa@imdea.org
G. U. Mahoro
Departamento de Física Aplicada
Universidad Autónoma de Madrid
Calle Francisco Tomás y Valiente 7, Madrid 28049, Spain
Dr. P. B. Coto
Materials Physics Center (CFM)
Spanish National Research Council (CSIC)
Paseo Manuel de Lardizabal 5
Donostia-San Sebastián, Gipuzkoa 20018, Spain
The ORCID identification number(s) for the author(s) of this article can be found under https://doi.org/10.1002/adom.202000260.

DOI: 10.1002/adom.202000260

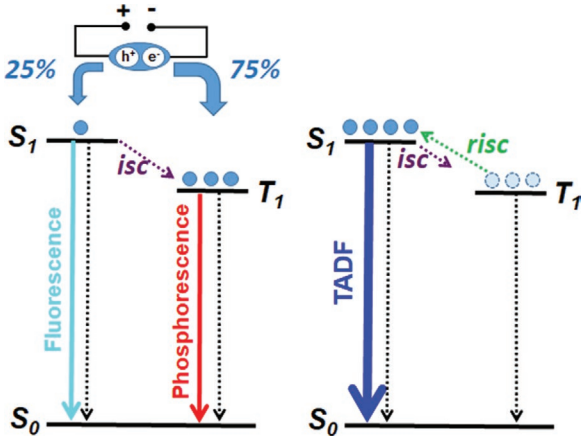

Figure 1. Simplified Jablonski diagram describing either the fluorescence and the phosphorescence processes (left) or the TADF pathway (right) after electron–hole recombination.

by the phosphorescence mechanism due to the high spin–orbit coupling (SOC). The latter also favors the ISC of the formed 25% singlet excitons into triplet excitons, which then deactivates via phosphorescence. TADF mechanism differs from phosphorescence as the emissive deactivation is obtained from the singlet excited state as explained above.[12] Thus, the 25% of singlet excitons can generate a prompt fluorescence (PF), while the 75% of triplet excitons repopulate the singlet energy level via an endothermic RISC before deactivation via DF (Figure 1). Thus, as TADF mechanism involves more steps than PF, the observed emission decay time (τ) of TADF emitters is longer than those of PF emitters but still shorter than phosphorescent molecules.[13]

As mentioned above, the RISC process requires some conditions, such as i) a small singlet–triplet energy splitting ($\Delta E_{ST} \leq$ 0.37 eV)[14]—that is, the difference between the energy level of the lowest singlet (S_1) and triplet (T_1); ii) a high rate for the RISC process (k_{RISC}) that should be much higher than the rates of the ISC (k_{ISC}) and the phosphorescence (k_P); and iii) a long-lived T_1 state. The combination of both high k_{RISC} and long-living T_1 states leads to the efficient repopulation of the S_1 state that radiatively deactivates to the ground state (GS) by DF. There are two major advantages of TADF emitters. On one hand, S_1 energy level is higher than T_1 rendering easier the access to efficient blue-emitting devices that still represent a milestone for both, OLEDs and LECs. On the other hand, several research groups have provided excellent guidelines on structure/property relationships for the design of more efficient TADF emitters by both experimental and theoretical approaches.[5,8,9] These rationalizations have resulted in interesting breakthroughs in high-energy emitting OLEDs. For instance, low ΔE_{ST} values require that the highest occupied molecular orbital (HOMO) and lower unoccupied molecular orbital (LUMO) are spatially separated.[15,16] In general, for TADF organic emitters, this is achieved by using either a spiro connection or a twisted molecular structure between donor and acceptor moieties in order to reduce the overlap between HOMO and LUMO (**Figure 2**a). Nevertheless, the simple vision of interconversions between the singlet and the triplet excited state does not explain how spin-flip can occur in organic compounds featuring a weak SOC. In the past few years, experimental and theoretical studies have shown that a more complicated second order process

Pedro B. Coto received his Ph.D. from the University of Oviedo (Spain) in 2003. After postdoctoral research with Prof. M. Olivucci at the University of Siena (Italy), Prof. M. Merchán at the University of Valencia (Spain), and Prof. M. Thoss at the University of Erlangen-Nürnberg (Germany), he joined the Materials Physics Center in San Sebastián (Spain) and started the Theoretical and Computational Chemistry group. His research interests include the investigation of photochemical processes in biological systems and organic molecules and charge transfer and transport processes in new materials with applications to organic photovoltaics and electronics.

Rubén D. Costa received his Ph.D. from the Universidad Valencia (Spain) in 2010 and was Humboldt post doc at the Universität Nürnberg-Erlangen (Germany) from 2011–2013. In 2014, he started the Hybrid Optoelectronic Materials and Devices Lab as Liebig group leader (2014–2017). In 2017, he moved his group to IMDEA Materials (Spain). His research encompasses the design and preparation of new hybrid materials and their use in optoelectronic devices for energy- and medical-related applications.

Sylvain Gaillard received his Ph.D. from the Université Paul Cézanne/ Aix-Marseille III, France, under the supervision of Dr. A. Tenaglia. After a first postdoctoral position under the supervision of Prof. J.-L. Renaud, Prof. C. M. Thomas, and Dr. C. Fischmeister at the ENSCR in Rennes, France, he pursued a second postdoctoral position under the supervision of Prof. S. P. Nolan at the University of St Andrews, Scotland, UK. In 2010, he obtained an associate professor position with Prof. J.-L. Renaud at Normandy University, Caen, France. His research interests include organometallic chemistry, homogeneous catalysis, and photoluminescent materials.

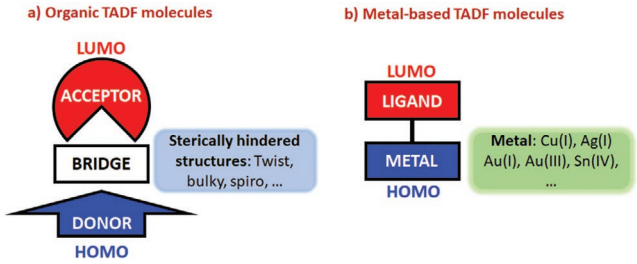

Figure 2. Simplified representation of the general design of a TADF emitter a) based on organic molecules (D-A) disposition and b) metal-based molecules with MLCT emissive transitions.

explains the spin-flip.[17] Indeed, Penfold and co-workers in agreement with previous works[18,19] have shown that vibronic coupling between charge transfer (^{3}CT) and localized (^{3}LE) triplet states are required for efficient RISC and TADF.[20,21] This new insight into the TADF mechanism led Adachi and co-workers to enlarge the design of TADF materials by combining multiple donors and acceptors, leading to a new family of very efficient TADF organic emitters.[22,23] Nevertheless, such spiro derivatives or twisted structures are sometimes difficult to prepare and may have some limitations to introduce electron donor or withdrawing groups at various positions.

By contrast, transition metal complexes offer a larger number of combinations involving d-block metal ions and ligands following simple and low-cost synthesis procedures. In other words, more pieces can easily be envisaged to the puzzle for the development of emissive compounds. Nevertheless, this may renders the rationalization of the emission pathway more complicated, as metal character orbitals are involved including an interplay between a myriad of excited states (i.e., metal-centered, metal-to-ligand charge transfer, ligand-centered, ligand-to-ligand charge transfer) caused by the easy structural arrangements of the coordination sphere of the metal ion core and the SOC values allowing or not spin changes. Considering the ease of syntheses, most of the coordination reactions are highly selective, giving very good to excellent isolated yields. In addition, the type of binding motif to the ion metal core determines the type of neutral or charged nature of the complexes, allowing their use in both OLEDs (neutral complexes) and LEC (ionic complexes)—Section 2.

Indeed, if the LEC technology is considered, ionic transition metal complexes are much more accessible than ionic TADF organic emitters. Finally, the versatile design of ionic transition metal complexes offers large choice of options to reach emission colors covering the whole visible range. Here, the HOMO features a strong d-metal character, while the LUMO is typically ruled by the ancillary organic ligand (Figure 2b). Thus, spatial separation of the HOMO and LUMO is full-filled. Indeed, as metal-to-ligand charge transfer (MLCT)—that is, d→π* electronic transition– is usually responsible for the emission of transition metal complexes, this prerogative is easily accessible. However, the interplay of excited states with ligand-centered and ligand-to-ligand charge transfer natures is crucial to ensure an efficient TADF emission mechanism. Of note, emissive excited states with MLCT nature are highly favored in the case of d^{10} transition metal complexes as all d orbitals are occupied, suppressing the potential non-radiative d→d* electronic transition—that is, metal-centered electronic transition (MC). This particular electronic configuration of d^{10} metal center explains the important efforts devoted to Cu(I), Ag(I), Au(I), and Zn(II) complexes for SSLDs. As low values of SOC diminish the possibility of a $T_1 \rightarrow S_0$ deactivation, copper(I) complexes are the most representative TADF-type organometallic compounds. For reference purposes, SOC values of 870 cm^{-1} (ζ_{Cu2+} value for free metal ion) strongly contrast with those of iridium and ruthenium complexes with SOC values of 4814 and 1201 cm^{-1} (the given values for ζ_{Ir4+} and ζ_{Ru3+} are for the free metal ions), respectively.[24]

Another crucial property is the geometry of the excited state that must be similar to that of the GS.[9] In the first approach, to generate TADF emission, molecules were designed in a fashion to render them the most rigid as possible to diminish non-radiative decays.[25] Nevertheless, Penfold and Monkman reported that high molecular rigidity can lead to negative effects on the spin-vibronic coupling that negatively impacts the k_{RISC} and consequently the TADF process.[20]

1.2. Experimental and Theoretical Determination of the TADF Process

The most comprehensive study to determine TADF existence is the temperature-dependence of the τ values going from 77 K (sometimes 1.6 K to determine the lifetime of the three triplet sub-states) to 298 K.[26] Indeed, lowering the temperature blocks the TADF process, allowing only the observation of the phosphorescent emission. The τ values taken at different temperatures lead to an empirical curve. After an extrapolation from an Arrhenius plot, several parameters can be obtained from these experimental measurements, such as i) decay time of the prompt fluorescence ($\tau_{(S1)}$), ii) decay time of phosphorescence ($\tau_{(T1)}$), and iii) ΔE_{ST}. The mathematical fitting includes a three-state model system (Equation (1)) in which k_B is the Boltzmann constant.[8,27]

$$\tau(T) = \frac{3 + \exp\left(-\frac{\Delta E_{(ST)}}{k_B T}\right)}{\frac{3}{\tau_{(T1)}} + \frac{1}{\tau_{(S1)}} \cdot \exp\left(-\frac{\Delta E_{(ST)}}{k_B T}\right)} \quad (1)$$

Other experimental or theoretical methods have also been used for the estimation of ΔE_{ST}. For example, the difference between the onsets of the fluorescence and phosphorescence spectra (phosphorescence spectra is recorded at 77 K to observe only the phosphorescence emission and block the TADF process, **Figure 3**).[28–31] However, this estimation method, which can only be possible when both S_1 and T_1 result from the same molecular orbitals, also should be used with more precautions as the shift of the emission spectra can be sometimes masked or covered by temperature-induced broadening effects.[31]

In this respect, theory and simulation can play an important role in the characterization of the TADF process and in the design of new TADF-active materials for optoelectronic applications.[32,33] On one hand, they can assist the interpretation of the experimental results contributing to their rationalization.[8,34] On the other hand, they can provide design and mechanistic information that cannot be straightforwardly obtained from the experiments.[35,36] However, and despite the considerable advances carried out in the field over the years, the theoretical description

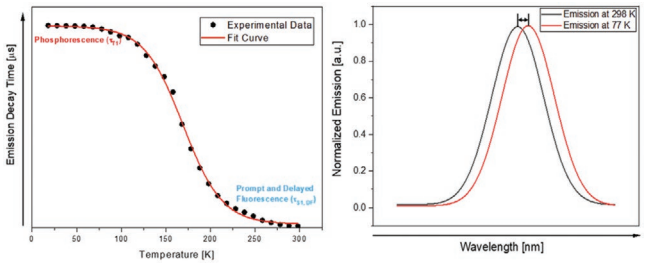

Figure 3. Left: Plot of decay lifetime versus temperature in a TADF emissive complex showing the phosphorescence region at low temperature and the TADF region at higher temperatures. Right: Onset emission spectra at RT of 298 K (black) and 77 K (red), a blue-shift of the emission upon heating often characteristic of TADF existence.

of TADF is still a challenging task.[32] This is related to the very nature of the process, which involves the participation of excited electronic states of different nature[37,38] with small energy gaps or near degeneracies between some of them,[39,40] and interacting through relatively small spin–orbit (and/or vibronic spin–orbit)[9,17,41–44] and hyperfine[45] interactions whose accurate evaluation is instrumental to characterize the ISC process that triggers TADF.[46] Furthermore, the characterization of the TADF process also requires the accurate description of several competing quenching mechanisms such as phosphorescence[47] or non-radiative deactivation processes,[48] and has to account for dynamical aspects that may have an important impact on TADF processes such as thermal fluctuations or mode-specific vibrational effects.[35,49] In addition, the prototypical systems used in technological applications are of medium to large size, can incorporate heavy atoms in their structure, and may arrange in amorphous structures with a surrounding environment that can have a significant impact on the photophysics of TADF.[40,50–53] Altogether, these issues impose practical limitations on the atomistic simulation methods that can be employed in the description of TADF, calling for the use of those that can provide a reasonable balance between the necessary accuracy and the computational cost. In this respect, and among the different state-of-the-art electronic structure methods for the description of excited electronic states available,[54–58] linear response time-dependent density functional theory (TD-DFT) approaches[59] are the most widely used.[60–62] The reasons are that these approaches can provide a reasonably good description of the electronic excited states involved in the process; their energies and their interactions such as spin–orbit contributions, can be used for the simulation of the dynamics of the process and can be employed in the simulation of large systems incorporating environmental effects with a good balance between accuracy and computational cost.[32] However, and despite the success obtained with these methods, it should be stressed that their use requires a careful assessment. This is due to the well-known limitations of DFT, linear response TD-DFT, and some of the conventionally used exchange-correlation functionals in the characterization of some types of electronic states (such as multiconfigurational electronic states, doubly excited or charge transfer states) and molecular funnel (conical intersection) regions, which can play a key role in TADF processes.[59,63] More details on these and other topics in the theoretical description and simulation of TADF processes can be found in refs. [32,33].

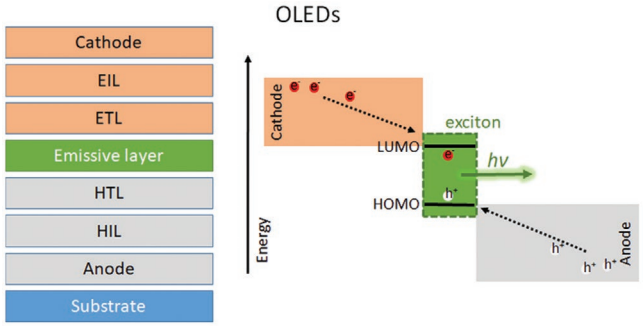

Figure 4. Architecture (left) and working principle (right) of an OLED device.

1.3. Thin-Film Lighting Device: Design and Working Mechanism

Besides the considerations about the chemistry and the photophysics of TADF organometallic compounds, efficient lighting devices require to take into account how the device design and working mechanism can affect the TADF process. Thus, the OLEDs and LECs working principles are described in the following:

A typical OLED consists of a transparent substrate (glass or plastic) that supports a multilayer architecture: i) transparent anode made of indium tin oxide (ITO), ii) a hole injection material (HIL), iii) a hole transport layer (HTL), iv) the active or emissive layer (EML), v) the electron transport layer, vi) the electron injection layer (EIL), and vii) the cathode, that closes the circuit (**Figure 4**). When a driving voltage is applied, electrons and holes are injected to the EIL and HIL from the cathode and anode electrodes, respectively. Both carriers are transported through the bulk to the EML. Here, electrons and holes recombine, forming excitons that radiatively relax. Typically, the EML consists of a mixture of a host—for example, mCP (*N*,*N*′-4,4′-dicarbazole-3,5-benzene), PYD2 (2,6-dicarbazolo-1,5-pyridine)—and a guest that acts as an emitter. Therefore, the TADF emitter in OLEDs can be either charged or neutral as it is not involved in the injection and transport processes, while the externally applied electric field is screened out. All-in-all, OLED optimization using TADF emitters has also led to guidelines with respect to the host design,[64] resulting in record EQE values of 37% and 30% for blue/green[10,65,66] and 29.2% orange/red[67] OLEDs (see Section 1.4 for more details).

Then, Pei and co-workers demonstrated a new device concept called LEC that consists of i) a transparent anode, ii) an active layer, in which the emitter is blended with an ionic electrolyte, and iii) an air-stable cathode (**Figure 5**). While in OLEDs

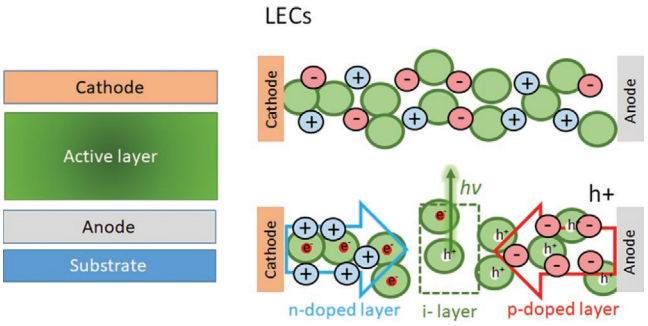

Figure 5. Architecture (left) and working scheme (right) of a LEC device.

the emission layer is not involved in ionic mobility, in LECs, the presence of mobile ions in the active layer assists charge injection and electrochemical doping from the air-stable electrodes.[68] Thus, the emitter must feature a reversible electrochemistry as it experiences both p- and n-type doping. The ionic electrolyte is responsible for the formation of electrical double layers at the electrode interfaces which allow charge injection at low applied voltages. Thus, the electric field decreases close to the electrode interface and holds constant across the active layer. In addition, the ionic electrolyte also controls the growth of the doped regions, forming the so-called p-i-n junction, in which the exciton formation is produced at the intrinsic (i) or neutral region.[68–70]

The host–guest approach can also be applied in LECs, but the control of balanced charge transport and electron–hole recombination is challenging. In addition, the devices experience strong and dynamic internal local electric fields. In contrast to OLEDs, the record efficiency achieved for LECs was 3.7 cd A^{-1} without the use of the host–guest approach.[71] This value is, nevertheless, very low compared to OLEDs. This fact could be related to several aspects, such as electric field across the active layer, working temperature, and interactions between the exciton and the doped species.

The host–guest approach commonly applied in OLEDs and barely in LECs is also critical as the interaction between the emitter and the host could play a role in the TADF mechanism.[64] As an example, Monkman and co-workers have observed that using hosts with different polarizability affects the energy level of the CT state and consequently the RISC rate of organic molecule.[52,72] This solid-state solvation effect (SSSE) was later supported by theoretical studies showing that like in solution, the solvation of the emitter in thin-film clearly impacts the TADF mechanism.

In order to help the reader to understand the figures-of-merit of the SSLD, we provide a short description as follows: In OLEDs and LECs, the emitted light is often described by the colorimetric system of the Commission Internationale de l'Eclairage (CIE).[73] The light is intensified into luminance or brightness which represents the amount of light that is emitted by the device per a unit of area (cd m^{-2}). The efficiency of the devices can be expressed as EQE (%), which is a key parameter that represents the ratio between the emitted photons and the injected charges into the device. Alternatively, the efficiency can be measured in terms of current efficiency (CE) or *Eff* (cd A^{-1}) and luminous power efficiency (PE) (lm W^{-1}). The turn-on voltage (V_{on}) is commonly considered as the voltage necessary for the device to start emitting light, but in some cases especially in OLEDs, it is assumed as the voltage at a luminance of 1 cd m^{-2}. The turn-on time (t_{on}) represents the time required for a device to reach its maximum luminance (L_{max}), while the lifetime or stability is defined as the amount of time that a device lives before losing half of its L_{max}.

1.4. Relevance of the TADF for the Lighting Market

The SSLD industry offers highly bright and efficient lighting sources and displays for portable devices, televisions, indoor and outdoor lighting, lights of cars, etc. Efficiency and stability of OLEDs have led to a huge commercial success. For example, IHS Markit estimates that OLED TV display revenues will grow from $2.9 billion in 2019 to $7.5 billion in 2025,[74] while LG estimates a growth from $3.9 million of panels in 2019 to over $10 million in 2021.[75] Moreover, the global sales of OLED displays are expected to reach over 40 billion USD in 2020.[76] Most of the commercial OLEDs are based on iridium, a rare earth metal with a strong SOC that allows iridium complexes to harvest both singlet and triplet excitons via phosphorescence. Despite the huge success of OLEDs, the main drawback named blue gap remains, as stable and efficient deep blue phosphorescent emitters are still unavailable.[6,77] The current approach toward the production of blue-emitting OLEDs consists of combining fluorescent blue emitters and host matrices. In this context, the implementation of TADF emitters is highly attractive to achieve highly efficient SSLD, as they offer a wide range of color emissions with good stabilities.[78] Thus, it is not surprising that TADF has gathered a lot of attention in the academic and industrial environment. Indeed, for the last 5 years, the number of publications related to TADF and OLEDs has been consistently rising. According to the data collected by the Web of Science (November 11th, 2019), 544 total articles including reviews discussing TADF and OLEDs have been published since 2015, cumulating 12 658 total citations.[79] As record devices, they have reached performances that are comparable to that of phosphorescent-based devices in terms of stability with over 10 000 h at an initial luminance of 1000 cd m^{-2},[80] and efficiency with EQE values of 37%.[65]

Finally, TADF mechanism is becoming key toward efficient blue-emitting thin-film devices. In general, TADF emitters can be divided into two groups: small molecules (SM) and organometallics. While the former has exhaustively been investigated reaching a mature knowledge with respect to molecular design, emission features, and device optimizations,[5,12,64,77,78,81–85] TADF organometallic compounds have been much less investigated to date.[5,12,31,77,86–89] This represents the focus of this review, complementing other recent ones.[5,12,31,86–89] In short, we have compiled all data published in the literature on SSLD devices—that is, OLEDs and LECs—including transition metal complexes showing TADF emission (Section 2). We have divided this section with regards to the type of metal core, and for each metal, the discussion is further focused on the emission color,—that is, blue, green, red, and white colors—of the devices.

2. Organometallic TADF Compounds for Lighting

2.1. Complexes with d^{10} Electronic Configuration

2.1.1. Copper(I) Complexes

Among the transition metal complexes possessing TADF emission, copper(I) derivatives are the most studied due to i) the weak SOC and propensity to have small ΔE_{ST},[24] ii) the d^{10} electronic configuration that precludes the non-radiative metal centered electronic transition, iii) the high photoluminescence quantum yields (PLQY), and iv) the low-cost copper due to its higher crust Earth abundancy compared to platinum metals. Herein, we have only focused on TADF copper(I) complexes

that have been applied to lighting devices, such as OLEDs and LECs. For detailed libraries of emissive Cu(I) complexes, the reader is highly recommended to refer to these excellent reviews and key articles.[8,12,14,27,47,70,85–87,90–100]

Blue-Emitting OLEDs: In 2013, Lu and co-workers published the first blue-emitting complexes [Cu(N^N)(POP)][BF_4] **Cu1–Cu3** (POP = bis(2-(dipenylphosphino)phenyl)ether in **Cu1–Cu3**) (N^N = pypz = 1-(2-pyridyl)pyrazole in **Cu1**, pympz = 3-methyl-1-(2-pyridyl)pyrazole in **Cu2**, and pytfmpz = 3-trifluoromethyl-1-(2-pyridyl)pyrazole in **Cu3**) exhibiting TADF in OLEDs (**Table 1** and **Scheme 1**).[30] The introduction of the electron-rich diimine pyridine-pyrazol ligands is the critical point

Table 1. Photophysical properties of Cu(I) complexes with TADF.

Complex[a)]	λ_{max} [nm][b)]	PLQY [%]	τ_{PF} [ns]/ τ_T [µs]/ τ_{TADF} [µs]	ΔE_{ST} [eV]	HOMO/LUMO [eV]	CIE [x/y]	Ref.
Cu1	490[c)]/508[d)]	56[c,f)]	–/–/20.4	0.18	–5.41/–2.23	0.20/0.38	[30]
Cu2	465[c)]/493[d)]	87[c,g)]	–/–/12.2	0.17	–5.39/–2.16	0.16/0.21	[30]
Cu3	492[c)]/511[d)]	75[c,g)]	–21/346/22.8	0.18	–5.53/–2.49	0.19/0.36	[30]
Cu4	493[c)]/501[d)]	60.9[c,g)]	562/565/145	0.12	–7.10/–4.11	–	[101]
Cu5	475[c)]/516[d)]	40.7[c,g)]	153/476/51	0.12	–6.87/–4.05	–	[101]
Cu6	463[c)]	22[c,g)]	670/45/13	0.35	–	–	[102,103]
Cu7	479[c)]	64[c,g)]	–/–/30	0.35	–	–	[102]
Cu8	458[c)]	86[c,g)]	800/81/44	–	–	–	[102]
Cu9	473[c)]/481[d)]	15[c,g)]	9.4/32/6	0.07	–	–	[103]
Cu10	474[c)]/482[d)]	73[c,g)]	141/38/14	–	–	–	[103]
Cu11	503[c)]/519[d)]	86[c,g)]	101/87/13	0.06	–	–	[103]
Cu12	545[c)]/550[d)]	50[c,h)]	–/170/3.8	0.16[i)]	–5.13/–1.17	–	[104]
Cu13	534[c)]/534[d)]	63[c,h)]	–/400/3.6	0.20[i)]	–5.61/–1.60	–	[104]
Cu14	523[c)]/514[d)]	68[c,h)]	–/270/8.2	0.19[i)]	–5.87/–2.06	–	[104]
Cu15	521[c)]/534[d)]	52[c)]/73[d,g)]	–/847/1.73,0.33	0.04[i)]	–	–	[105]
Cu16	517[c)]/507[d)]	38[c)]/56[d,g)]	–/2500/4.6	0.08[i)]	–5.23/–2.23	–	[106]
Cu17	512[c)]/500[d)]	55[c)]/85[d,g)]	–/360/8.0	0.10[i)]	–5.27/–2.24	–	[106]
Cu18	473[c)]/456[d)]	59[c)]/85[d,g)]	–/100/7.1	0.10[i)]	–5.22/–2.15	–	[106]
Cu19	487[c)]/477[d)]	80[c)]/85[d,g)]	–/520/6.5	0.07[i)]	–5.18/–2.13	–	[106]
Cu20	486[c)]/487[d)]	95[c)]/95[d,g)]	–/910/8.9	0.09[i)]	–5.20/–2.15	–	[106]
Cu21	495[c)]/507[d)]	45[c)]/71[d,g)]	–/671/134	0.18	–5.51/–2.59	–	[108]
Cu22	518[c)]/521[d)]	98[c)]/39[d,g)]	–/521/23	0.13	–	–	[108]
Cu23	530[c)]/531[d)]	76[c)]/82[d,f)]	–/1778/19	0.10	–4.89/–1.46	–	[112]
Cu24	523[c)]/531[d)]	79[c)]/83[d,f)]	–/1611/16	0.94	–4.86/–1.46	–	[112]
Cu25	521[c)]/531[d)]	83[c)]/85[d,f)]	–/294/11	–	–4.78/–1.47	–	[112]
Cu27	537[c)]/580[d)]	34[c)]/10.9[d,g)]	–/8.7/569	0.23[i)]	–	–	[113]
Cu28	570[c)]/591[d)]	15.5[c)]/33.7[d,g)]	–/859/5.3	0.14[i)]	–	–	[113]
Cu30	552[c)]/598[d)]	26.6[c)]/10.5[d,g)]	–/208/6.2	0.18[i)]	–	–	[113]
Cu31	497[c)]/514[d)]	38.9[c)]/62.1[d,h)]	–/1145.7/15.3	0.14[i)]	–5.19/–2.46	–	[114]
Cu32	588[c)]/600[d)]	6.6[c)]/16[d,h)]	–/473/5.5	0.20[i)]	–5.25/–2.69	–	[114]
Cu33	657[c)]/624[d)]	4.2[c)]/4.4[d,h)]	–/495.6/2.1	0.26[i)]	–5.22/–2.99	–	[114]
Cu34	519[c)]/558[d)]	88[c)]/76[d,g)]	190/110/34	0.10[i)]	–5.30/–2.60	–	[31,115]
Cu35	547[c)]	69[c,g)]	–	0.10 ± 0.5	–	0.36/0.47	[117]
Cu36	498[c)]/500[d)]	32[c,g)]	–/103/2.5	0.12	–4.70/–0.87	–	[118]
Cu37	511[c)]/517[d)]	28[c,g)]	–/714/12.5	0.12	–4.50/–0.87	–	[118]
Cu38	527[c)]/532[d)]	29[c,g)]	–/818/4.8	0.14	–4.50/–0.98	–	[118]
Cu39	520[c)]/550[d)]	20[c,h)]	5.1/52.7/1.05	0.12	–	–	[119]
Cu40	525[c)]/555[d)]	5.8[c,h)]	3.5/109.6/0.61	0.23	–	–	[119]
Cu41	550[c)]/568[d)]	22.4[c)]/19.3[d,g)]	125/334/5.7	0.09	–6.13/–2.66	–	[120]
Cu42	549[c)]/560[d)]	18.5[c)]/16.2[d,g)]	105/310/5.7	0.09	–6.12/–2.59	–	[120]
Cu43	556[c)]/564[d)]	20[c)]/19.4[d,g)]	132/356/5.7	0.09	–6.16/–2.61	–	[120]
Cu44	509[c)]/523[d)]	45[c)]/67[d,g)]	73/158/5.5	0.09	–5.20/–2.33	–	[121]

Table 1. Continued.

Complex[a]	λ_{max} [nm][b]	PLQY [%]	τ_{PF} [ns]/τ_T [µs]/τ_{TADF} [µs]	ΔE_{ST} [eV]	HOMO/LUMO [eV]	CIE [x/y]	Ref.
Cu45	519[c]/546[d]	29[c]/54[d,f]	75/356/16	0.12	–5.21/–2.32	–	[121]
Cu46	503[c]/516[d]	79[c]/82[d,f]	51/209/1.4	0.10	–5.22/–2.33	–	[121]
Cu47	553[c]	32[c,f]	55/261/16.3	0.12	–	–	[125]
Cu48	548[c]	22[c,f]	66/122/14.9	0.11	–	–	[125]
Cu49	538[c]	24[c,f]	100/167/17.1	0.11	–	–	[125]
Cu50	527[c]	28[c,f]	58/169/27.5	0.13	–	–	[125]
Cu52	502[c]	33[c,g]	–/–/3	0.14	–5.58/–2.59	–	[130]
Cu53	506[c]/502[d]	90[c,g]	70/44190/1.3	0.06	–4.98/–1.88	–	[131]
Cu54	490[c]/508[d]	90[c,f]	–/269/23.6	0.09	–5.80/–2.85	–	[133]
Cu55	512[c]/520[d]	27.8[c,f]	–/210/13.0	0.04	–5.70/–2.73	–	[133]
Cu56	553[c]	48.8[c,g]	31.6/–/5.3	–	–	–	[134]
Cu57	537[c]	77.9[c,g]	25.7/–/5.5	–	–	–	[134]
Cu58	526[c]	63.7[c,g]	30.3/–/5.3	–	–	–	[134]
Cu59	487[c]/500[d]	69[c,g]/81[d,f]	182/58.8/9.46	0.07[h]	–5.12/–1.98	–	[137]
Cu60	483[c]/494[d]	86[c,g]/96[d,f]	299/126/7.62	0.04[h]	–5.18/–2.15	–	[137]
Cu61	521[c]	20[c,f]	–/–/7	0.36	–	–	[102]
Cu62	575[c]/610[d]	6.2[c,f]	–/45/2.9	–	–6.07/–2.53	–	[138]
Cu63	581[c]/595[d]	11.1[c,f]	–/31/2.9	–	–6.07/–2.36	–	[138]
Cu64	517[c]/604[d]	50.3[c,f]	–/42/12	0.11	–6.17/–2.76	–	[138]
Cu65	584[c]/573[d]	14.8[c,g]/25.7[d,e]	–/82/2.7	0.15	–5.99/–2.74	–	[141]
Cu66	587[c]/560[d]	17.1[c,g]/30.6[d,e]	–/119/3.3	–	–6.07/–2.78	–	[141]
Cu67	582[c]/613[d]	3.9[c,g]/3.8[d,e]	–/12/2.5	–	–6.00/–2.61	–	[141]
Cu68	569[c]/593[d]	16.3[c,g]/18[d,e]	–/25/4.8	–	–6.03/–2.65	–	[141]
Cu69	596[c]/568[d]	6.3[c,g]/27.5[d,e]	–/55/2.6	–	–6.00/–2.83	–	[141]
Cu70	544[c]/569[d]	10.9[c,g]/40[d,e]	–/107/2.3	0.19	–6.09/–2.78	–	[141]
Cu71	565[c]/599[d]	17[c,g]/5[d,e]	–/21/3.3	0.23	–5.87/–2.46	–	[145]
Cu72	570[c]/596[d]	9[c,g]/6[d,e]	–/2.7/28	–	–5.90/–2.47	–	[145]
Cu73	585[c]/613[d]	5[c,g]/3[d,e]	–/16/1.5	–	–5.92/–2.55	–	[145]
Cu74	549[c]/563[d]	30[c,g]/10[d,e]	–/48/10.2	0.21	–5.94/–2.52	–	[145]
Cu75	564[c]/598[d]	22[c,g]/9[d,e]	–/31/6.5	–	–5.93/–2.52	–	[145]
Cu76	566[c]/600[d]	20[c,g]/7[d,e]	–/33/6.2	–	–5.98/–2.55	–	[145]
Cu77	566[c]/593[d]	19[c,g]/11[d,e]	–/23/4.7	–	–5.92/–2.53	–	[145]
Cu78	566[c]/594[d]	22[c,g]/15[d,e]	–/23/4.0	–	–5.91/–2.52	–	[145]
Cu79	572[c]/610[d]	12[c,g]/11[d,e]	–/13/2.7	–	–5.93/–2.57	–	[145]
Cu80	557[c]/588[d]	21[c,g]/20[d,e]	–/38/6.0	0.21	–5.90/–2.53	–	[145]
Cu81	552[c]/575[d]	32[c,g]/20[d,e]	–/38/6.5	–	–5.93/–2.55	–	[145]
Cu82	552[c]/576[d]	38[c,g]/23[d,e]	–/44/9.1	–	–5.92/–2.52	–	[145]
Cu83	584[c]/597[d]	3[c,g]/7[d,e]	–/27.6/1.95	–	–5.98/–2.54	–	[146]
Cu84	552[c]/578[d]	16[c,g]/25[d,e]	–/56.3/6.32	–	–5.96/–2.51	–	[146]
Cu85	522[c]/555[d]	59[c,g]/46[d,e]	–/92/13.8	–	–5.98/–2.40	–	[146]
Cu86	589[c]/594[d]	1.9[c,g]/11[d,e]	–/20/1.19	–	–5.87/–2.45	–	[146]
Cu87	547[c]/587[d]	26[c,g]/19[d,e]	–/19.7/6.62	–	–5.89/–2.49	–	[146]
Cu88	575[c]	20[c,f]	–/–/1.22, 0.33	–	–5.8/–2.8	–	[147]
Cu89	493[c]	20[c,f]	–	–	–	–	[149]
Cu90	671[c]	56[c,f]	–/–/0.63	–	–5.6/–3.5	–	[150]

[a]Selected photophysical data in solid-state for Cu(I) complexes with TADF used in OLEDs and LECs or discussed in this review; [b]Maximum emission wavelength; [c]Measured at 298 K; [d]Measured at 77 K. PLQY values in [e]solution (glassy solution of Me-THF); [f]powder; [g]film. Values converted from the ones reported by the authors in [h]cm^{-1}; [i]kJ mol^{-1}.

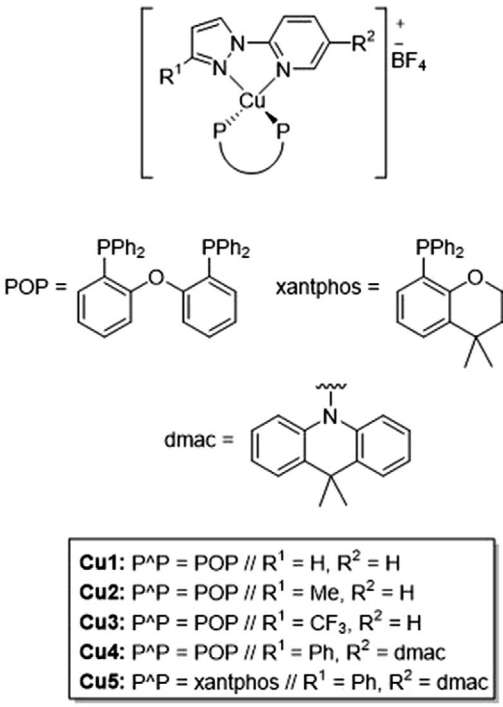

Scheme 1. Description of copper(I) complexes **Cu1–5**.

of access to high-energy emissions. In fact, the introduction of the electron-donating methyl group on the N^N ligand in **Cu2** (λ_{max} = 465 nm, PLQY = 87%) shifts the emission of the copper complex to higher energies compared to **Cu1** (λ_{max} = 490 nm, PLQY = 56%) and **Cu3** (λ_{max} = 492 nm, PLQY of 75%). These complexes showed τ values of 20.4, 12.2, and 22.8 µs; the ΔE_{ST} were estimated at 0.18, 0.17, and 0.18 eV for **Cu1**, **Cu2**, and **Cu3**, respectively.

The three complexes **Cu1–Cu3** were used as emissive materials for solution-processed OLEDs (**Table 2**). The configuration of the devices was ITO/PEDOT:PSS/complex in 20 wt%:host/DPEPO/LiF/Al. Two different hosts were tested: 2,6-bis(*N*-carbazolyl)pyridine (26mCPy; HOMO −5.7 eV, LUMO −2.2 eV) and bis(2-(diphenylphosphino)phenyl) ether oxide (DPEPO; HOMO −6.0 eV, LUMO −2.0 eV). First, 26mCPy was used; this device configuration (ITO/PEDOT:PSS/complex in 20 wt%:26mCPy/DPEPO/LiF/Al) was optimized for **Cu3** leading to green-emitting devices (λ_{max} = 508 nm, x/y CIE color coordinates: 0.21/0.33) with an L_{max} of 2033 cd m^{-2} and EQE of 8.47%. In contrast, complexes **Cu1** and **Cu2** feature LUMO levels relatively close to the level of 26mCPy. This resulted in a poor electron injection. As a consequence, devices based on **Cu1** and **Cu2** showed emissions from both the copper(I) complexes and the host, achieving L_{max} of 1116 and 502 cd m^{-2} and maximum EQEs of 3.18% and 1.59% for **Cu1** and **Cu2** devices, respectively. The authors replaced the host 26mCPy by DPEPO having a higher LUMO level and higher triplet level. Regardless of the emitter, devices with pure emissions from the complexes were obtained but only enhanced EQE values were noted for those with **Cu2** (EQE = 3.72%). The performance of devices with **Cu1** and **Cu3** significantly decreased caused by the lack of the hole-blocking barriers between the emitting and the electron transport layer.

The same authors published new complexes incorporating the group 9,9-dimethylacridan (DMAC), with remarkable steric bulkiness and well-known electron donor character, as a substituent of the pyridine ring of the N^N ligand associated with POP (**Cu4**) and 4,5-bis(diphenylphosphino)-9,9-dimethylxanthene (xantphos) (**Cu5**) (Table 1 and Scheme 1).[101] They aimed at i) increasing the PLQYs by restraining the flattening distortion in the excited states, and ii) improving the hole-transporting efficiency of the devices. The blue-emitting Cu(I) complexes **Cu4** and **Cu5** featured a much smaller ΔE_{ST} of 0.12 eV and τ_{TADF} of 50–145 µs in comparison to complexes **Cu1–Cu3** (vide supra and Table 1).[30] Solution-processed OLEDs doped with complexes **Cu4** and **Cu5** 20 wt% in mCP were fabricated (Table 2). The device with **Cu4** showed the most bluish emission (λ_{max} = 490 nm, x/y CIE color coordinates: 0.17/0.37) and the highest luminescence maximum of 6563 cd m^{-2}, while

Table 2. Figures of merit of OLED devices based on Cu(I) complexes with TADF.

Complex[a)]	Device architecture	V_{on} [V]	λ_{max} [nm]	L_{max} [cd m^{-2}]	EQE [%]	CE [cd A^{-1}]	PE [lm W^{-1}]	CIE [x/y]	Ref.
Cu1	ITO/PEDOT:PSS/**Cu1** 20wt%:DPEPO/DPEPO/LiF/Al	8.7	500	309	1.98	5.15	–	0.20/0.29	[30]
Cu2	ITO/PEDOT:PSS/**Cu2** 20wt%:DPEPO/DPEPO/LiF/Al	9.3	484	194	3.72	8.37	–	0.17/0.21	[30]
Cu3	ITO/PEDOT:PSS/**Cu3** 20wt%:DPEPO/DPEPO/LiF/Al	11.5	496	139	1.42	3.53	–	0.18/0.25	[30]
Cu4	ITO/PEDOT:PSS/TAPC/**Cu4** 20wt%:mCP/3TPYMB/LiF/Al	5.3	490	6563	5.83	14.0	–	0.17/0.37	[101]
Cu5	ITO/PEDOT:PSS/TAPC/**Cu5** 20wt%:mCP/3TPYMB/LiF/Al	7.4	501	5579	7.42	20.2	–	0.21/0.43	[101]
Cu12	ITO/PEDOT:PSS/TAPC/**Cu12** 10wt%:mCP/3TPYMB/LiF/Al	3.4	552	–	11.9	34.6	–	0.40/0.53	[104]
Cu13	ITO/PEDOT:PSS/TAPC/**Cu13** 10wt%:mCP/3TPYMB/LiF/Al	3.2	545	–	16.0	46.7	–	0.37/0.54	[104]
Cu14	ITO/PEDOT:PSS/TAPC/**Cu14** 10wt%:mCP/3TPYMB/LiF/Al	2.6	528	–	17.7	54.1	–	0.34/0.54	[104]
Cu15	ITO/PEDOT:PSS/PVK/**Cu15** 10wt%:TAPC 30wt%:mCP/3TPYMB/LiF/Al	5.0	–	–	7.8	21.3	–	0.40/0.53	[105]
Cu16	ITO/PEDOT:PSS/TAPC/**Cu16** 10wt%:mCP/3TPYMB/LiF/Al	3.3	527	–	21.1	67.7	–	0.30/0.55	[106]
Cu17	ITO/PEDOT:PSS/TAPC/**Cu17** 10wt%:mCP/3TPYMB/LiF/Al	3.0	517	–	21.3	65.3	–	0.29/0.4	[106]
Cu18	ITO/PEDOT:PSS/TAPC/**Cu18** 10wt%:mCP/3TPYMB/LiF/Al	3.1	513	–	21.2	62.4	–	0.25/0.51	[106]
Cu19	ITO/PEDOT:PSS/TAPC/**Cu19** 10wt%:mCP/3TPYMB/LiF/Al	3.3	529	–	22.5	69.4	–	0.32/0.54	[106]

Table 2. Continued.

Complex[a)]	Device architecture	V_{on} [V]	λ_{max} [nm]	L_{max} [cd m^{-2}]	EQE [%]	CE [cd A^{-1}]	PE [lm W^{-1}]	CIE [x/y]	Ref.
Cu20	ITO/PEDOT:PSS/TAPC/**Cu20** 10wt%:mCP/3TPYMB/LiF/Al	3.3	515	–	18.6	55.6	–	0.26/0.51	[106]
Cu22	ITO/PEDOT:PSS/**Cu22** A 20wt%:czpzpy/DPEPO/LiF/Al	5.6	514	2939	6.34	17.34	–	0.26/0.49	[108]
Cu22	ITO/PEDOT:PSS/**Cu22** B[b)] 15wt%:czpzpy/DPEPO/LiF/Al	5.6	516	3251	6.36	17.44	–	0.25/0.49	[108]
Cu23	ITO/MoO_3/TAPC/TCTA/**Cu23** 10wt%:mCP/TPBI/LiF/Al	3.5	584	–	9.6	24.7	21.4	0.47/0.50	[112]
Cu24	ITO/MoO_3/TAPC/TCTA/**Cu24** 10wt%:mCP/TPBI/LiF/Al	3.5	584	–	12.4	32.7	28.8	0.47/0.50	[112]
Cu25	ITO/MoO_3/TAPC/TCTA/**Cu25** 10wt%:mCP/TPBI/LiF/Al	3.5	584	–	16.3	40.8	35.9	0.48/0.49	[112]
Cu27	ITO/PEDOT:PSS/**Cu27** 5wt%:PYD2/DPEPO/TPBi/LiF/Al	–	–	3480	16.6	49.8	25.4	0.44/0.53	[113]
Cu28	ITO/PEDOT:PSS/**Cu28** 5wt%:PYD2/DPEPO/TPBi/LiF/Al	–	–	5580	15.6	43.3	19.8	0.48/0.51	[113]
Cu30	ITO/PEDOT:PSS/**Cu30** 2.5wt%:PYD2/DPEPO/TPBi/LiF/Al	–	–	3030	5.10	14.8	5.10	0.44/0.53	[113]
Cu31	ITO/PEDOT:PSS/**Cu31** 12wt%:PYD2/DPEPO/TPBi/LiF/Al	–	535	8650	18.5	58.5	23.0	0.37/0.56	[114]
Cu32	ITO/PEDOT:PSS/**Cu32** 12wt%:PYD2/DPEPO/TPBi/LiF/Al	–	582	17600	14.3	35.3	10.0	0.51/0.48	[114]
Cu33	ITO/PEDOT:PSS/**Cu33** 4wt%:CBP/TPBi/LiF/Al	–	631	4630	10.2	11.3	4.10	0.61/0.38	[114]
Cu34	ITO/PEDOT:PSS/PLEXCORE UT-314/**Cu34** 30wt%:PYD2/3TPYMB/Al	2.6	–	10000	23	73	–	–	[31,115]
Cu35	ITO/PEDOT:PSS/**Cu35** 8 mg/mL:decalin/TSPO1/TPBi/LiF/Al	4	–	1000	13.9	45	–	–	[117]
Cu36	ITO/MoO_3/TAPC/TCTA/**Cu36** 10wt%:mCP/TmPyPb/LiF/Al	5.1	–	2339	10.1	32.9	19.9	0.31/0.54	[118]
Cu37	ITO/MoO_3/TAPC/TCTA/**Cu37** 10wt%:mCP/TmPyPb/LiF/Al	5.4	–	2399	7.3	20.4	11.2	0.31/0.50	[118]
Cu38	ITO/MoO_3/TAPC/TCTA/**Cu38** 10wt%:mCP/TmPyPb/LiF/Al	3.9	–	3256	8.3	22.9	16.0	0.38/0.51	[118]
Cu39	ITO/HATCN/NPB/TCTA/Ir(bpiq)2acac 5wt%:TCTA/**CuI** 6wt%:CzBPDCb/TPBi/Liq/Al	3.4	525	18186	17.6	53.8	48.3	–	[119]
Cu40	ITO/HATCN/NPB/TCTA/Ir(bpiq)2acac 5wt%:TCTA/**CuI** 6wt%:CzBPCb/TPBi/Liq/Al	3.6	525	4450	3.2	8.58	6.24	–	[119]
Cu41	ITO/PEDOT:PSS/TCTA/**Cu41** 10wt%:/TmPyPb/LiF/Al	5.2	544	11010	14.8	47.0	21.6	0.37/0.55	[120]
Cu42	ITO/PEDOT:PSS/TCTA/**Cu42** 10wt%:mCP/TmPyPb/LiF/Al	5.6	544	5152	11.2	35.6	14.5	0.38/0.55	[120]
Cu43	ITO/PEDOT:PSS/TCTA/**Cu43** 10wt%:mCP/TmPyPb/LiF/Al	5.3	544	5242	6.67	21.3	12.1	0.38/0.54	[120]
Cu44	ITO/PEDOT:PSS/**Cu44** 20 wt%:PYD2/3TPYMB/LiF/Al	8.5	523	2342	7.6	24.8	–	0.30/0.54	[121]
Cu45	ITO/PEDOT:PSS/**Cu45** 20wt%:PYD2/3TPYMB/LiF/Al	7.7	526	2012	6.2	20.4	–	0.30/0.54	[121]
Cu46	ITO/PEDOT:PSS/**Cu46** 20wt%:PYD2/3TPYMB/LiF/Al	7.3	522	2525	8.3	27.1	–	0.29/0.53	[121]
Cu49	ITO/PEDOT:PSS/**Cu49** 15wt%:BCPO/TPBi/LiF/Al	4.0	–	12800	10.5	–	–	0.32/0.53	[125]
Cu50	ITO/PEDOT:PSS/**Cu50** 15wt%:BCPO/TPBi/LiF/Al	4.0	–	7740	9.5	–	–	0.33/0.54	[125]
Cu51	ITO/PEDOT:PSS/TFB/**Cu51** 20wt%:PVK/BPhen/LiF/Al	3.4	–	7790	9.7	30.4	11.8	–	[129]
Cu52	ITO/PEDOT:PSS/TFP/**Cu52** 20wt%:PVK/BPhen/LiF/Al	3.8	–	8100	5.6	–	–	0.37/0.60	[130]
Cu53	ITO/HATCN/TAPC/**Cu53** 40vol%:mCP/TPBi/Liq/Al	2.5	543	54000	19.4	–	–	–	[131]
Cu54	ITO/PEDOT:PSS/**Cu54** 20wt%:TCTA/TPBi/LiF/Al	6.5	520	1437	–	1	–	–	[133]
Cu55	ITO/PEDOT:PSS/**Cu55** 20wt%:TCTA/TPBi/LiF/Al	6.0	539	1871	–	2.1	–	–	[133]
Cu56	ITO/PEDOT:PSS/**CuCl** 5wt%:aza-SBF/TCTA/TPBi/Liq/Al	5.1	–	6799	9.5	24.3	12.9	–	[134]
Cu57	ITO/PEDOT:PSS/**CuBr** 7wt%:aza-SBF/TCTA/TPBi/Liq/Al	4.4	–	13670	13.6	37.2	25.1	–	[134]
Cu58	ITO/PEDOT:PSS/**CuI** 9wt%:aza-SBF/TCTA/TPBi/Liq/Al	4.0	–	7891	10.7	30.7	21.6	–	[134]
Cu59	ITO/MoO_3/MoO_3 20wt%:mCP/mCP/**Cu59** 9wt%:mCP/DPEPO/TPBi/LiF/Al	4.4	515	1380	7.44	26.3	–	–	[137]
Cu60	ITO/MoO_3/MoO_3 20wt%:mCP/mCP/**Cu60** 10wt%:mCP/DPEPO/TPBi/LiF/Al	4.4	540	3665	14.5	32.2	–	–	[137]

[a)]Reported data were selected from the corresponding references, in favor of the highest EQE or highest CE when EQE was not given; [b)]The dopant complex **Cu22** was prepared in situ using the starting materials. V_{on}: turn-on voltage; λ_{max}, electroluminescence maximum emission; L_{max}, maximum luminance; EQE, maximum external quantum efficiency; CE, maximum current efficiency; PE, maximum external power efficiency; CIE, Commission Internationale de l'Eclairage.

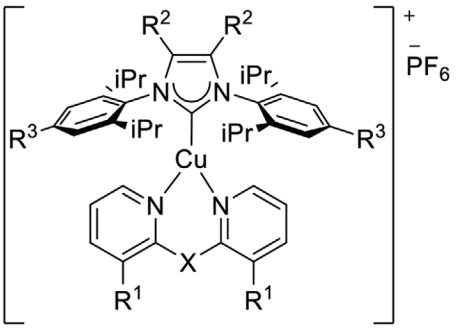

R = H unless specified
Cu6: X = NH
Cu7: X = NH // R^2 = Me, R^3 = OMe
Cu8: X = NH // R^1 = Me
Cu9: X = CH_2
Cu10: X = CMe_2
Cu11: X = PPh

Scheme 2. Description of copper(I) complexes **Cu6–11**.

devices with **Cu5** reached the highest EQEs of 7.82%. The fact that complexes **Cu4** and **Cu5** outperformed **Cu1–Cu3** in both, photophysical and electroluminescence behaviors, encouraged the authors to conclude that the DMAC moiety is critical for achieving good performances using this type of complexes in OLEDs.

Blue-Emitting LECs: While the first Cu(I)-based blue-emitting OLEDs with TADF emission were published in 2013, it was not until 2016 that the first Cu(I)-based blue-emitting LECs were published by Gaillard and Costa groups.[102] The authors reported a series of tricoordinated copper(I) complexes [Cu(NHC)(dpa)][PF_6] based on *N*-heterocyclic carbene (NHC) and dipyridylamine (dpa) derivatives as ligands (**Scheme 2**). The influence of different substituents on both NHC and dpa ligands were investigated to modulate the λ_{max} and PLQY values of this family of complexes. A detailed understanding of the design of these complexes allowed tuning of the emission from blue (λ_{em} = 463 nm) to green (λ_{em} = 550 nm). Breaking the geometry of the complexes by the plane angle, defined by the authors, and/or H...F interactions between the dpa ligand and the counter ion appeared to increase the PLQY (in powder) of this family. In this series, **Cu6**, **Cu7**, and **Cu8** (Scheme 2) exhibited TADF with λ_{max} centered at 463, 479, and 458 nm; PLQYs of 22, 64, and 86%; τ_{obs} of 13, 30, and 44 µs; and ΔE_{ST} of 0.35 eV, respectively. They were selected to prepare the first blue-emitting LECs with the architecture ITO/PEDOT:PSS/copper(I) complex (100 nm)/Al (**Table 3**). Under current–voltage–luminance (IVL) assays, devices with **Cu6** and **Cu8** showed the highest L_{max} of 56 and 310 cd m^{-2}, respectively. In general, the devices possessed low stability as a drop of luminance was observed along with a red-shift of the λ_{max} over repetitive IVL assays. This degradation was assigned to a poor redox reversibility of the complexes. Nevertheless, these devices were driven at pulsed current densities; the bluest emission at λ_{max} of 493 nm was measured for devices with **Cu7** (x/y CIE color coordinates: 0.23/0.29), achieving the lowest performance including L_{max} of 10 cd m^{-2}, efficiencies of 0.006 cd A^{-1}, and lifetimes ($t_{1/2}$) of 1.3 min. Devices with **Cu8** showed λ_{max} centered at 497 nm (x/y CIE color coordinates: 0.23/0.28) and the highest performance in terms of L_{max}, efficiencies, and $t_{1/2}$ with values of 50 cd m^{-2}, 0.29 cd A^{-1}, and 2.7 min, respectively.

The following year, the same authors studied the role of the bridging atom in the bis-pyridyl ligand in a series of copper(I) complexes [Cu(NHC)(N^N)][PF_6]. Using as reference the nitrogen-based complex **Cu6** (X = NH, Scheme 2),[102] three more bridging groups of the bis-pyridyl N^N ligand were

Table 3. Figures of merit of LEC devices based on Cu(I) complexes with TADF.

Complex[a)]	Device architecture	Operating conditions	λ_{max} [nm]	L_{max} [cd m^{-2}]	t_{on} [h]	$t_{1/2}$ [h]	EQE [%]	CE [cd A^{-1}]	PE [lm W^{-1}]	CIE [x/y]	Ref
Cu6	ITO/PEDOT:PSS/**Cu6**/Al	166.4 mA cm^{-2}[c)]	495	5.9	<1 s	1.3 min	–	0.004	3.23	0.24/0.29	[102]
Cu7	ITO/PEDOT:PSS/**Cu7**/Al	166.5 mA cm^{-2}[c)]	493	10	<1 s	1.2 min	–	0.006	3.04	0.23/0.29	[102]
Cu8	ITO/PEDOT:PSS/**Cu8**/Al	–	497	170	–	–	–	1.30	–	0.23/0.28	[102,109]
Cu9	ITO/PEDOT:PSS/**Cu9**/Al	5 mA[c)]	–	2.2	–	36 s	–	0.001	–	0.30/0.42	[103]
Cu10	ITO/PEDOT:PSS/**Cu10**/Al	0.5 mA[c)]	–	6.2	–	240 s	–	0.19	–	0.23/0.39	[103]
Cu11	ITO/PEDOT:PSS/**Cu11**/Al	0.5 mA[c)]	–	13	–	42 s	–	0.39	–	–	[103]
Cu61	ITO/PEDOT:PSS/**Cu61**/Al	IVL	555	2.7	–	–		–	–	–	[102]
Cu62	ITO/PEDOT:PSS/**Cu62** 4/1 [EMIM][PF_6]/Al	100 A m^{-2}[c)]	595	65	0.37	8.5	0.4	0.70	0.20	–	[138]
Cu63	ITO/PEDOT:PSS/**Cu63** 4/1 [EMIM][PF_6]/Al	100 A m^{-2}[c)]	589	109	2.28	31	0.5	1.10	0.40	–	[138]
Cu64	ITO/PEDOT:PSS/**Cu64** 4/1 [EMIM][PF_6]/Al	100 A m^{-2}[c)]	593	131	0.13	2	0.6	1.30	0.40	–	[138]
Cu65	ITO/PEDOT:PSS/**Cu65** 4/1 [EMIM][PF_6]/Al	100 A m^{-2}[c)]	586	121	<5 s	0.28	0.5	1.20	0.30	–	[141]
Cu66	ITO/PEDOT:PSS/**Cu66** 4/1 [EMIM][PF_6]/Al	100 A m^{-2}[c)]	587	259	12 s	0.08	1.2	2.70	0.60	–	[141]

Table 3. Continued.

Complex[a)]	Device architecture	Operating conditions	λ_{max} [nm]	L_{max} [cd m^{-2}]	t_{on} [h]	$t_{1/2}$ [h]	EQE [%]	CE [cd A^{-1}]	PE [lm W^{-1}]	CIE [x/y]	Ref
Cu71	ITO/PEDOT:PSS/**Cu71** 4/1 [EMIM][PF_6]/Al	50 A m^{-2}[b)]	585	17	15.9	200	–	0.30	–	–	[145]
Cu72	ITO/PEDOT:PSS/**Cu72** 4/1 [EMIM][PF_6]/Al	50 A m^{-2}[b)]	585	63	1.00	102	–	1.30	–	–	[145]
Cu73	ITO/PEDOT:PSS/**Cu73** 4/1 [EMIM][PF_6]/Al	50 A m^{-2}[b)]	585	37	3.40	104	–	0.70	–	–	[145]
Cu74	ITO/PEDOT:PSS/**Cu74** 4/1 [EMIM][PF_6]/Al	50 A m^{-2}[b)]	585	32	0.40	14	–	0.60	–	–	[145]
Cu75	ITO/PEDOT:PSS/**Cu75** 4/1 [EMIM][PF_6]/Al	50 A m^{-2}[b)]	585	14	0.30	6	–	0.20	–	–	[145]
Cu76	ITO/PEDOT:PSS/**Cu76** 4/1 [EMIM][PF_6]/Al	50 A m^{-2}[b)]	585	22	3.90	60	–	0.40	–	–	[145]
Cu77	ITO/PEDOT:PSS/**Cu77** 4/1 [EMIM][PF_6]/Al	50 A m^{-2}[b)]	585	45	4.20	48	–	0.90	–	–	[145]
Cu78	ITO/PEDOT:PSS/**Cu78** 4/1 [EMIM][PF_6]/Al	50 A m^{-2}[b)]	585	79	0.50	54	–	1.60	–	–	[145]
Cu79	ITO/PEDOT:PSS/**Cu79** 4/1 [EMIM][PF_6]/Al	50 A m^{-2}[b)]	585	80	1.80	47	–	1.60	–	–	[145]
Cu80	ITO/PEDOT:PSS/**Cu80** 4/1 [EMIM][PF_6]/Al	50 A m^{-2}[b)]	585	44	0.90	20	–	0.90	–	–	[145]
Cu81	ITO/PEDOT:PSS/**Cu81** 4/1 [EMIM][PF_6]/Al	50 A m^{-2}[b)]	585	39	0.70	14	–	0.80	–	–	[145]
Cu82	ITO/PEDOT:PSS/**Cu82** 4/1 [EMIM][PF_6]/Al	50 A m^{-2}[b)]	585	56	3.10	80	–	1.10	–	–	[145]
Cu83	ITO/PEDOT:PSS/**Cu83** 4/1 [EMIM][PF_6]/Al	100 A m^{-2}[b)]	584	20	0.02	0.08	–	0.20	–	–	[146]
Cu84	ITO/PEDOT:PSS/**Cu84** 4/1 [EMIM][PF_6]/Al	100 A m^{-2}[b)]	575	230	0.08	0.90	–	2.30	–	–	[146]
Cu85	ITO/PEDOT:PSS/**Cu85** 4/1 [EMIM][PF_6]/Al	100 A m^{-2}[b)]	557	370	0.02	0.82	–	3.70	–	–	[146]
Cu86	ITO/PEDOT:PSS/**Cu86** 4/1 [EMIM][PF_6]/Al	100 A m^{-2}[b)]	582	50	0.01	0.58	–	0.50	–	–	[146]
Cu88	ITO/PEDOT:PSS/CBP/**Cu88**/Al	7.5 mA[b)]	573	32.9	1.6	10.8	–	0.30	–	0.46/0.52	[147]
Cu90	ITO/PEDOT:PSS/**Cu90**/Al[c)]	15 mA	675	97.9[d)]	–	20.9	–	–	0.23	0.66/0.32	[150]
Cu90	ITO/PEDOT:PSS/**Cu90** 15/85 CBP/Al[e)]	–	–	4	–	–	–	–	–	0.31/0.32	[150]

[a)]Reported data were selected from the corresponding references, in favor of the highest EQE or highest CE when EQE was not given; [b)]Pulse mode; [c)]Complex **Cu90** was used in a red-emitting LEC device; [d)]Luminance given in irradiance [μW cm^{-2}]; [e)]Complex **Cu90** was used in a white-emitting LEC device. λ_{max}, maximum emission; L_{max}, maximum luminance; t_{on}, time to reach the maximum luminance; $t_{1/2}$, time to reach half of the maximum luminance; EQE, maximum external quantum efficiency; CE, maximum current efficiency; PE, maximum external power efficiency; CIE, Commission Internationale de l'Eclairage.

studied with X = CH_2 for **Cu9**, X = $C(CH_3)_2$ for **Cu10**, and X = PPh for **Cu11** (Table 1 and Scheme 2).[103] The authors established clear relationships between the structural changes of the complexes in both the ground and excited states induced by the bridging group and both the PLQY and the device performance. Interestingly, the TADF mechanism was noted for each complex, showing ΔE_{ST} values of 0.07 eV for **Cu9** and 0.06 eV for **Cu11** and τ_{TADF} values of 6, 14, and 13 μs for **Cu9**, **Cu10**, and **Cu11**, respectively. As an example, **Cu9** and **Cu10** showed the same emission centered at 475 and 483 nm at RT and 77 K, respectively. However, the planar-like complex **Cu9** exhibited low PLQY of 15%, while the boat-like **Cu10** exhibited a PLQY of 73%. This was related to the presence of two methyl groups, which brings a more pronounced symmetry breaking, therefore, leading to a pyramidal geometry of the bridging group. In addition, the authors also noted that the different molecular structures strongly impact the ionic mobility in thin films ranging from 4×10^{-9} to 8×10^{-8} S m^{-1} for **Cu9** and **Cu10**, respectively. This is of particular interest to select the appropriate current to ensure enough charge injection at the lower current possible, avoiding stability issues due to over oxidation/reduction processes. For instance, devices driven at low applied currents of 5 mA showed a greenish-blue emission (x/y CIE color coordinates: 0.30/0.42) with L_{max} of 21 cd m^{-2} and $t_{1/2}$

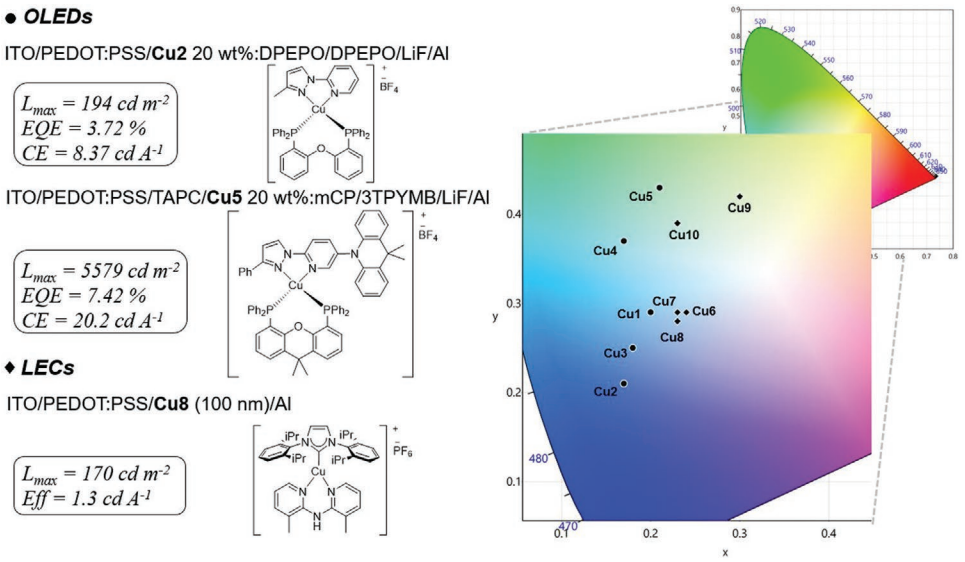

Figure 6. Graphical summary of the benchmark copper(I)-based blue-emitting OLEDs and LECs devices; devices with highest efficiencies are represented on the left.

of 324 s for **Cu10**, while those with **Cu9** showed a more blue-shifted emission (x/y CIE color coordinates: 0.23/0.28) with L_{max} of 2.2 cd m^{-2} and a $t_{1/2}$ of 36 s (Table 3).

A detailed representation in the CIE color space of the blue-emitting devices (OLEDs and LECs) based on Cu(I) complexes is given in **Figure 6**, with a highlight on the best performing devices in each category.

Green and Yellow-Emitting OLEDs: A large family of complexes based on bidentate diphenylphosphinobenzene (dppbz) derivatives with TADF emission has been developed by Osawa and co-workers.[104–107] In 2013, a series of tetra-coordinate Cu(I) complexes **Cu12–14** with diphenyl-bis(pyrazol-1-yl) borate ($pz_2Bph_2^-$) and three dppbz derivatives were reported (Table 1 and **Scheme 3**).[104] The authors investigated the influence of the fluorine (**Cu13**) and CF_3 (**Cu14**) substituents at the dppbz ligand on the photophysical properties and device performances. **Cu12** without any substituent was used as a reference. Fluorinated substituents had a limited effect but not negligible on the photophysical properties, for instance; in thin films at 298 K: λ_{max}(nm){ϕ(%)}[τ(µs)] = 545{50}[3.8] for **Cu12**, 534{63}[3.6] for **Cu13**, 523{68}[8.2] for **Cu14**. Although complexes **Cu13** and **Cu14** exhibited emission λ_{max} at 77 K similar to those at 298 K with exception of **Cu12** (λ_{max} = 550 nm), all complexes showed a general red-shift of the beginning edges of emission spectra. Additionally, the $\tau_{77\,K}$ were increased to 170, 400, and 270 µs, which suggested the existence of TADF. This was confirmed by small ΔE_{ST} values of 3.70, 4.64, and 4.32 kcal mol^{-1}. However, these fluorinated

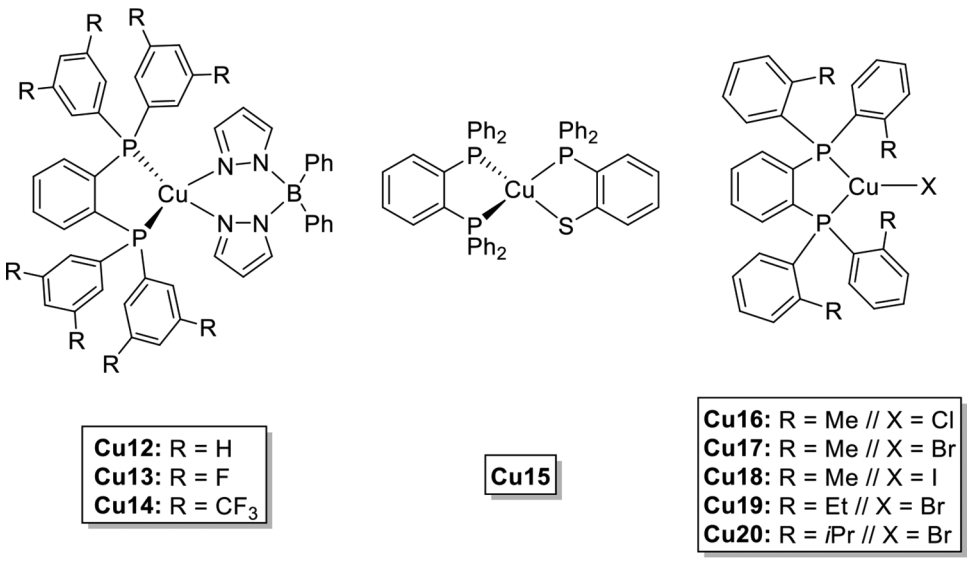

Scheme 3. Description of copper(I) complexes **Cu12–20.**

substituents showed huge impact on the oxidation potentials values: E_{ox} (vs Fc/Fc^+) = +0.36 V (**Cu12**), +0.86 (**Cu13**), and +1.20 V (**Cu14**). The electrochemical analysis, combined with DFT calculations, showed that these substituents stabilize both the HOMO and the LUMO, leading to small changes in the HOMO-LUMO gap, explaining the weak influence on the emissions shifts. The introduction of fluorinated substituents increased the thermal stability and sublimability of the complexes; this allowed the preparation of sublimated OLEDs using mCP as a host. These OLEDs feature a similar green emission at low turn-on voltages (V_{on}) of 3.4, 3.2, and 2.6 V for devices with **Cu12**, **Cu13**, and **Cu14**, respectively. The maximum EQEs of 11.9%, 16.0%, and 17.7% were achieved for devices with **Cu12**, **Cu13**, and **Cu14**, respectively, (Table 2). Both the PLQYs and the EQEs suggest that increasing the number of fluorine atoms is beneficial to the photoluminescence of the complexes and the electroluminescence of the devices.

The same year, the authors reported a comparative study between copper(I), silver(I), and gold(I) complexes **Cu15**, **Ag1**, and **Au1**, in which $pz_2Bph_2^-$ was replaced by the strong electron donor 2-diphenylphosphinobenzenethiolate (dppbzS) (Table 1 and Scheme 3).[105] This led to very little contribution of the metal orbital to the HOMOs. As a consequence, the MLCT character is only 2% in this series, in contrast to 30–38% in complexes **Cu12–14**.[104] Nevertheless, complexes **Cu15**, **Ag1**, and **Au1** featured TADF emissions centered at 521, 505 and 630 nm, owing to small ΔE_{ST} of 309, 199, and 405 cm^{-1}, respectively. Unfortunately, **Ag1** showed a low solubility, whereas **Au1** featured a quick degradation in solution. For these reasons, **Cu15** was the only one implemented in OLEDs, achieving green luminescence (x/y CIE color coordinates: 0.40/0.53) with an EQE of 7.8% (Table 2). This value is much smaller than those of their counterparts **Cu12–14**, indicating that the dppbzS ligand is not suitable for the design of organometallic TADF emitters.

In 2015, three coordinate Cu(I) complexes (**Cu16–Cu20**; Table 1 and Scheme 3) bearing bidentate dppbz ligands (1,2-bis[bis(2-methylphenyl)phosphino]benzene, 1,2-bis[bis(2-ethylphenyl) phosphino]benzene, and 1,2-bis[bis(2-isopropylphenyl)phosphino]benzene]) and halides Cl, Br, and I were reported by Osawa et al. Complexes showed a TADF behavior and were employed for OLED devices.[106] These complexes featured blue to green TADF emission in powder, with PLQYs ranging between 38% and 95%, and the ΔE_{ST} was less than 830 cm^{-1}. In this family of complexes, the origin of the emission is the $(\sigma(Cu)+X)\rightarrow\pi^*$ transition. Bulkier diphosphine ligands lead to increased PLQY values. Noteworthy, **Cu20** reached a PLQY value of almost 100% which is in good agreement with the general statement that steric hindrance around the coordination sphere of Cu(I) increases the PLQY of the TADF emission. It is important to mention that the influence of the halide is noticed through the τ analysis at 77 K. In fact, the k_r values follow the trend (Cl < Br < I) suggesting that the SOC of the halides affects the emissions. All the OLEDs exhibited TADF green luminescence (513–529 nm; x/y CIE color coordinates: 0.25/0.51–0.32/0.54) with high EQE values (18.6–22.5%) (see Table 2).

Two years after publishing the family of TADF blue-emitting copper(I) complexes **Cu1–Cu3**,[30] Lu and co-workers synthesized two new green-emitting complexes [Cu(czpzpy)$(PPh_3)_2$][BF_4] **Cu21** and [Cu(czpzpy)(POP)][BF_4] **Cu22**, in which czpzpy is a diimine ligand functionalized with a carbazole (Cz) group (Table 1 and **Scheme 4**).[108] Both complexes showed a TADF emission (ΔE_{ST} = 0.18 and 0.13 eV, τ_{obs} = 134 and 23 µs), achieving a PLQY of 98% for **Cu22**. Complex **Cu22**, showing the best thermal stability with the highest decomposition temperature (T_d) of 349 °C, was applied to OLEDs following two approaches. First, the complex was used in 20 wt% as dopant and the ligand czpzpy as host, that is, the ITO/PEDOT:PSS/**Cu22**, 20wt%:czpzpy/DPEPO/LiF/Al device A. Second, the authors prepared device B by spin-coating a mixture of the ligand and the starting material [$Cu(CH_3CN)_2$(POP)][BF_4]. The working hypothesis aimed to achieve the same device architecture while synthesizing complex **Cu22** during the deposition process and using the excess of czpzpy as a host to inhibit dissociation of the N^N ligand, which is a typical decomposition pathway for this type of copper(I) complexes.[109–111] Both devices showed green emissions (λ_{max} = 514 nm, x/y CIE color coordinates: 0.26/0.49; and λ_{max} = 516 nm, x/y CIE color coordinates: 0.25/0.49) for devices A and B, respectively. Interestingly, both devices achieved similar performances with L_{max} of ≈3000 cd m^{-2} and EQE value of 6.34% (Table 2).

Copper(I) complexes **Cu23–Cu25** (Table 1 and **Scheme 5**) displaying dual TADF and phosphorescence emissions were reported by Xu and co-workers in 2017.[112] These neutral complexes have a general formula of [CuX(TTPP)], in which TPPP is the tridentate phosphine 2,2′-(phenylphosphinedyl) bis(2,1-phenylene)bis(diphenylphosphine) and X a halide atom (X = Cl **Cu23**, X = Br **Cu24**, and X = I **Cu25**). The triphosphine ligand offers a rigid and stable tetrahedral geometry to the complexes as well as a strong thermal stability, while the halide groups modify the SOC of the complexes. As a consequence, the contribution of each emission process (TADF and phosphorescence) can be modulated. For instance, **Cu23** shows

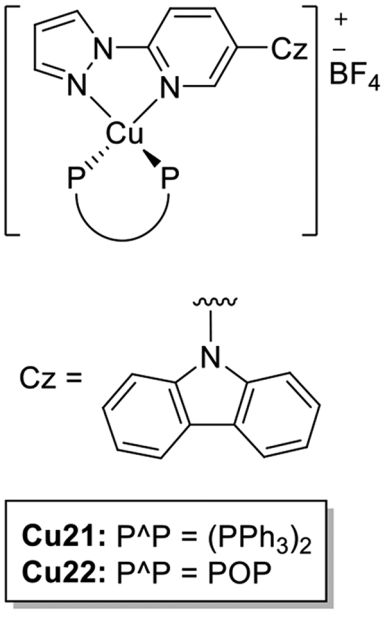

Scheme 4. Description of copper(I) complexes **Cu21** and **Cu22**.

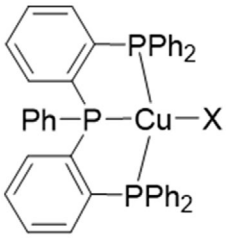

Cu23: X = Cl
Cu24: X = Br
Cu25: X = I

Scheme 5. Description of copper(I) complexes **Cu23–25.**

almost pure TADF emission (94%) at RT, while **Cu25** displays 34% of phosphorescence. This is also reflected in its high PLQY (83%) due to a large ΔE_{ST} and strong SOC. All compounds display similar yellow color (λ_{max} = 584 nm, x/y CIE color coordinates: 0.47/0.49) in OLED devices with the architecture ITO/MoO_3/TAPC/**Cu23–25** 10wt%:mCP/2,2′,2″-(1,3,5-benzinetriyl)-tris(1- phenyl-1-H-benzimidazole) (TPBi)/LiF/Al, Table 2. All compounds showed comparable electron-only conductivity. The hole-only transport is, however, higher for devices with **Cu23** and **Cu25** due to the strong electronegativity of the chlorine atom and the large polarizability of the iodine atom. All devices featured a V_{on} of 3.5 V and reached 1000 cd m^{-2} at low voltages (6–7 V). Devices with **Cu25** exhibited remarkable EQE values of 16.3%. With an electron–hole recombination of 98%, the device reaches a complete singlet–triplet harvesting and achieves very low EQE roll-offs of 6% at 1000 cd m^{-2}.

Che and co-workers proposed a family of heteroleptic TADF copper(I) complexes based on phenanthrolines (phen), bipy, and neocuproine ligands associated in concert with 7,8-bis(diphenylphosphino)-7,8-dicarbanido-unido-undecaborate (dppnc) (Table 1 and **Scheme 6**).[113,114] In 2015, the first series of copper(I) complexes **Cu26–Cu29** highlighted the influence of substituents of the diimine ancillary ligand on the PLQY of these TADF emitters.[113] In detail, complexes **Cu27** and **Cu28** with neocuproine moiety exhibited emissions with PLQY around 5% in dichloromethane solution, whereas those with phen (**Cu26** and **Cu29**) were not emissive. Thus, poor device performances were noted for these complexes. The authors pointed out that the presence of methyl groups brings steric hindrance, preventing the flattening distortions of the complexes in the excited states. This assumption was corroborated by DFT calculations showing that the P2-N2-N1-P2 dihedral angle presented considerable changes in **Cu26** and **Cu29** for both excited states compared to ground state $\Delta(S_0–S_1)$ = 20.2° and 19.8°; $\Delta(S_0–T_1)$ = 12.8° and 12.7°, respectively. In contrast, these geometries are more rigid in the case of **Cu27** and **Cu28** with $\Delta(S_0–S_1)$ = 3.4° and 3.3° and $\Delta(S_0–T_1)$ = 2.6° and 1.1°, respectively. To support this theoretical study, the authors synthesized the copper(I) complex **Cu30**, replacing the neocuproine by 6,6′-dimethyl-2,2′-bipyridine, which showed performances similar to **Cu27** and **Cu28**. The emission mechanism in complexes **Cu27**, **Cu28**, and **Cu30** involved TADF. Solution-processed OLEDs consisting of ITO/PEDOT:PSS/Cu(I) complex 2.5–5 wt%:PYD2/DPEPO/TPBi/LiF/Al were fabricated and these devices reached EQE values of 16.6%, 15.6%, and 5.10% for **Cu27**, **Cu28**, and **Cu30**, respectively (Table 2). The low performance of the device incorporating complex **Cu30** was explained by the lack of energy transfer between the complex and the host PYD2.

After showing that substitutions in position 2 of the phen strongly influences the emission mechanism, the authors evaluated the impact of substitutions in position 4 on the emission features of the neocuproine derivatives.[114] Three complexes were synthesized with different substituents in the position 4 of neocuproine: (2-ethylhexyl)oxy **Cu31**, 9,9-dihexyl-9H-fluoren-2-yl **Cu32**, and (4-(9H-carbazol-9-yl)phenyl)ethynyl **Cu33** (Table 1 and Scheme 6). Compounds **Cu31–Cu33** showed TADF emissions in the blue region λ_{max} = 497 nm (**Cu31**), yellow λ_{max} = 588 nm, and red region λ_{max} = 657 nm (**Cu33**). The solution-processed OLEDs were prepared using PYD2 as host and the emitters **Cu31–Cu33** as guest with the following architecture: ITO/PEDOT:PSS/copper(I) complex 4–20wt%:PYD2/DPEPO/TPBi/LiF/Al. The optimum performances were achieved at 12 wt% of **Cu31** or **Cu32**. In this configuration, the green-emitting

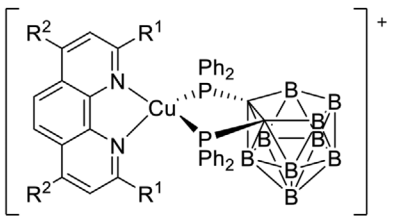

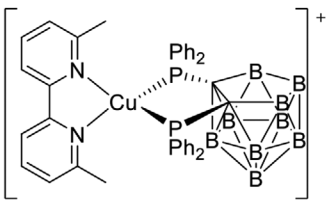

Cu26: R^1 = H // R^2 = H
Cu27: R^1 = Me // R^2 = H
Cu28: R^1 = Me // R^2 = Ph
Cu29: R^1 = H // R^2 = Ph
Cu31: R^1 = Me // R^2 = (2-ethylhexyl)oxy
Cu32: R^1 = Me // R^2 = 9,9-dihexyl-9*H*-fluoren-2-yl
Cu33: R^1 = Me // R^2 = (4-(9*H*-carbazol-9-yl)phenyl)ethynyl

Cu30

Scheme 6. Description of copper(I) complexes **Cu26–33**.

device (λ_{max} = 535 nm, x/y CIE color coordinates: 0.37/0.56) incorporating **Cu31** exhibited a L_{max} of 8650 cd m^{-2} with an EQE of 18.5%. The devices prepared with **Cu32** showed a yellow emission (λ_{max} = 582 nm, x/y CIE color coordinates: 0.51/0.48) with a L_{max} of 17 600 cd m^{-2} and an EQE of 14.3%. Devices using **Cu33** featured a red mission (λ_{max} = 631 nm, x/y CIE color coordinates: 0.61/0.38) with a L_{max} of 4630 cd m^{-2} and EQE of 10.2% (Table 2). More details are provided in the next section corresponding to the red-emitting devices.

Bauman and co-workers synthesized a binuclear heteroleptic complex Cu_2I_2(MePyrPHOS)(dpph) **Cu34** (MePyrPHOS = 2-diphenylphosphino-4-methylpyridin, dpph = 1,6-bis diphenylphosphinohexan), in which the NHet-PHOS and the dpph are supported by a $\{Cu_2I_2\}$ central core (Table 1 and **Scheme 7**).[31,115] Unlike in mononuclear copper(I) complexes, binuclear copper(I) complexes feature the HOMO entirely delocalized on the $\{Cu_2I_2\}$ core, limiting the flattening-distortions during oxidation processes.[115,116] The two bidentate ligands dpph and NHet-PHOS render the complex more rigid, something which is most problematic in mono- and multinuclear copper(I) complexes.[31] As a consequence, complex **Cu34** is stable under ambient atmosphere; additionally, it is both electrochemically and thermally stable with no degradation detected under 290 °C. **Cu34** exhibits green emissions with λ_{max} = 519 nm and PLQYs of 88% in powder and 92% in PYD2 doped thin films. Temperature-dependent τ analysis revealed that their emission mechanism involves both TADF and phosphorescence with respective τ of 31 and 110 µs for both

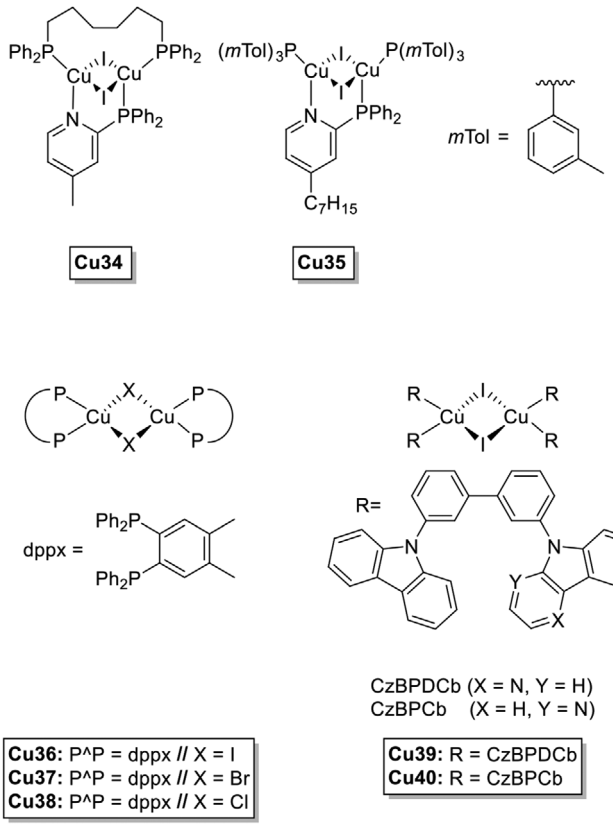

Scheme 7. Description of copper(I) complexes **Cu34–40**

processes and ΔE_{ST} of 830 cm^{-1}. Complex **Cu34** was used as a dopant in a solution-processed OLED device with the configuration ITO/PEDOT:PSS/PLEXCORE UT-314/**Cu34** 30wt%:PYD2/tris(2,4,6-trimethyl-3-(pyridin-3-yl)phenyl)borane (3TPYMB)/Al (Table 2). The resulting green-yellowish emitting device (λ_{max} = 550 nm) showed very good performances with L_{max} of 10 000 cd m^{-2} at 10 V and EQE of 23%. Importantly, this is the highest value reported to date in solution processed TADF OLEDs with copper(I) complexes.

Following this achievement, in 2016 Baumann, Volz, and co-workers developed another TADF green-emitting OLED by inkjet-printing technique using another NHet-PHOS Cu(I) binuclear complex **Cu35** (Table 1 and Scheme 7).[117] The authors designed a highly soluble compound by introducing non-symmetrical substituted phosphine and pyridine with alkyl groups. This structural modification resulted in a very good solubility in both polar and nonpolar solvents, which is crucial for inkjet-printing. With an estimated ΔE_{ST} of 100 ± 50 meV, **Cu35** features TADF emissions with λ_{max} = 547 nm, x/y CIE color coordinates: 0.36/0.47, and a PLQY of 69% in powder. Additionally, the PLQY increases in thin films reaching values as high as 92% in films with either PMMA or PYD2 hosts. The OLEDs were prepared by printing **Cu35** using an ink based on decalin that is fully compatible with PEDOT:PSS. The device showed a low V_{on} of 4 V and reaches around 1000 cd m^{-2} of L_{max} with EQE of 13.9% Table 2.

In 2016, Lo and co-workers synthesized a series of neutral dinuclear copper(I) complexes of general formula [Cu(μ-X)(dppbz)]$_2$ (Table 1 and Scheme 7), in which X was I (**Cu36**), Br (**Cu37**), and Cl (**Cu38**).[118] At RT, complexes **Cu36–38** display blue to green TADF emissions (λ_{max} ranging from 498 to 527 nm) originated from the (σ+X)→π^* transition with moderate PLQYs (28–32%) and τ between 2.5 and 12.5 µs. Vacuum-processed OLEDs were prepared with the architecture ITO/MoO_3/TAPC/TCTA/**Cu36–38** 10wt%:mCP/TmPyPb/LiF/Al (Table 2). All devices reach L_{max} of over 2000 cd m^{-2}. The highest EQEs of 10.1% was measured for devices with **Cu36**. Overall, the efficiencies of the devices are in good agreement with the PLQY, i.e., **Cu38** > **Cu36** > **Cu37**.

Another example of binuclear Cu(I) complexes exhibiting TADF emission and their application in OLEDs was reported in 2017 by Wei et al.[119] The ligands 5-(3′-(9H-carbazol-9-yl)-[1,1′-biphenyl]-3-yl)-5H-pyrido[3,2-b]indole (CzBPDCb) and 9-(3′-(9H-carbazol-9-yl)-[1,1′-biphenyl]-3-yl)-9H-pyrido[2,3-b]indole (CzBPCb) were co-deposited in the presence of CuI to serve as both the ligand and the host, following the same strategy used by Lu in 2015.[30] The in situ generation of copper(I) complexes leads to the formation of [CuI_2(CzBPDCb)$_4$] **Cu39** and [CuI_2(CzBPCb)$_4$] **Cu40**, respectively (Table 1 and Scheme 7). While neat films of CzBPDCb and CzBPCb showed fluorescence emission centered at 382 nm with lifetimes of 4 and 6 ns for ligands CzBPDCb and CzBPCb, respectively, the emission of the co-deposited films with 4 or 8 wt% of CuI_2 featured green emissions centered around 520 nm for both compounds with lifetimes of 1.05 and 0.61 µs for **Cu39** and **Cu40**, respectively. This emission was confirmed to involve TADF as a 30 nm red-shift of the λ_{max} observed upon freezing the films at 77 K along with a considerable increase of the lifetimes up to 52.7 and 109.6 µs for

Cu39 and **Cu40**, respectively. The corresponding ΔE_{ST} were estimated at 0.12 and 0.23 eV. Noteworthy, at 8 wt%, **Cu40** featured the emission band at 382 nm corresponding to the free ligand, which suggested poor coordinating ability. Thus, both photoluminescence and device analyses showed that CzBPCb is a better ligand and host than its isomer. Concerning the best performance of OLED devices prepared as such (ITO/HATCN/NPB/TCTA/Ir(bpiq)2acac 5wt%:TCTA/CuI 6wt%:CzBPDCb or CzBPCb/TPBi/Liq/Al), a maximum EQE of 17.5% was noted for devices with **Cu39**, while those prepared with **Cu40** reached 3.24% (Table 2).

Zhai and co-workers prepared three new copper(I) complexes **Cu41–Cu43** bearing *N*-substituted-carbazol-3-yl)-4,5-diazafluorene derivative as ligand associated with POP having a general formula of [Cu(POP)(N^N)][PF_6] (N^N = 9,9-bis(9-ethylcarbazol-3-yl)-4,5-diazafluorene for **Cu41**, 9,9-bis(9-ethylhexylcarbazol-3-yl)-4,5-diazafluorene for **Cu42**, 9,9-bis(9-phenylcarbazol-3-yl)-4,5-diazafluorene for **Cu43**) (Scheme 1).[120] Complexes **Cu41–Cu43** showed a TADF emission mechanism with a fitted ΔE_{ST} of 0.09 eV, as well as a fitted τ_{TADF} of 5.7 µs (Table 1). These complexes feature good thermal stabilities with T_d values of 382, 375, and 384 °C for **Cu41**, **Cu42**, and **Cu43**, respectively. Additionally, these complexes feature high glass transition temperatures (T_g) of 123 and 185 °C for **Cu42** and **Cu43**, while **Cu41** does not exhibit a T_g but a melting point (T_m) of 249 °C. Corresponding OLED devices were prepared by vacuum deposition with the following structure: ITO/PEDOT:PSS/TCTA/complex 10 wt%:mCP/TmPyPb/LiF/Al. All the devices exhibited a yellowish-green electroluminescence emission centered at around λ_{max} = 544 nm, x/y CIE color coordinates: 0.37/0.55 and L_{max} of 1100 cd m^{-2} and EQE of 14.8% for the device with **Cu41** (Table 2). The good PL and EL efficiencies were justified by the authors indicating: i) the bulkiness of the ligand substituents weakens the lattice energies and electrostatic interactions which render the complexes easily sublimable, and ii) a good carrier balance related to the hole-transporting properties of the carbazole and the electron-transporting properties of the diazafluorene which improves the OLEDs efficiency.

The copper(I) dinuclear complexes **Cu44–Cu46** prepared in 2017 have a central tetraimine ligand, a 3,5-dipyridyl-1,2,4-triazole derivative, coordinating two {Cu(POP)}$^+$ fragments by two nitrogen atoms on each metal center. The three complexes differ on the substituents introduced in the tetraimine (pytzph = 6,6′-(1-phenyl-1,2,4-triazole-3,5-diyl)bis(2-methylpyridine) **Cu44**, pytzphcf = 6,6′-(1-(4-(trifluoromethyl)phenyl)-1,2,4-triazole-3,5-diyl)bis(2-methylpyridine) **Cu45**, and pytzphcz = 9-(4-(3,5-bis(6-methylpyridin-2-yl)-1,2,4-triazol-1-yl)phenyl)-carbazole **Cu46**.[121] At RT, the photoluminescence of these complexes consists of a green emission centered at around 503–519 nm with dominant TADF contribution (89–97%) and a remaining phosphorescence contribution (3–11%). Additionally, **Cu46** with the highest PLQY of 79% exhibits the highest TADF contribution of 97%, while **Cu45** with the lowest PLQY of 29% exhibited the highest phosphorescence contribution of 11% (Table 1 and **Scheme 8**). Of note, these complexes are thermally stable until 325 °C. Solution-processed OLEDs with the architecture ITO/PEDOT:PSS/**Cu44–Cu46** 20wt%:PYD2/3TPYMB/LiF/Al displayed similar green emissions (λ_{max} = 522–526 nm) with L_{max} of more than 2000 cd m^{-2}. Complex **Cu46** with the

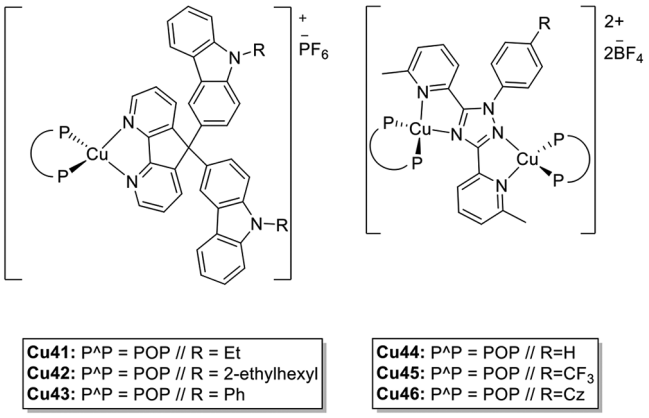

Scheme 8. Description of copper(I) complexes **Cu41–46**.

aforementioned highest PLQY displayed the best performances in devices, reaching the highest brightness peak (2525 cd m^{-2}) and the highest EQE (8.3%) at 7.3 V (Table 2). The authors attributed these results to the good hole-transporting properties of the carbazole moiety.

Interestingly, Sauvage, Nierengarten, Armaroli, and co-workers synthesized heteroleptic copper(I) pseudorotaxanes based on macrocyclic phenanthroline and biphosphines ligands,[122–125] By comparison with more conventional acyclic phenanthroline ligands, the authors demonstrated that the macrocyclic ligand brings more chemical stability to the copper(I) complexes, as decoordination of ligands is unfavored as the diphosphosphine copper(I) framework is surrounded by the macrocycle.[122–124] Encouraged by these preliminary results, the first applications in OLEDs were reported in 2018.[125] The three complexes **Cu47–Cu49** of general formula [Cu(N^N)(POP)][BF_4] (N^N is a macrocyclic ligand incorporating 2,9-phenanthroline moiety and is depicted in **Scheme 9**) were synthesized. For comparative motives, the authors included [Cu(dmp)(POP)][BF_4] **Cu50** that is one of the widely studied copper(I) complexes (Table 1 and Scheme 9).[126–128] Contrary to other copper(I) complexes,[109] these copper rotaxane complexes exhibited rather good stability at RT in solution. Overall, the electrochemical study proved that increasing the size of the macrocycle improved the stability by preventing the flattening of the Cu(I) complexes during the oxidation process. The photoluminescence analysis at different temperatures revealed the existence of TADF for all compounds. Additionally, a strong relationship between the excited states and the pseudorotaxanes structure was evidenced. Indeed, longer triplet lifetimes were found in the small macrocycle **Cu47**, while **Cu49** with the largest macrocycle showed the longest singlet lifetime. The complex **Cu49**, which showed excellent electrochemical stabilities was selected as the reference **Cu50** for OLED devices (ITO/PEDOT:PSS/complex 15wt%:BCPO/TPBi/LiF/Al) (**Figure 7** and Table 2). Both devices provided a similar bright green electroluminescence (x/y CIE color coordinates: 0.32/0.55 for **Cu49** and 0.33/0.55 for **Cu55**). However, devices with **Cu49** reached much higher L_{max} of 12 800 cd m^{-2} and EQE 10.5% than devices with **Cu50**—that is, 7740 cd m^{-2} and 9.5%.

The copper(I) complexes **Cu51** and **Cu52** based on carbene-metal-amide (CMA) structure with TADF were introduced into

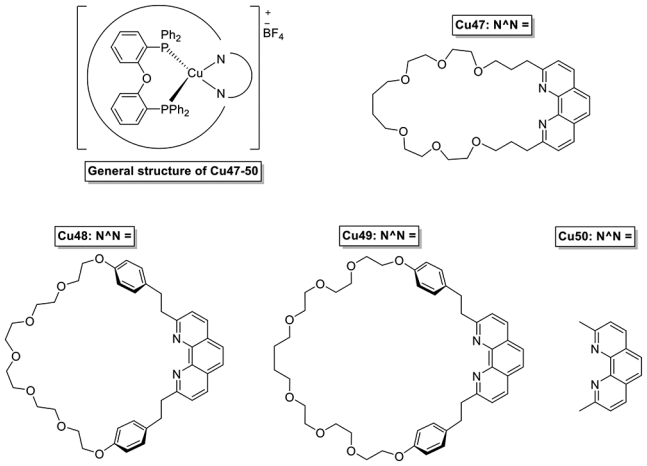

Scheme 9. Description of copper(I) complexes **Cu47–50**.

OLEDs by Bochmann, Credgington, and co-workers (Table 1 and **Scheme 10**).[129,130] Calculations carried out using TD-DFT showed a low ΔE_{ST} below 0.15 eV, confirming the TADF mechanism. Complex **Cu52** exhibited a weak charge transfer nature that leads to poor photoluminescence features.[130] Their thermal gravimetric analysis (TGA) in powder showed high stabilities, that is, T_d above 340 °C for **Cu51** and 360 °C for the sterically hindered **Cu52**. Subsequently, **Cu51** achieved a maximum EQE of 9.7% in solution-processed OLEDs (ITO/PEDOT:PSS/poly(9,9-dioctylfluorene-co-N-(4-butylphenyl)diphenylamine) (TFB)/**Cu51**/20wt%:PVK/bathophenanthroline (BPhen)/LiF/Al) (Table 2).

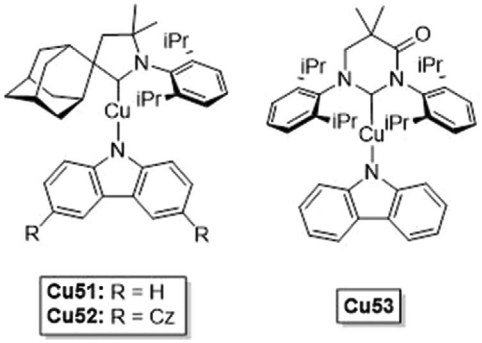

Scheme 10. Description of copper(I) complexes **Cu51–53**.

Thompson reported in 2019 a series of two-coordinate CMA copper(I) complexes based on NHC ligands.[131,132] The complexes exhibited TADF emission and covered the visible spectrum from violet (432 nm) to deep red (704 nm) with high PLQYs up to 100% (Table 1 and Scheme 10). The k_r values were ranging between 10^5 and 10^6 s^{-1}, which are comparable to those of iridium(III) and platinum(II) complexes.[13] As shown in **Figure 8**, a thorough temperature-dependent analysis was conducted for complex **Cu53**. The analysis of τ revealed a steady monoexponential increase upon decreasing the temperature from 320 to 130 K and then, featured a biexponential behavior between 120 and 5 K. The compound was found to have a small ΔE_{ST} of 500 cm^{-1} (62 meV) and a large zero-field splitting (ZFS) or $\Delta E(^{III}T_1\text{-}^{II}T_1/^{I}T_1)$ of 85 ± 20 cm^{-1}. The τ values are 70 ns; 1.4, 44, and 190 µs for τ_{S1}, τ_{TADF}, $\tau^{III}T_1$, and $\tau\ ^{II}T_1/^{I}T_1$, respectively. The vapor-deposited OLEDs were designed using **Cu53** either

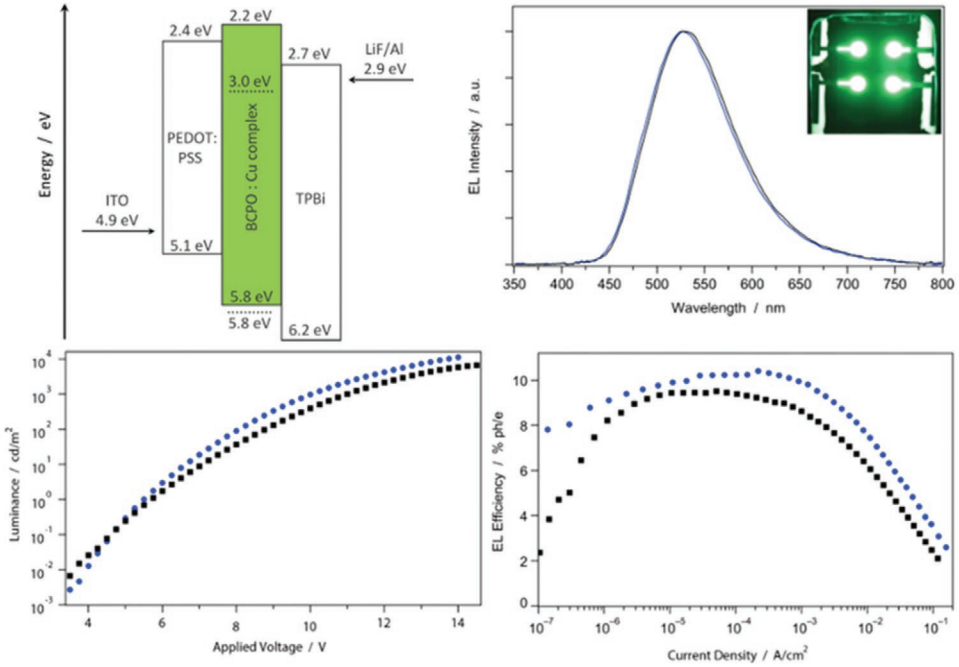

Figure 7. Architecture and properties of OLEDs based on **Cu49** (blue) and **Cu50** (black). Reproduced with permission.[125] Copyright 2018, American Chemical Society.

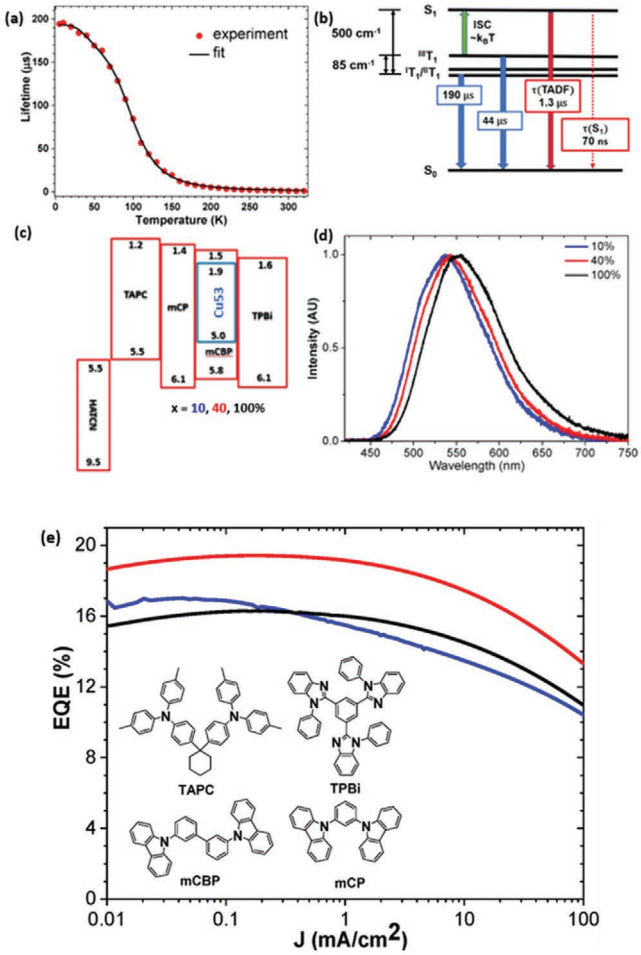

Figure 8. a,b) TD-emission decay times of compound **Cu53** and corresponding fitted data according to Equation (1). c–e) Architecture and EL properties of the OLED devices using compound **Cu53** in 10 wt% (blue), 40 wt% (red), and 100 wt% (black). Reproduced with permission.[131] Copyright 2019, American Chemical Society.

as a dopant at 10 and 40 vol% into the guest mCPB or as neat (Figure 8). All devices reached over 16% of EQE with the device with 40% of the dopant displaying the highest EQE of 19.4% with an L_{max} of 54 000 cd m^{-2} (Table 2).

A family of copper(I) complexes based on 2-(3-phenyl-1*H*-1,2,4-triazol-5-yl)pyridine (pptz) was prepared by Xu and co-workers.[133] At RT, the $[Cu(PPh_3)_2(pptz)][BF_4]$ **Cu54** (**Scheme 11**) exhibited a blue emission centered at 490 nm with 89.9% of PLQY, while [Cu(POP)(pptz)][BF_4] **Cu55** (Scheme 11) showed a green emission at 512 nm with a moderate PLQY of 27.8% (Table 1). At 77 K, the emission maxima of both complexes were red-shifted up to 508 and 520 nm for **Cu54** and **Cu55**, respectively. The τ became much longer from 23.6 to 269.0 µs for **Cu54** and from 13.0 to 210.1 µs for **Cu55** (Table 1). Contrary to the photoluminescence performances, devices with **Cu55** outperformed those with **Cu54** using the device configuration ITO/PEDOT:PSS/complex 20wt%:TCTA/TPBi/LiF/Al. Indeed, devices prepared with **Cu55** exhibited a lower V_{on} of 6 V, a higher L_{max} of 1871 cd m^{-2}, and efficiency of 2.1 cd A^{-1} compared to the device fabricated with **Cu54** with V_{on}, L_{max}, and

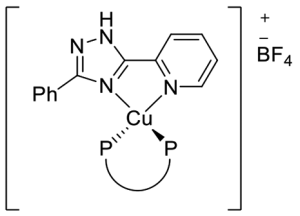

Cu54: P^P = POP
Cu55: P^P = $(PPh_3)_2$

Scheme 11. Description of copper(I) complexes **Cu54** and **55**.

efficiency of 6.5 V, 1437 cd m^{-2}, and 1 cd A^{-1}, respectively. The authors assigned the enhanced performance to the better conjugated molecular structure and a smaller ΔE_{ST} of 0.04 eV compared to that of **Cu52** (0.09 eV) (Table 2).

Zhang and co-workers investigated the photo- and electroluminescence characteristics of the binuclear copper(I) complexes prepared by co-deposition using aza-9,9′-spirobifluorene (aza-SBF) as ligand and CuX salts (X = Cl, Br, and I giving **Cu56**, **Cu57**, and **Cu58**, respectively) (Table 1 and **Scheme 12**).[134] In thin films, the complexes exhibited yellow emissions with λ_{max} centered at 553 nm for **Cu56**, 537 nm for **Cu57**, and 526 nm for **Cu58**; τ ranged between 25.7 and 31.6 ns for PF and around 5.3 µs for DF τ values. These findings were attributed to a TADF mechanism.[119,121,135,136] The authors used different doping concentrations of CuX and found that molar ratios of 7% for CuCl and CuBr and 9% for CuI led to enhanced PLQY and EQE values. Co-deposited copper(I) complexes during OLED elaboration often suffer from lack of stability.[135] Thus, the thermal and moisture stability of the co-deposited thin films showed decomposition upon heat treatment and also were moisture sensitive. The electroluminescence of the complexes in solution-processed OLEDs are red-shifted compared to the photoluminescence (≈20 nm); the devices achieved maxima EQE values of 9.1%, 13.6%, and 10.7% for **Cu56**, **Cu57**, and **Cu58**, respectively. Meanwhile, a blue-shift of 4 nm was detected upon voltage increase and attributed to an irreversible electric field-induced exciton dissociation of the complexes (Table 2). These findings compiled with the thin films' thermal and air degradations suggested that an irreversible dissociation takes place during operation.

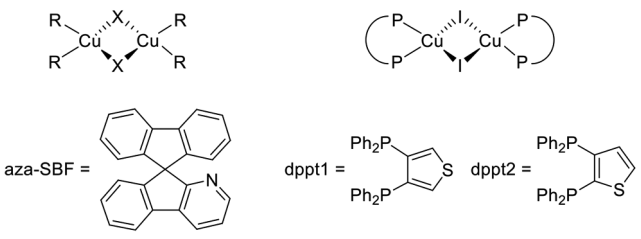

Cu56: R = aza-SBF // X = Cl
Cu57: R = aza-SBF // X = Br
Cu58: R = aza-SBF // X = I

Cu59: P^P = dppt1
Cu60: P^P = dppt2

Scheme 12. Description of copper(I) complexes **Cu56–60**.

Lu and co-workers prepared two new binuclear copper(I) complexes, in which the $\{Cu_2I_2\}$ core was chelated with two thiophene-based diphosphine ligands: 3,4-bis(diphenylphosphino) thiophene (dppt1) **Cu59** and 2,3-bis(diphenylphosphino)thiophene (dppt2) **Cu60** (Table 1 and Scheme 12).[137] Compared to **Cu15** and **Cu36–38**, which are based on dppbz derivatives, these new complexes bearing a thiophene ring instead of the benzene ring in the dppbz ligand feature blue-shifted emissions. Moreover, the position of the sulfur atom in the thiophene was found to have a strong influence on both photo- and electro-luminescent properties of the complexes. The importance of the electronic properties of the thiophene was confirmed by DFT calculations, which revealed that, while the HOMO is dispersed across the metal core, the LUMO is solely located at the sulfur heterocycle. The theoretical study also showed that **Cu60** exhibited a smaller HOMO–LUMO energy gap than **Cu59**. Additionally, **Cu60** featured a ΔE_{ST} of 362 cm^{-1} versus 586 cm^{-1} for **C59**. Consequently, **Cu60** exhibited a 96% TADF blue emission (λ_{max} = 483 nm) with a PLQY of 86%, and τ_{obs} of 7.62 µs, while **Cu59** showed a 84% of TADF blue emission (λ_{max} = 487 nm) with a PLQY of 69% and τ_{obs} of 9.46 µs (Table 1). All complexes featured very good thermal stability with T_d over 400 °C. Vapor-processed OLEDs (ITO/MoO_3/MoO_3 20wt%:mCP/mCP/complex 9wt%:mCP/DPEPO/TPBi/LiF/Al) based on **Cu59** and **Cu60** showed green emissions at 515 and 540 nm, respectively. In line with the photoluminescence features, devices with **Cu60** exhibited higher EQE (14.5%) and L_{max} (3665 cd m^{-2}), while **Cu59** reached 7.44% and 1380 cd m^{-2} for EQE and $L_{max,}$ respectively (Table 2).

Green and Yellow-Emitting LECs: Gaillard and Costa groups reported a green-emitting NHC-Cu(I)-based complex **Cu61** featuring a green emission at RT with λ_{max} of 521 nm and PLQY of 20% (powder) with τ_{obs} of 7 µs (Table 1 and **Scheme 13**).[102] Upon freezing at 77 K, a red-shifted emission up to 150 cm^{-1} was detected. The ΔE_{ST} of 0.35 eV was calculated using TD-DFT. Complex **Cu61** was used in LECs with the configuration ITO/PEDOT:PSS/**Cu61**/Al, showing a L_{max} of 2.7 cd m^{-2} and an electroluminescence spectrum red-shifted to λ_{max} of 555 nm (Table 3). In addition, the authors noticed a further 9 nm red-shift over repetitive IVL, probably due to the same issue during the oxidation process observed for complex **Cu8**.[109] Furthermore, studying the role of the bridging group on dipyridyl ligand in [Cu(NHC)(N^N)][PF_6] complexes,[103] the authors reported that replacing the NH framework of the 2,2′-dipyridylamine ligand by PPh group, **Cu11** exhibits green emission with λ_{max} centered at 503 nm and PLQY of 86%. Performances of LEC devices

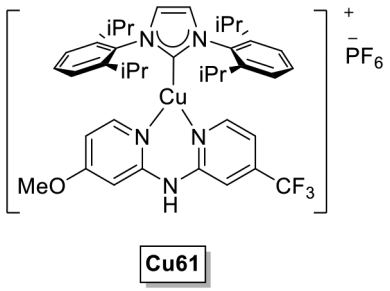

Cu61

Scheme 13. Description of copper(I) complex **Cu61.**

prepared with complex **Cu11** were studied at different currents (5 and 0.5 mA) and the latter reached the best values of L_{max} of 32 cd m^{-2} at 5 mA and an *Eff* of 0.39 cd A^{-1} at 0.5 mA (Table 3).

Housecroft, Orti, Constable, and co-workers prepared LECs containing TADF emitting [Cu(P^P)(N^N)][PF_6] complexes **Cu62–64** (**Scheme 14**). In 2018, the authors presented the effects of trifluoromethyl group (CF_3) substitution in positions 6, 5, and 4 on the bipyridine (bpy) ligand of [Cu(P^P)(bpy)][PF_6] complexes.[138] Electrochemistry study revealed that the introduction of the CF_3 pushes the Cu^+/Cu^{2+} oxidation to higher potential values (+0.85 to +0.96 V), while theoretical studies showed that the HOMO–LUMO gap is influenced by the electronic richness of the N^N ligand. Indeed, adding an electron-withdrawing group (EWG) stabilizes both the HOMO and the LUMO while an electron-donating group (EDG) has the opposite effect. In solution, compounds showed a broad absorption band between 350 and 480 nm assigned to the MLCT, with a very weak emission ranged from 606 to 705 nm. In powder at 298 K, all compounds exhibited an emission in the range of 517–664 nm and with τ between 2.9–12 µs. From all compounds, [Cu(xantphos)((6,6′-Me_2-4,4′-$CF_3)_2$bpy)][PF_6] **Cu64** showed the highest PLQY of 50.3% at λ_{max} of 517 nm and the longest emission τ_{obv} of 12 µs. As in frozen Me-THF, the λ_{max} of **Cu64** was red-shifted to 604 nm and showed longer excited-state lifetimes up to 88 µs; the participation of a TADF process was suggested and then confirmed by TD-DFT calculations, as ΔE_{ST} was found at 0.11 eV (Table 2). Compounds [Cu(POP)(6-CF_3bpy)][PF_6] **Cu62**, [Cu(xantphos)(6-CF_3bpy)][PF_6] **Cu63**, and [Cu(xantphos)((6,6′-Me_2)(4,4′-$CF_3)_2$bpy)][PF_6] **Cu64** were incorporated in LECs (Table 3). To improve the performances of the devices by decreasing the turn-on time (t_{on}),[139,140] the authors added an ionic liquid (IL), 1-ethyl-3-methylimidazolium hexafluorophosphate [EMIM][PF_6], to the active layer in a 4/1 molar ratio of Cu(I)/IL. All devices showed a yellow emission with device **Cu64**, displaying the fastest t_{on} of 8 min and the highest L_{max} of 131 cd m^{-2} with EQE of 0.6%. Complex **Cu 63** exhibited the longest lifetime $t_{1/2}$ of 31 h with an L_{max} of 109 cd m^{-2} and an EQE of 0.5% (Table 3).

After proving that [Cu(POP)(bpy)][PF_6] and [Cu(xantphos)(bpy)][PF_6] complexes with CF_3 group in the bpy ligand exhibit TADF emissions,[138] the substitution with halides in position 3,3′ namely chlorine: [Cu(POP)(6,6′-Cl_2bpy)][PF_6] **Cu65** and [Cu(xantphos)(6,6′-Cl_2bpy)][PF_6] **Cu66** and bromine: [Cu(POP)(6-Brbpy)][PF_6] **Cu67**, [Cu(xantphos)(6-Brbpy)][PF_6] **Cu68**, [Cu(POP)(6,6′-Br_2bpy)][PF_6] **Cu69**, and [Cu(xantphos)(6,6′-Br_2bpy)][PF_6] **Cu70** were also investigated (Scheme 14).[141] The complexes exhibit yellow emissions in powder from 544 nm (**Cu70**) to 584 nm (**Cu65**) with moderate PLQY values 3.9–17.1%. The ΔE_{ST} was estimated in a range 0.15 eV (**Cu65**) to 0.19 eV (**Cu70**), which is small enough to allow TADF mechanism and confirmed upon freezing the samples at 77 K, as the decay lifetimes increased considerably from 2.3–4.8 µs at RT to 112–119 µs at 77 K (Table 1),[14,47,138] although **Cu65–70** showed two emission maxima in solution, which could explain the coexistence of both TADF and phosphorescence.[71,142,143] LECs based on **Cu65–70** with the following architecture ITO/PEDOT:PSS/complex:[EMIM][PF_6] (1:4)/Al were developed (Table 3). Devices with complexes **Cu67–Cu70** having bromine substitutions did not display any electroluminescence. The authors stated that this

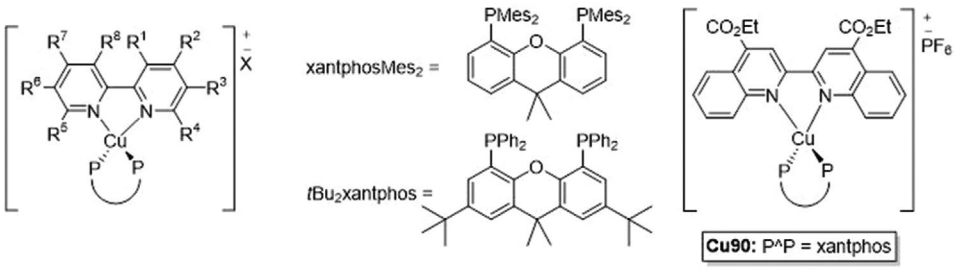

R = H unless specified	**Cu75:** P^P = POP // R^4 = SEt
X = PF_6 unless specified	**Cu76:** P^P = POP // R^4 = SPh
Cu62: P^P = POP // R^4 = CF_3	**Cu77:** P^P = xantphos // R^4 = OMe
Cu63: P^P = xantphos // R^4 = CF_3	**Cu78:** P^P = xantphos // R^4 = OEt
Cu64: P^P = xantphos // R^2 = R^7 = CF_3, R^4 = R^5 = Me	**Cu79:** P^P = xantphos // R^4 = OPh
Cu65: P^P = POP // R^4 = R^5 = Cl	**Cu80:** P^P = xantphos // R^4 = SMe
Cu66: P^P = xantphos // R^4 = R^5 = Cl	**Cu81:** P^P = xantphos // R^4 = SEt
Cu67: P^P = POP // R^4 = Br	**Cu82:** P^P = xantphos // R^4 = SPh
Cu68: P^P = xantphos // R^4 = Br	**Cu83:** P^P = tBu$_2$xantphos
Cu69: P^P = POP // R^4 = R^5 = Br	**Cu84:** P^P = tBu$_2$xantphos // R^4 = Me
Cu70: P^P = xantphos // R^4 = R^5 = Br	**Cu85:** P^P = tBu$_2$xantphos // R^4 = R^5 = Me
Cu71: P^P = POP // R^4 = OMe	**Cu86:** P^P = xantphosMes$_2$
Cu72: P^P = POP // R^4 = OEt	**Cu87:** P^P = xantphosMes$_2$ // R^4 = Me
Cu73: P^P = POP // R^4 = OPh	**Cu88:** P^P = POP // R^4 = R^5 = OMe
Cu74: P^P = POP // R^4 = SMe	**Cu89:** P^P = xantphos // R^2 = R^7 = OMe, X = BF_4

Scheme 14. Description of copper(I) complexes **Cu62–90**.

type of behavior had already been reported in other copper(I)[143] and iridium(III)[144] complexes. Devices based on **Cu65** and **Cu66** with chlorine substitutions displayed both quite similar yellow electroluminescence with peaks at λ_{max} of 586 and 587 nm, respectively. Overall, devices based on **Cu66** with xantphos led to the best performances with an L_{max} of 259 cd m^{-2}, an EQE of 1.2% corresponding to at least 50% higher performances than the device based on **Cu65** with POP (L_{max}, EQE, CE, and PE of 121 cd m^{-2}, 0.6%, 1.2 cd A^{-1}, and 0.3 lm W^{-1}, respectively). Nevertheless, the latter exhibits longer stabilities and fast turn-on times (Table 3).

The same authors also studied the influence of alkoxy, alkylthio, phenyloxy, and phenylthiol groups on the bpy moiety in [Cu(P^P)(bpy)][PF_6]:[145] i) P^P is POP and N^N: 6-MeObpy (**Cu71**), 6-EthObpy (**Cu72**), 6-PhObpy (**Cu73**), 6-MeSbpy (**Cu74**), 6-EthSbpy (**Cu75**), and 6-PhSbpy (**Cu76**); ii) P^P is xantphos and N^N is: 6-MeObpy (**Cu77**), 6-EthObpy (**Cu78**), 6-PhObpy (**Cu79**), 6-MeSbpy (**Cu80**), 6-EthSbpy (**Cu81**), and 6-PhSbpy (**Cu82**) (Table 1 and Scheme 14). The electrochemical studies suggested that substitutions in 6-position stabilized the tetrahedral geometry of the complexes, which results in high oxidation values in the range of +0.75 to +0.86 V. These values are higher than those of the unsubstituted parent complexes [Cu(POP)(bpy)][PF_6] (+0.72 V) and [Cu(xantphos)(bpy)][PF_6] (+0.76 V).[138]

In terms of photophysical properties, **Cu67–Cu78** exhibited photoluminescence at λ_{max} between 549 and 585 nm. The PLQY analysis showed higher values for the xantphos complexes series compared to POP complexes, attributed to the higher rigidity of the xantphos ligand. The thioether substituent led to higher PLQYs for these copper(I) complexes than ether substituent, and these values tend to increase with the size of the hydro carbonated group.

At 298 K, the τ were measured at 1 to 10 µs magnitude in powder, while in frozen Me-THF at 77 K, these values were at least four times higher. Then, red-shift of the emission by a 14 to 34 nm was also observed, suggesting again the presence of the TADF process. Studying the complexes **Cu71–Cu82** using TD-DFT, ΔE_{ST} were calculated in the range of 0.21 and 0.25 eV, allowing participation of TADF emission mechanism. All the compounds were incorporated in LECs using the same configuration previously reported (ITO/PEDOT:PSS/complex:[EMIM][PF_6] (4:1)/Al) (Table 3).[138,141] The devices were pulsed at a 50 A m^{-2} current average, 50% duty cycle, 1 kHz. Following the same trend observed for the PLQY, devices with xantphos-type complexes were more efficient as their efficiencies were measured in a range between 0.8 and 1.6 cd A^{-1}, compared to 0.2–1.3 cd A^{-1} for the POP series.

Importantly, devices prepared with complexes having RObpy as ligands (**Cu71–73**) have longer device lifetime than the ones fabricated with complexes having RSbpy substituent (**Cu74–76**) when the POP series is considered. Nevertheless, this trend is reversed when the xantphos series (**Cu77–82**) is taken into account. Overall, the bulkier the substituents, the higher the L_{max} and the better the efficiencies, which is in agreement with the electrochemical analysis, pointing out that an increased hindrance leads to a stabilization of the geometry.

As the next step, the authors studied the structural and electronic effects of bulkier groups in the xantphos ligand: 2,7-bis(*tert*-butyl)-4,5-bis(diphenylphosphino)-9,9-dimethylxanthene (tBu$_2$xantphos) and chiral 4,5-bis(mesityl-phenylphosphino)-9,9-dimethylxanthene (xantphosMes$_2$).[146] As N^N ligands, 6-methyl-2,2′-bipyridine (6-Mebpy) and 6,6′-dimethyl-2,2′-bipyridine (6,6′-Me$_2$bpy) were selected.[146] In comparison to their xantphos homologues, tBu$_2$xantphos complexes **Cu83–Cu85** (Table 1 and Scheme 14) showed blue-shifted emissions: λ_{max} = 522 nm for **Cu85** versus λ_{max} = 539 nm for the same complex with

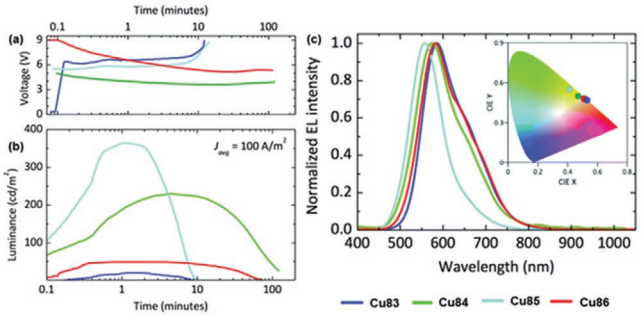

Figure 9. Figures of merit of copper(I) complexes **Cu83-86**. a) Voltage and b) luminance versus time at an average current density of 100 A m^{-2}. c) Electroluminescence spectra for the same device series with (inset) the corresponding CIE 1931 color coordinates. Reproduced with permission.[146] Copyright 2019, Royal Society of Chemistry.

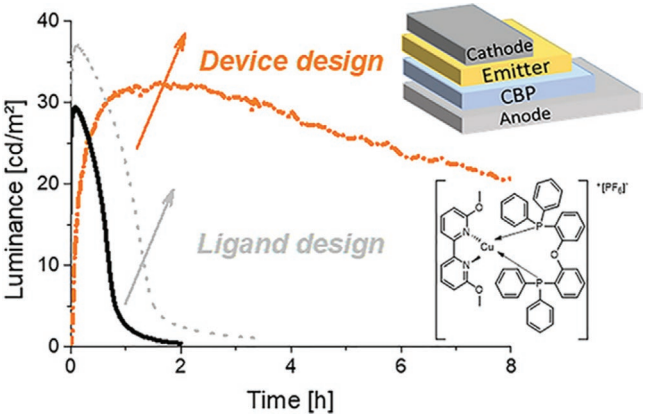

Figure 10. Figures of merit of LECs designed with **Cu88**. Reproduced with permission.[147] Copyright 2018, American Chemical Society.

xantphos,[138] whereas xantphosMes$_2$ complexes **Cu86–Cu87** exhibited less altered emissions: λ_{max} of 589 and 547 nm, respectively, versus λ_{max} of 587 and 547 nm for the corresponding xantphos complexes.[138] TADF mechanism was again confirmed in all complexes with a ΔE_{ST} in the range of 0.17–0.25 eV. The corresponding LECs (ITO/PEDOT:PSS/complex:[EMIM][PF_6] (4:1)/Al) (Table 3) showed all electroluminescence except for complex **Cu86** with the lowest PLQY in powder (1.9%). The electroluminescence and the PLQY followed the same trend. In detail, *t*Bu$_2$xantphos-based devices showed better properties than xantphosMes$_2$ analogues. Devices with **Cu85** were the best performing with the highest *Eff* and L_{max} of 3.7 cd A^{-1} and 370 cd m^{-2}, respectively (**Figure 9**).

Another contribution to this TADF copper(I) complex family of [Cu(bpy)(P^P)]$^+$ was carried out by Costa and co-workers in 2018.[147] The authors reported the influence of ortho-substitution of the methoxy group to the bipyridine ligand; complex **Cu88** with N^N = 6,6-dimethoxy-2,2-bipyridine and POP ligands with yellow emissions centered at 575 nm with PLQY of 20% and τ_{obs} of 1.22 and 0.13 µs (Table 1 and Scheme 14). Noteworthy, the authors mentioned that **Cu88** exhibited better thermo- and photostability, as well as photoluminescence and ionic conductivity, compared to those of the unsubstituted [Cu(bpy)(POP)]$^+$ complex.[138,147,148] These enhancements were also observed in LECs built in a bilayer architecture: ITO/PEDOT:PSS/4,4′-bis(carbazol-9-yl)biphenyl (CBP)/**Cu88**/Al when driven at 7.5 mA. The device showed yellow emission with λ_{max} = 573 nm, x/y CIE color coordinates: 0.46/0.52 at a low V_{on} of 3.4 V and t_{on} of 1.6 h. This device reached an L_{max} of 32.9 cd m^{-2}, efficacies of 0.3 cd A^{-1}, and $t_{1/2}$ of 10.8 h (Table 2 and **Figure 10**).

In 2019, Cano et al. released a comparative detailed study between copper(I) complex [Cu(4,4′-dimethoxy-2,2′-bipy)(xantphos)] (**Cu89**) (Table 1 and Scheme 14), and silver(I) complex [Ag(4,4′-dimethoxy-2,2′-bipy)(xantphos)] (**Ag6**) (**Table 4** and **Scheme 15**).[149] Complex **Cu89** features sky-blue emissions centered at 493 nm with PLQY of 57.1% in powder, whereas its silver(I) homologue **Ag6** shows more red-shifted emissions at 545 nm and lower PLQY of 18.9%. Theoretical calculations suggested that TADF is less notable in **Cu89** than in **Ag6**. The authors provided valuable guidelines regarding the emission mechanism and how to enhance the PL and EL of d^{10} complexes emitters for LEC applications (see **Section 2.1.2**).

Figure 11 gathers all green and yellow-emitting OLED devices using their CIE color coordinates as reported by the authors. The best preforming devices are also given. However, LEC devices are not represented as the authors did not report the CIE color coordinates.

Orange and Red-Emitting OLEDs: As mentioned in the section dedicated to green-emitting devices, Che and co-workers prepared three TADF copper(I) complexes based on neocuproine and dppnc emitting in green (**Cu31**), yellow (**Cu32**), and red (**Cu33**), (Table 1 and Scheme 6).[114] At RT, **Cu33** showed red emission centered at λ_{max} = 657 nm with a PLQY of 4.2% in powder and a τ_{obs} of 2.1 µs, while the emission is blue-shifted to λ_{max} = 624 nm with a dramatic increase of τ_{obs} to 495.6 µs at 77 K. Theoretical calculations carried out at the TD-PBE0/LanL2DZ;6-31G(d) theoretical level rendered a

Table 4. Photophysical properties of Ag(I) complexes with TADF.

Complex[a)]	λ_{max} [nm][b)]	PLQY [%]	τ_{PF} [ns]/τ_P [µs]/τ_{TADF} [µs]	ΔE_{ST} [eV]	HOMO/LUMO [eV]	CIE [x/y]	Ref.
Ag1	505[c)]/530[d)]	32[c,g)]/72[d,f)]	–/547/2.22,0.56	0.02[h)]	–	–	[105]
Ag2	470[c)]/472[d)]	100[c,g)]	–/11/0.5	0.02[h)]	–	–	[132]
Ag3	512[f)]/500[d)]	79[c,g)]	–/7.7/0.33	0.02[h)]	–	–	[132]
Ag4	496[c)]/443,479,510[e)]	19[c,g)]	–/10.8/0.38	0.08	–5.51/–2.86	–	[162]
Ag5	514[c)]/457,486,516[e)]	45[c,g)]	–/20.3/0.42	0.08	–5.29/–2.83	–	[162]
Ag6	545[c)]	18.9[c,f)]	–	–	–	–	[149]

[a)]Selected photophysical data in solid-state for Ag(I) complexes with TADF used in OLEDs discussed in this review; [b)]Maximum emission wavelength; [c)]Measured at 298 K; [d)]Measured at 77 K; [e)]Measured at 50 K. PLQY values in [f)]powder; [g)]film. Values converted from the ones reported by the authors in [h)]cm^{-1}.

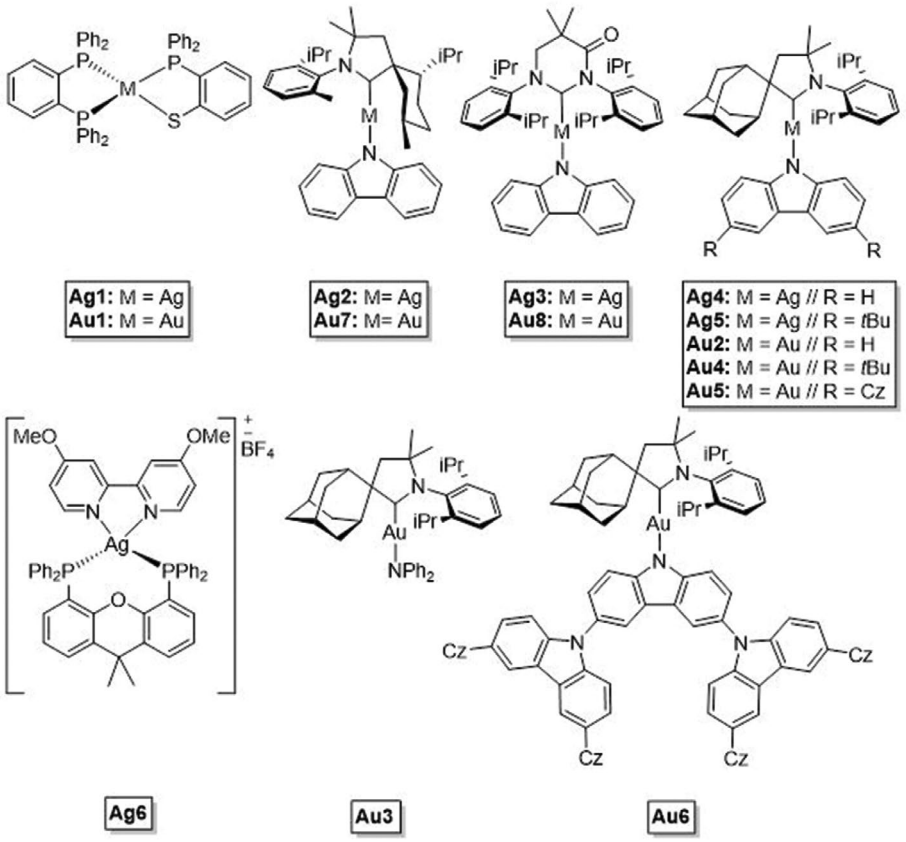

Scheme 15. Description of Ag(I) complexes **Ag1–6** and Au(I) complexes **Au1–8**.

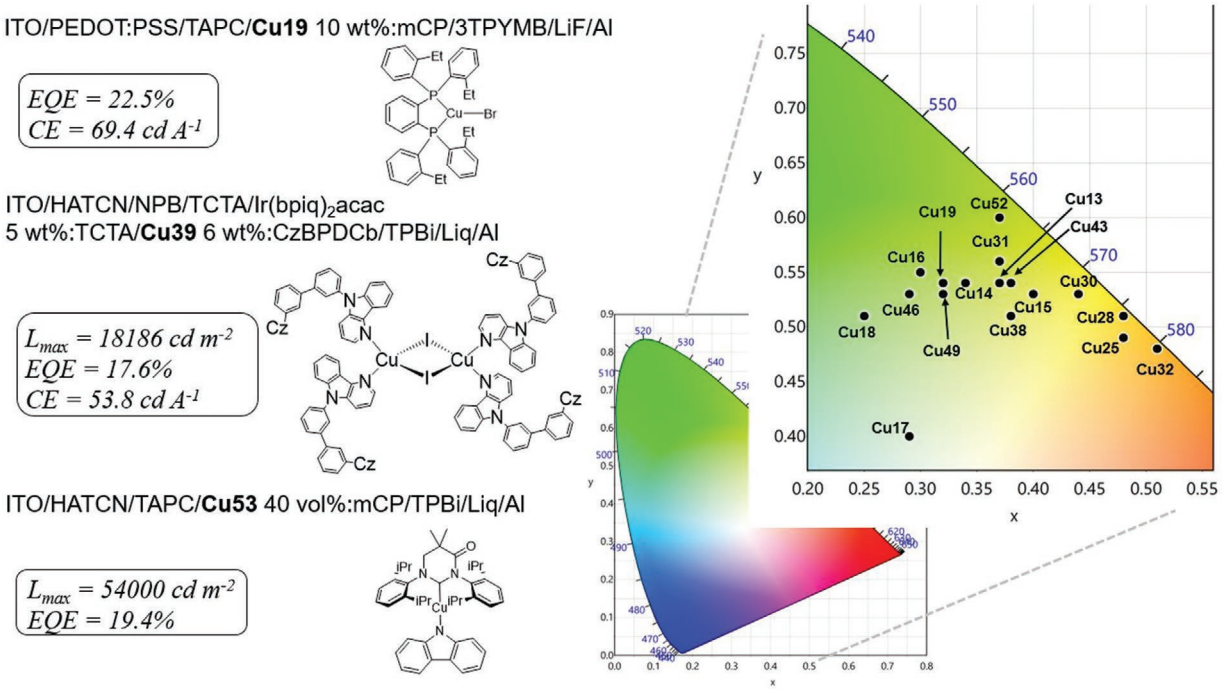

Figure 11. Graphical summary of the benchmark copper(I)-based green and yellow-emitting OLEDs devices, devices with highest efficiencies are represented on the left. LEC devices are not given as the authors did not report CIE color coordinates.

ΔE_{ST} value of 2073 cm^{-1}. The authors had previously reported that the ΔE_{ST} predicted with the aforementioned model is often 1.5- to 2.5-fold higher than the experimental values,[113] therefore, assuming a correction factor of 1.5; the experimental values of ΔE_{ST} were estimated to be 1382 cm^{-1}, suggesting that **Cu33** was, indeed, a TADF emitter. The photoluminescence was also investigated in thin films using different host materials (PMMA, PVK, and PYD2) and **Cu33** in 10 wt%. The films prepared showed emissions of λ_{max} = 665 nm and PLQY of 4.6% for PMMA, λ_{max} = 664 nm and PLQY of 3.8% for PVK, and λ_{max} = 639 nm and PLQY of 21.7% for PYD2. This high PLQY encouraged the use of PYD2 as host to prepare solution-processed OLEDs using **Cu33** as guest in 4, 8, 12, and 20 wt%. The detailed configuration was: ITO/PEDOT:PSS/**Cu33** 4–20wt%:PYD2/DPEPO/TPBi/LiF/Al. In addition to the electroluminescence from **Cu33**, these devices showed an emission from PYD2, suggesting an inefficient overlap between the host and the dopant. To circumvent this issue, the PYD2 was replaced by CBP as host. As well, DPEPO was removed to keep only TPBi. The new device, using CBP as a host and 4 wt% of **Cu33**, was a record-breaking red-emitting copper-based OLED with λ_{max} = 631 nm, x/y CIE color coordinates: 0.61/0.38, and maximum EQE of 10.2% (Table 2).

Orange and Red-Emitting LECs: The only example of deep-red emitting LECs based on Cu(I) TADF complexes was reported by Costa et al. in 2019.[150] In this study, three complexes with the general formula [Cu(N^N)(P^P)](PF_6) (N^N = 4,4′-diethylester-2,2′-biquinoline (dcbq)) were reported, and among the diphosphines tested, complex **Cu90** with P^P = xantphos (Scheme 14) was selected for device preparation due to its superior stability, deep-red emission in the solid-state, λ_{max} = 671 nm, and the highest PLQY value of the series (56%) (Table 1). The device made with **Cu90** showed a promising electroluminescent response, that is, stable deep-red emission centered at around 675 nm, x/y CIE color coordinates: 0.66/0.32 (Table 2), with an irradiance of ≈100 μW cm^{-2}, and stabilities of almost a day. The authors also reported white-emitting LECs using **Cu90** (see section White-Emitting LECs).

White-Emitting OLEDs: White-emitting OLEDs were successfully achieved by Che and co-workers using the yellow emitting complex **Cu28** (Table 1 and Scheme 6) and blue-emitting dopant (**Figure 12**): i) iridium(III) complex bis[(4,6-difluorophenyl)pyridinato-N,C2]-(picolinato)iridium (FIrpic),[151] and ii) $Zn_4O(AID)_6$ (AID = 7-azaindolate).[113] First, a solution-processed Cu/Ir OLED (ITO/PEDOT:PSS/FIrpic 10wt%: **Cu28** 1wt%: PYD2/DPEPO/TPBi/LiF/Al) was investigated. This device reached a high EQE of 16.8% with x/y CIE color coordinates: 0.37/0.48 and a color rendering index (CRI) of 61. Changing the host and hole-blocking layer (HBL) from PYD2 to poly(N-vinylcarbazole):((1,3-bis((4-tert-butylphenyl)-1,3,4-oxadiazolyl)phenylene)) (PVK:OXD-7) and DPEPO to 3TPYMB proved to be beneficial for the CRI as the new white-emitting device showed higher CRI of 71 and x/y CIE color coordinates: 0.37/0.45.

Next, the authors used this PVK:OXD-7/3TPYMB configuration to make the Cu/Zn OLED (Figure 12). This device reached the highest EQE of 6.88%, CRI of 80, L_{max} of 22 cd m^{-2}, and x/y CIE color coordinates of 0.44/0.44 at 7 V. The highest CRI

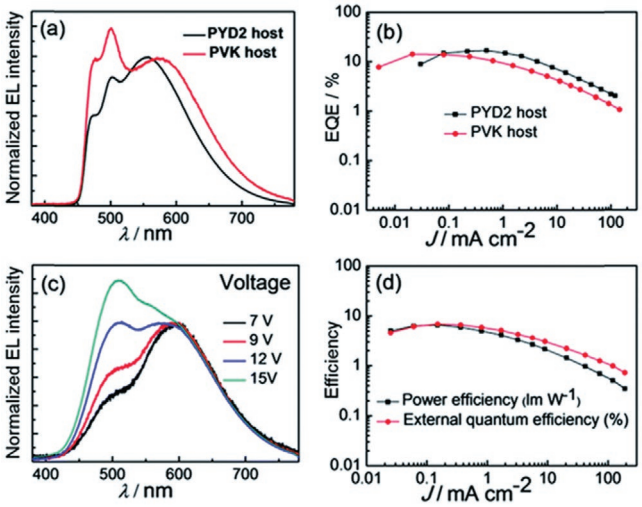

Figure 12. a) Normalized EL spectra and b) EQE–power efficiency–current density characteristics of the white OLED with 10 wt% FIrpic and 1 wt% **Cu28** using PYD2/DPEPO or PVK/3TPYMB device structure. c) EL spectra at different driving voltages and d) EQE–power efficiency–current density characteristics of the white OLED with 10 wt% $Zn_4O(AID)_6$ and 1 wt% **Cu28**. Reproduced with permission.[113] Copyright 2019, Royal Society of Chemistry.

of 81 was reached upon increasing the voltage at 9 V, while the highest luminance of 3150 cd m^{-2} was reached at 15 V with x/y CIE color coordinates: 0.35/0.44.

White-Emitting LECs: As mentioned in the red-emitting LECs section, Costa and co-workers also reported the first proof-of-concept for white-emitting LECs.[150] The device was prepared by mixing **Cu90** with the HTM CBP in a host–guest approach. The LEC (85:15 wt% for CBP:**Cu90**) featured x/y CIE color coordinates of 0.31/0.32 and a high CRI of 92.

As mentioned before, copper(I) complexes are the most representative TADF transition metal complexes emitters. This large reported library is mainly due to the d^{10} electronic configuration avoiding the non-emissive MC transition. Then, if the comparison is made from data reported in the literature, some structural/photophysical relationships can be noticed.

As first example, complexes coordinated to electron-rich pyrazole derivatives **Cu1–Cu5**, **Cu21**, and **Cu22** (Schemes 1 and 4) feature high energetic emissions (blue-green region) with very high PLQY. The introduction of functional moieties on these ligands, such as DMAC and carbazole, appears to enhance both the photoluminescence and electroluminescence of the resulting copper(I) complexes as the ΔE_{ST} is reduced, giving efficient TADF emitters. Using triazole ligands (**Cu–54** and **Cu55**, Scheme 11) is also beneficial for the TADF efficiency (ΔE_{ST} = 0.09 and 0.04 eV^{-1}), but the emissions are red-shifted.

Copper(I) complexes based on rigid dppbz derivatives and pyrazole ligand derivatives containing a bridging boron atom feature green TADF emissions (**Cu12–Cu14**). Of note, functionalization of the dppbz ancillary with fluorine substituents increase the PLQY and the thermal stabilities of the compounds, leading to OLEDs with higher performances than those including complexes coordinated to unsubstituted dppbz.

If neutral halogen–diphosphine complexes **Cu16–Cu20** (Scheme 3) bearing various dppbz ligands are compared to the halogen–triphosphine complexes **Cu23–Cu25** (Scheme 5), emission mechanism becomes dual, and the presence of halogen ligand having high SOC enhances the phosphorescent mechanism. As a consequence, complex **Cu25** features a dual phosphorescence and TADF emission at RT with 39% and 71% contributions, respectively.

In the series of complexes bearing NHC ligands **Cu6–Cu11** and **Cu61** (Schemes 2 and 13), variation on the TADF mechanism was not noticed, but an increase of the PLQY can be achieved in function of the σ-donation of the NHC, whereas color tuning can be obtained by varying the central atom or the electronic nature of the substituent in the bis-pyridyl ligand.

When phenanthroline and bipyridine derivatives are coordinated to the copper metal center copper(I) complexes **Cu26–33** (Scheme 6) and **Cu47–50** (Scheme 9), functionalization of the ligands in the ortho position of the coordinating nitrogen atom leads to stable complexes as geometrical distortions are balanced by both the Jahn–Teller effect and the steric hindrance. This also affects the TADF efficiency by minimizing the ΔE_{ST}. On the other hand, the maximum emission wavelength is controlled by functionalization at the para position of the nitrogen atoms. The use of rigid phosphane ligands has been widely investigated; sterically bulky carborane ligands **Cu26–Cu33** with unique electronic effects and thermal stability improve the photoluminescence and physical properties of the complexes, while the use of functionalized xantphos derivative tBu$_2$xantphos **Cu84** and **Cu85** (Scheme 14) leads to high efficiency in LECs.

Binuclear copper(I) complexes feature strong stability compared to mononuclear ones; this is due to the fact that in these complexes, the HOMO is localized on both copper atoms, and the complexes having Cu_2X_2 core show emission governed by a MLCT/ligand-to-ligand charge transfer (LLCT) mixture. The presence of heavy halogens—for example, iodine—with a strong SOC effect, increases the phosphorescence participation in the emission for these complexes. The stability of these copper(I) complexes has led to industry level processability of OLEDs such as inkjet printing in the case of complex **Cu35** (Scheme 7) or co-deposition of CuX salt and corresponding ligands to in situ form complexes **Cu39**, **Cu40** (Scheme 7), and **Cu56–58** (Scheme 12).

2.1.2. Silver(I) Complexes

Silver(I) complexes exhibiting TADF have recently emerged. However, compared to copper(I) complexes, they are still scarce, mostly because silver(I) complexes have a stronger SOC effect compared to copper(I) complexes and, consequently, often exhibit phosphorescence rather than TADF.[8,87,149] Silver(I) complexes suffer, however, from an inherent sensitivity to light[152] and limited solubilities.[12,105,152] The 4d orbitals of silver(I) complexes are energetically lower than ligand-centered orbitals and, in turn, the nature of the emitting excited state shows a dominant LLCT character, while copper(I) complexes are dominated by the MLCT character.[8,12,87] Thus, silver(I) complexes with TADF exhibit higher stabilities upon oxidation and higher energy emissions. Besides, the PLQY is usually very high, up to 100%. Additionally, their τ and ΔE_{ST} are often smaller.[105,107,132,152–157] In contrast to the above mentioned, silver(I) complexes have scarcely been applied to lighting devices.[158–161]

OLEDs: TADF in silver(I) complexes was first discussed by Osawa and co-workers in 2013.[105] **Ag1 (**Table 4 and Scheme 15) showed TADF emission centered at 505 nm arising from LLCT transition with a PLQY of 32%. Unfortunately, its incorporation into OLEDs was unsuccessful due to its low solubility. Thompson's group has recently reported silver(I) complexes **Ag2** and **Ag3** with TADF emissions (ΔE_{ST} = 150 and 180 cm^{-1}) with high PLQY up to 100% for **Ag2** (Table 4 and Scheme 15), but the authors failed to prepare OLEDs based on these complexes due to their lack of sublimability.[132]

Bochmann and co-workers successively prepared OLEDs based on TADF-emitting Ag(I) complexes **Ag4** and **Ag5** (Table 4 and Scheme 15).[162] The complexes are based on the strong sigma donor character of NHC(Ad) carbene and carbazole ligands in a linear donor-Ag-acceptor geometry. Unlike other silver(I) complexes, these compounds are not sensitive to light,[152] and are stable in non-protic solvents. The nature of the emitting excited state was determined using DFT, featuring a LLCT transition originated from the carbazole unit with only a 5% of contribution of the Ag metal core to the LUMO entirely located at the carbene ligand. In thin films, **Ag4** and **Ag5** exhibit TADF emissions centered at 496 and 514 nm with respective lifetimes of 380 and 420 ns at RT. **Ag5** featured the highest PLQY of 45%. At 50 K, the emission becomes phosphorescence but this appears blue-shifted and exhibits three peaks at 443, 479, and 510 nm for **Ag4** and 457, 486, and 516 nm for **Ag5**. The ΔE_{ST} was estimated at 0.08 eV for both complexes. Of note, the TGA analysis shows T_d of 264.8 and 263.6 °C for **Ag4** and **Ag5**, respectively. Vapor and solution-processed OLEDs were developed (**Table 5** and **Figure 13**). These devices reach the highest EQE of 4.3% and 13.7% for vapor-processed, while solution-processed devices achieve 3.8% and 11% for **Ag4** and **Ag5**, respectively. The latter exhibited a red-shifted EL spectra with higher V_{on} and increased roll-off compared to vapor-processed devices.

LECs: In their recent work, Cano et al. provided an in-depth comparison on both **Cu89** and **Ag6**, two d^{10} complex emitters based on a bipy derivative and xantphos ligand (Schemes 14 and 15).[149] With both photoluminescence and theoretical studies, the authors concluded despite the fact that **Cu89** and **Ag6** feature similar molecular and electronic nature in both ground and excited states; the phosphorescence is more favored in **Cu89** than **Ag6**. However, TADF was found to be induced in both cases by ferromagnetic couplings taking place between the metal and the bipy in the excited states. Noteworthy, **Cu89** exhibited emission-quenching Cu-O bonds in the excited states, which are not found in **Ag6**, suggesting that replacing oxygen in the xantphos by a non-coordinating atom should be beneficial. The electroluminescence properties of **Ag6** were investigated in LEC devices.[163] Despite a L_{max} of 40 cd m^{-2} and *Eff* of 0.2 cd A^{-1} under 6.5 V, the device showed low stabilities with a $t_{1/2}$ 0.008 h. Changing the counterion from BF_4^- to PF_6^- led to higher L_{max} of 131 cd m^{-2}, *Eff*

Table 5. Figures of merit of OLED devices based on Ag(I) complexes with TADF.

Complex[a)]	Device architecture	V_{on} [V]	λ_{max} [nm]	L_{max} [cd m^{-2}]	EQE [%]	CE [cd A^{-1}]	PE [lm W^{-1}]	CIE [x/y]	Ref.
Ag4	ITO/PEDOT:PSS/TAPC/**Ag4** 20wt%:mCP/UGH2:TPBi/TPBi/LiF/Al	4.3	502	–	4.3	–	–	0.26/0.42	[162]
Ag5	ITO/PEDOT:PSS/TAPC/**Ag5** 20wt%:mCP/UGH2:TPBi/TPBi/LiF/Al	4.3	509	21000	13.7	–	–	0.28/0.46	[162]

[a)]Reported data were selected from the corresponding references, in favor of the highest EQE or highest CE when EQE was not given. V_{on}, turn-on voltage; λ_{max}, maximum emission; L_{max}, maximum luminance; EQE, maximum external quantum efficiency; CE, maximum current efficiency; PE, maximum external power efficiency; CIE, Commission Internationale de l'Eclairage.

of 0.6 cd A^{-1}, but at cost of the device stability (0.003 h). The quick degradation of the devices was confirmed to be originated from the irreversible reduction of Ag(I) into Ag(0) upon electron injection forming Ag(0) nanoclusters. Decoupling electron injection and exciton formation by using 2-(4-*tert*-butylphenyl)-5-(4-biphenylyl)-1,3,4-oxadiazole (PBD), an electron transporting material with reversible oxido-reduction processes led to the optimization of the device by hampering the direct reductions of the Ag(I). This approach led to a broad whitish emission (x/y CIE color coordinates: 0.40/0.44 and CRI of 85) with L_{max} of 35 cd m^{-2}, and most importantly, the stability was improved up to 80 h.

2.1.3. Gold(I) Complexes

Gold has always been a very prolific element for the preparation of emissive complexes. However, the number of gold complexes with TADF emission is still scarce. Like silver(I) complexes, gold(I)-based complexes have a strong SOC that facilitates the ISC, the forbidden spin-triplet states then allow phosphorescent emissions arising from MC and MLCT transitions.[12,156,158,164] Contrary to silver(I), emissions in gold(I) complexes are usually red-shifted due to strong Au–Au interactions; however, these interactions tend to quench the luminescence or to activate cluster centered charge transfer (CCCT) transitions without TADF component.[12,165]

In 2013, Osawa and co-workers reported the first gold(I) complex **Au1** with TADF (**Table 6** and Scheme 15).[105] At RT, **Au1** features emissions centered at 610 nm with a PLQY of 12% and a two-component decay of 1.66 and 0.47 µs. At 77 K, the emissions are red-shifted to 630 nm, and the decay

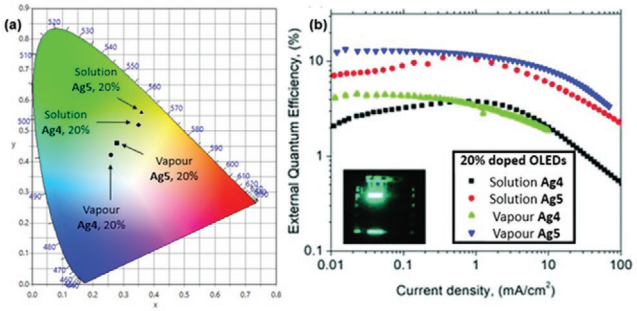

Figure 13. a) CIE color coordinates of vapor-processed and solution-processed OLEDs based on complexes **Ag4** and **Ag5**. b) EQE versus current density of the same OLEDs. Reproduced with permission.[162] Copyright 2018, Wiley-VCH.

increases considerably up to 52 µs. The $S_1 - T_1$ energy gap was calculated to be 405 cm^{-1} and the origin of the emission was assigned to LLCT instead of MLCT, since it is weakened by the electron-donating character of the thiolate ligand. However, unlike its copper(I) homologue **Cu15**, the complex **Au1** could not be used in either solution or vacuum-processed OLED due to its instability in solutions and its low vapor pressure. Likewise, there are other examples of gold(I) complexes with TADF, but with no application in SSL. An excellent summary of the state-of-the-art for TADF in gold has been recently published during the preparation of this review.[88]

A particular family of carbene-metal-amide (CMA) gold(I) complexes with TADF emissions was implemented in OLEDs with excellent results.[129,130,132,166–168] These complexes are soluble and stable in a range of organic solvents and present good thermal stabilities, rendering them well-suited for both solution and vapor-processed OLEDs. The molecular configuration of these molecules allows a rapid RISC from a near-zero ΔE_{ST}, leading to good PL and EL efficiencies. Additionally, the EL is optimized by the presence of carbazole moieties from their good hole-transporting properties. Credgington, Bochmann, and co-workers reported the first OLEDs based on gold(I)-CMA complexes with TADF emissions.[129] **Au2–Au4** feature sub-microsecond lifetime TADF emissions due to a rapid RISC (Table 6 and Scheme 15). A temperature-dependent PL analysis of **Au2** shows that the emission is 99% delayed fluorescence at RT with 350 ns, while below 100 K, the emission is assigned to phosphorescence with lifetimes around 10 µs. Corresponding solution-processed OLEDs (**Figure 14**) achieved outstanding performances up to EQE of 27.5% for **Au4**. In comparison to its copper(I) homologue **Cu51**, devices with **Au2** outperformed it. Indeed, **Au2** displays a low V_{on} of 2.6 V and high L_{max} of 44 700 cd m^{-2} and EQE values of 26.3% (**Table 7**). These performances were improved a year later, as the authors developed vacuum-processed OLED based **Au2** displaying up to 27% of EQE (Table 7).[167] Noteworthy, the authors reported a host-free TADF OLED with EQE higher than 23% breaking the record previously held by Adachi and co-workers.[169]

In a follow-up work, the authors presented dendritic complexes based on a CMA core (Table 6 and Scheme 15).[130] Just like **Au2–Au4**,[129] **Au5** and **Au6** exhibit an emission that is accounted for over 90% of TADF at RT with short $\tau < 1$ µs. The gold series showed better CT between the donor (carbazole) and the acceptor (carbene) compared to their copper homologue **Cu52**. Suitable solution-processed OLEDs were fabricated; all devices displayed over 10 000 cd m^{-2} of luminance

Table 6. Photophysical properties of Au(I) and Au(III) complexes with TADF.

Complex[a]	λ_{max} [nm][b]	Φ_{PL} [%]	τ_{PF} [ns]/τ_P [µs]/τ_{TADF} [µs]	ΔE_{ST} [eV]	HOMO/LUMO [eV]	CIE [x/y]	Ref.
Au1	610[c]/630[d]	12[c,e]/18[d,e]	–/52/1.66, 0.47	0.05[g]	–	–	[105]
Au2	540[c]/510[d]	–	–/≈10/0.35	–	–5.60/–2.80	–	[129,167]
Au5	510[c]/524[d]	68[c,f]	–/–/1.97	0.11	–5.67/–2.62	–	[130]
Au6	508[c]/513[d]	47.5[c,f]	–/–/1.06	0.15	–5.68/–2.68	–	[130]
Au7	472[c]/472[d]	100[c,f]	25/45/1.14	0.07[g]	–5.17/–5.01	–	[132]
Au8	512[c]/506[d]	85[c,f]	24/43/0.83	0.07[g]	–5.12/–1.87	–	[132]
Au9	523[c]	66[c,f]	–/–/1.35	–	–4.60/–2.48	–	[186]
Au10	564[c]	42[c,f]	–/–/0.74	0.05[g]	–		[186]
Au11	517[c]	84[c,f]	56.9/23.5/0.72	0.04[g]	–4.70/–2.42	–	[186]
Au12	513[c]	78[c,f]	–/–/0.85	–	–	–	[186]
Au13	521[c]	67[c,f]	–/–/1.10	–	–	–	[186]
Au14	577[c]	88[c,f]	–/–/0.85	0.33[g,h]	–	–	[187]
Au15	546[c]	29[c,f]	–/–/3.78	–	–	–	[187]
Au16	560[c]	67[c,f]	–/–/1.43	–	–	–	[187]
Au17	567[c]	65[c,f]	–/–/1.46	–	–	–	[187]
Au18	568[c]	80[c,f]	–/–/1.19	–	–	–	[187]
Au19	595[c]	56[c,f]	–/–/0.77	–	–	–	[187]
Au20	527,570,640[c]	9[c,f]	–/–/0.33	–	–	–	[187]

[a]Selected photophysical data in solid-state for Au(I) and Au(III) complexes with TADF used in OLEDs; [b]Maximum emission wavelength; [c]Measured at 298 K; [d]Measured at 77 K. PLQY values in [e]powder; [f]film. Values converted from the ones reported by the authors in [g]cm^{-1}; [h]Depending on the relative orientation of the D-A fragments.

with **Au5** achieving 29 000 cd m^{-2} and the highest maximum EQE of 10.6%.

In 2019, Thompson released a detailed study on CMA d^{10} coinage metal complexes.[132] Gold(I) complexes **Au7**-**Au8** with high PLQY between 80% and 100% were included (Table 6 and Scheme 15). At RT, all complexes feature TADF emissions with small τ between 0.33 and 2.8 µs, which is governed by ΔE_{ST} ranging between 150–590 cm^{-1}. Thorough temperature-dependent photophysical analysis revealed τ of 20–85 ns for fluorescence and 50–200 µs for phosphorescence, respectively. Complex **Au8** was used to prepare OLEDs. They feature green emissions and reach high EQE up to 18% and almost 10 000 cd m^{-2} of brightness (Table 7). CIE color coordinates of Ag(I)- and Au(I)-based devices were collected and are represented in **Figure 15**, as the best performing devices in each category.

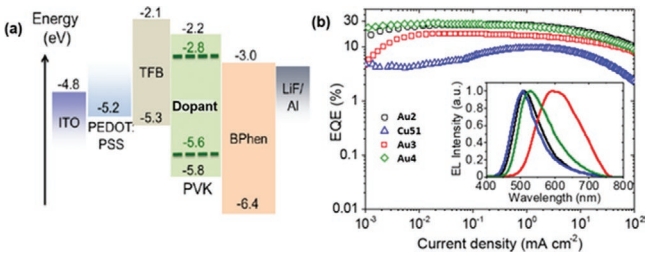

Figure 14. a) Energy level diagram of solution-processed OLEDs based on **Au2–Au4** and **Cu51**. b) EQE versus current density of the same OLEDs devices with the inset showing their EL spectra. Reproduced with permission.[129] Copyright 2017, Science (AAAS).

2.1.4. Tin(IV) Complexes

Tin(IV) complexes have also been used as emitters in OLEDs,[4,170–172] after the pioneering work of Adachi in 2009.[4] Here, six Tin(IV) complexes **Sn1**–**Sn6** were described (**Table 8** and **Scheme 16**). Their steady-state emissions feature strong TADF emissions (569–579 nm) and weak phosphorescence around 700 nm at RT. The photoluminescence analysis at different temperatures on **Sn1** revealed PF, TADF, and phosphorescence processes. Beyond 250 K, the photoluminescence is ruled by the TADF process. This indicates that the k_{RISC} is temperature-dependent, and in turn, TADF is allowed due to a small ΔE_{ST} estimated at 0.24 eV. An OLED device based on **Sn1** was prepared, the device showed poor performances as it required up to 10 V for current injections and 29 V to reach a current density of 100 mA cm^{-2} (**Table 9**). The device exhibits a temperature depending electroluminescence, featuring both prompt and delayed fluorescence; the latter is composed of TADF and phosphorescence. Based on these findings, Adachi and co-workers provided crucial guidelines on designing efficient TADF emitters, such as the molecule rigidity, the use of heavy atoms or halogens, and most importantly a small ΔE_{ST}.

2.1.5. Tungsten(VI) Complexes

Two years after reporting OLEDs with 4.79% of EQE using air-stable phosphorescent tungsten(VI) complexes,[173] Cheng and co-workers reported for the first time TADF in tungsten(VI)

Table 7. Figures of merit of OLED devices based on Au(I) and Au(III) complexes with TADF.

Complex[a)]	Device architecture	V_{on} [V]	λ_{max} [nm]	L_{max} [cd m^{-2}]	EQE [%]	CE [cd A^{-1}]	PE [lm W^{-1}]	CIE [x/y]	Ref.
Au2	ITO/PEDOT:PSS/TFB/**Au2** 20wt%:PVK/BPhen/LiF/Al	2.6	–	44700	26.3	76.3	62.7	0.24/0.42	[129,167]
Au3	ITO/PEDOT:PSS/TFB/**Au3** 20wt%:PVK/BPhen/LiF/Al	3.0	–	39540	17.9	45.2	33.6	0.24/0.42	[129]
Au4	ITO/PEDOT:PSS/TFB/**Au4** 20wt%:PVK/BPhen/LiF/Al	2.6	–	73100	27.5	87.1	75.1	0.24/0.42	[129]
Au5	ITO/PEDOT:PSS/TAPC/**Au5** 20wt%:TCP/BPhen/LiF/Al	3.2	–	29000	10.6	–	–	0.39/0.58	[130]
Au6	ITO/PEDOT:PSS/TFP/**Au6** 20wt%:PVK/BPhen/LiF/Al	3.6	–	10000	3.7	–	–	0.37/0.60	[130]
Au8	ITO/TAPC/mCP/**Au8** 40wt%:mCBP/TPBi/LiF/Al	2.6	516	92401	18.0	–	–	–	[132]
Au10	ITO/PEDOT:PSS/**Au10** 16wt%:PVK:OXD-7/TPBi/LiF/Al	–	509	57340	14.8	44.9	23.6	0.32/0.55	[186]
Au12	ITO/PEDOT:PSS/**Au12** 16wt%:PVK:OXD-7/TPBi/LiF/Al	–	500	33740	23.8	70.4	47.3	0.27/0.51	[186]
Au14	ITO/HATCN/TAPC/TCTA/**Au14** 8wt%:TCTA:TPBi/ /TPBi/TmPyPb/LiF/Al	–	–	37500	23.1	76.0	99.4	0.35/0.56	[187]
Au17	ITO/HATCN(5 nm)/TAPC/ TCTA/**Au17** 4wt%:TCTA:TPBi/ TPBi/TmPyPb/LiF/Al	–	–	26300	19.7	57.5	86.9	0.41/0.55	[187]
Au18	ITO/HATCN(5 nm)/TAPC/ TCTA/**Au18** 4wt%:TCTA:TPBi/ TPBi/TmPyPb/LiF/Al	–	–	70300	23.4	70.6	82.8	0.40/0.55	[187]

[a)]Reported data were selected from the corresponding references, in favor of the highest EQE or highest CE when EQE was not given V_{on}, turn-on voltage; λ_{max}, maximum emission; L_{max}, maximum luminance; EQE, maximum external quantum efficiency; CE, maximum current efficiency; PE, maximum external power efficiency; CIE, Commission Internationale de l'Eclairage.

complexes in OLEDs (Table 9 and **Scheme 17**).[174] The new complex **W1** chelated to a Schiff base exhibits high PLQY up to 84% in steady-state and a ΔE_{ST} 1000 cm^{-1} small enough to allow TADF which was proved by emission red-shift and excited states lifetimes at low temperature (Table 8). Importantly, TGA analysis shows very good thermal stabilities with T_d values of 363 °C. Solution-processed OLEDs based on **W1** reached outstanding EQE of 15.6% and L_{max} of 16 890 cd m^{-2} (Table 9). These performances which are not far from the best reported in TADF Cu, Ag, and Au,[115,129,162] show that W is a promising

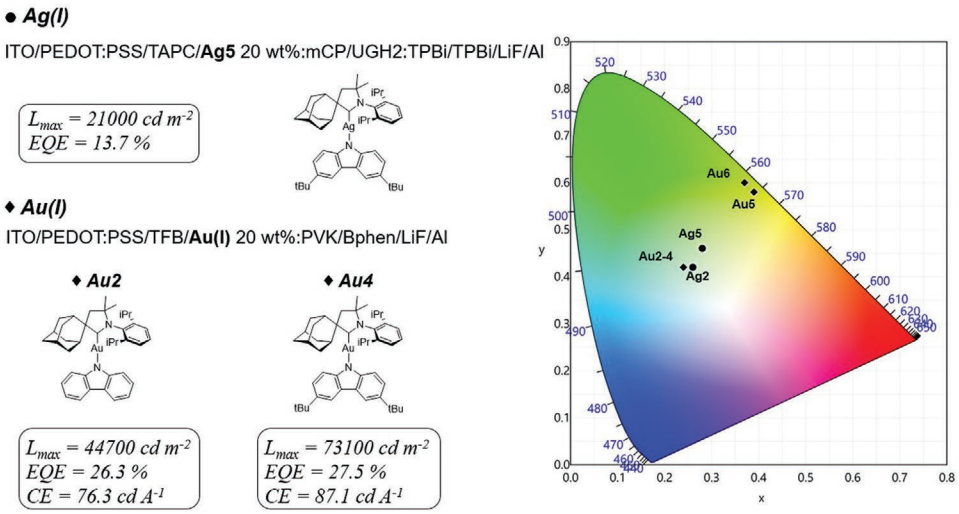

Figure 15. Graphical summary of the benchmark OLEDs devices based on Ag(I) and Au(I) complexes; devices with highest efficiencies are represented on the left.

Table 8. Photophysical properties of Pd(II), Sn(IV), W(VI) and Zn(II) complexes with TADF.

Complex[a)]	λ_{max} [nm][b)]	Φ_{PL} [%]	τ_{PF} [ns]/τ_{P} [µs]/τ_{TADF} [µs]	ΔE_{ST} [eV]	HOMO/LUMO [eV]	CIE [x/y]	Ref.
Pd1	534[c)]/522[d)]	72[c,e)]	142	0.26	–	–	[28]
Pd2	518[d)]	76[c,e)]	205	–	–	–	[28]
Sn1	571[c)]/701 [d)]	–	–	0.40[g)]	–	–	[4]
Sn2	569[c)]/701[d)]	–	–	0.41[g)]	–	–	[4]
Sn3	576[c)]/698[d)]	–	–	0.38[g)]	–	–	[4]
Sn4	579[c)]/708[d)]	–	–	0.39[g)]	–	–	[4]
Sn5	570[c)]/703[d)]	–	–	0.40[g)]	–	–	[4]
Sn6	571[c)]/701[d)]	–	–	0.40[g)]	–	–	[4]
W1	555[c)]/563[d)]	84[c,e)]	–/358/2	0.12[f)]	–	–	[174]
Zn1	542[c)]	78.4[c,e)]	12.8/–/37.8	0.06	–	–	[29]
Zn2	523[c)]	58.2[c,e)]	–	0.18	–	–	[29]

[a)]Selected photophysical data in solid-state for Pd(II), Sn(IV), W(VI) and Zn(II) complexes with TADF used in OLEDs; [b)]Maximum emission wavelength; [c)]Measured at 298 K; [d)]Measured at 77 K; [e)]PLQY value in film. Values converted from the ones reported by the authors in [f)]cm^{-1}; [g)]kJ mol^{-1}.

competitor to other earth-abundant TADF metals in lighting applications.

2.1.6. Zinc(II) Complexes

Zinc(II) compounds are used in OLEDs as in various applications, such as emitters, host materials, and hole injection layers.[86,175] A number of OLEDs including WOLEDs using Zinc(II) complexes as emitters have been reported by different groups[29,176–179]; however, no TADF Zn(II) complex was reported until 2015 when Adachi and co-workers published the first examples in green OLEDs (Table 9 and **Scheme 18**).[29] These new TADF complexes showed very high PLQY of 78.4% and 58.4% with Φ_{TADF} = 66.1% and 48.1% for **Zn1** and **Zn2** respectively (Table 8). All complexes showed an ILCT transition, the authors observed a decrease of ΔE_{ST} and increase of k_{RISC} by metallization to zinc. The devices based on **Zn1** and **Zn2** showed very high EQEs up to 19.6% for **Zn1** and 10.4% for **Zn2**.

Bushuev and his team reported a Zn(II) complex (**Zn3**), exhibiting an interplay between excitation-wavelength-dependent emission and TADF in a proton-transfer system.[180] Although **Zn3** was not used in a lighting device, this was the third zinc(II) complex reported with a TADF emission. **Zn3** showed excitation depending luminescence; in fact, when **Zn3** was excited between 240–420 nm, a maximum emission was detected at 640 nm with a shoulder at 565 nm and the PLQY of 0.02%. Excitation at 420–480 nm increased the 565 nm band with the highest PLQY up to 7.1%. The authors attributed the 565 nm band to PF and TADF, while the 640 nm was attributed to phosphorescence. The authors concluded that incorporating Zn(II) to their molecule facilitates the $S_2 \rightarrow T_2 \rightarrow T_1$ and $S_2 \rightarrow T_1$ intersystem crossing. For Zn(II) photochemistry, the reader can read these articles[91,181–183] and for Zn(II) complexes in OLEDs, the reader is advised to read these reviews.[87,184]

2.2. Complexes with d^8 Electronic Configuration

2.2.1. Gold(III) Complexes

Besides gold(I) complexes, gold(III) complexes with TADF emissions is a growing area with a lot of recent interest. The first example of TADF in gold(III) complexes was reported by Fernandez-Cestau et al. in 2015.[185] Two years later, Che et al. reported

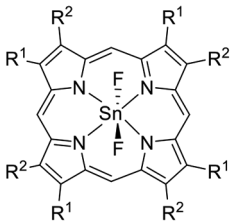

Sn1: $R^1 = R^2$ = Et
Sn2: R^1 = Me, R^2 = Et
Sn6: R^1 = Me, $R^2 = (CH_2)_2$-CO_2Me

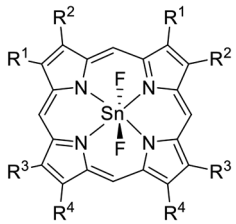

Sn3: R^1 = Me, R^2 = CH(OH)-CH_3, R^3 = Me, $R^4 = (CH_2)_2CO_2H$
Sn4: R^1 = Me, R^2 = vinyl, R^3 = Me, $R^4 = (CH_2)_2CO_2H$
Sn5: R^1 = Me, R^2 = Et, R^3 = Me, $R^4 = (CH_2)_2CO_2H$

Scheme 16. Description of Sn(IV) complexes **Sn1–6**.

Table 9. Figures of merit of OLED devices based on Pd(II), Sn(IV), W(VI), and Zn(II) complexes with TADF.

Complex[a)]	Device architecture	V_{on} [V]	λ_{max} [nm]	L_{max} [cd m^{-2}]	EQE [%]	CE [cd A^{-1}]	PE [lm W^{-1}]	CIE [x/y]	Ref.
Pd1	ITO/HATCN/NPD/TAPC/**Pd1** 6wt%:26mCPy/DPPS/BmPyPB/LiF/Al	–	–	–	20.9	–	–	0.30/0.61	[28]
Pd2	ITO/HATCN/NPD/TAPC/**Pd2** 6wt%:26mCPy/DPPS/BmPyPB/LiF/Al	–	–	–	20.4	–	–	0.30/0.62	[28]
Sn1	ITO (100 nm)/PEDOT:PSS/**Sn1** 2wt%:PVCz/MgAg/Ag	10	–	–	–	–	–	–	[4]
W1	ITO/PEDOT:PSS/**W1** 30wt%:PVK:OXD-7/TPBi/LiF/Al	–	–	16890	15.6	34.0	29.1	0.49/0.49	[174]
Zn1	ITO/α–NPD/**Zn1** 6wt%:mCBP/TPBi/LiF/Al	–	–	–	19.6	–	–	–	[29]
Zn2	ITO/α–NPD/**Zn2** 6wt%:mCBP/TPBi/LiF/Al	–		–	10.4	–	–	–	[29]

[a)]Reported data were selected from the corresponding references, in favor of the highest EQE or highest CE when EQE was not given. V_{on}, turn-on voltage; λ_{max}, maximum emission; L_{max}, maximum luminance; EQE, maximum external quantum efficiency; CE, maximum current efficiency; PE, maximum external power efficiency; CIE, Commission Internationale de l'Eclairage.

the use of TADF Au(III) complex emitters to prepare OLEDs.[186] The authors prepared a family of aryl bis cyclometallated Au(III) complexes [(C^N^C)Au(Ar)] **Au9**–**Au13** with different substituents in the pincer and the aryl ancillary ligand (Table 6 and **Scheme 19**). The study of the photophysical properties of these complexes revealed that the introduction of the *p*-NX_2 {X = Me (**Au10**), Ph (**Au9** and **Au11**), *p*-FC_6H_4 (**Au12**), and *p*-*t*BuC_6H_4 (**Au13**)} substituents in the aryl ancillary ligand activate the TADF mechanism. In particular, in complexes **Au10** and **Au12**, the HOMO is located on the *p*-NX_2 ligand and the LUMO is located on the C^N^C. The authors performed TD-DFT calculations, assuming Boltzmann equilibrium of the S_1 and T_1 excited states, and the average k_r was estimated to be 1.69×10^6 s^{-1}, while the experimental was found to be 7.2×10^5 s^{-1} for **Au10**. For **Au12**, they found a computed k_r of 1.45×10^6 s^{-1} and an experimental value of 1.11×10^6 s^{-1}. The analysis of τ at different temperatures agrees with the calculations leading to the conclusion that complexes **Au9**–**Au13** are TADF emitters.

From this series, **Au9** and **Au11** exhibiting TADF emissions with high PLQY up to 84% were selected to be emissive dopants in solution-processed OLEDs. Different dopant concentrations (4–16 wt%) were employed (Table 7). The authors reported sky-blue to green-emitting OLEDs with a gradual red-shift upon increasing the dopant concentration. The electroluminescence spectrum maxima of the devices with 4 wt% was 509 (**Au9**) and 500 nm (**Au11**). The

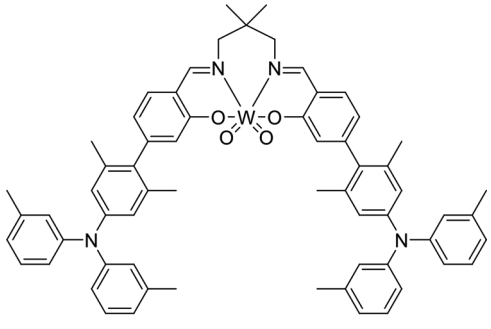

W1

Scheme 17. Description of W(IV) complex **W1**.

emission color of the devices based on **Au9** was sky-blue (x/y CIE color coordinates: 0.27/0.51), whose high EQE of 23.8% was comparable with the best sky-blue OLEDs fabricated by solution process technique. In addition, the emission energy of the devices made with **Au11** could be tuned by using host materials with different band-gaps. For instance, replacing PVK:OXD-7 by PYD2 led to a device emission centered at 486 nm with x/y CIE color coordinates of 0.21/0.42 and a maximum EQE of 15.7% (**Figure 16**).

The same group studied the presence of TADF emissive pathways in bis cyclometallated gold(III) complexes with functionalized acetylide ligands in the ancillary position [(C^N^C)Au(C≡CR)] **Au14**–**Au20** (Table 6 and **Scheme 20**).[187] Since Au(III)-Csp(acetylide) bond is stronger than Au(III)-Csp2(aryl), the former is more stable than the latter. In addition, the photoluminescence is usually more intense since the MC orbitals are higher in energy. The authors performed theoretical calculations and demonstrated that the transition that produces the emission is mainly a HOMO→LUMO, with HOMO located on the triphenylamine motif and the LUMO localized on the C^N^C pincer. The rotation of the alkynyl substituent with respect to the pincer generates a different conformation. Thus, the average k_r of the phosphorescence at the different angles is estimated in the 10^5 s^{-1} and the ΔE_{ST} in the optimized geometry is 18 cm^{-1}. However, the authors also admit the controversy that, at this geometry, the D-A disposition is perpendicular, and the oscillator strength is 0. However, they assign the emission in these systems to TADF. Vacuum-deposited OLEDs based on **Au14**, **Au17**, and **Au18** were fabricated (Table 7 and **Figure 17**). The devices had a structure of ITO/HATCN/TAPC/TCTA/TCTA:TPBi:Au(III) emitter/TPBi/TmPyPb/LiF/Al, in which HATCN (1,4,5,8,9,11-hexaazatriphenylenehexacarbonitrile) was used as a hole-injecting layer, TAPC (di-[4-(*N*,*N*-ditolyl-amino)-phenyl]cyclohexane)as a hole-transporting layer, and TmPyPb (1,3,5-tri(m-pyrid-3-yl-phenyl)benzene) as an electron-transporting layer. The EML was constructed by using the co-host system consisting of TCTA (4,4′,4″-tris(carbazol-9-yl)-triphenylamine) and TPBi with 1:1 weight ratio. The dopant concentrations of **Au14**, **Au17**, or **Au18** were 2, 4, and 8 wt%. Two 10-nm-thick layers of TCTA and TPBi were inserted between EML and charge-transporting

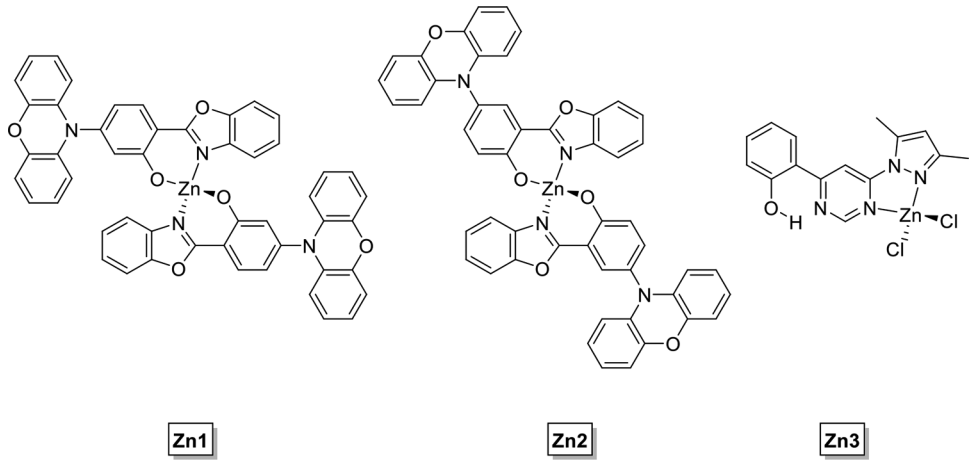

Scheme 18. Description of Zn(II) complexes **Zn1–3**.

layers as exciton-blocking layers. High EQE values of ≈23% were achieved, and in particular, the EQE values of devices fabricated with **Au14** (4 and 8 wt%) and **Au18** (4 and 8 wt%) were slightly higher than those of **Au9** and **Au11** (Table 7).[186]

Thanks to a low V_{on} of 2.4 V, a high power efficiency of 99.4 lm W^{-2} was achieved in the **Au14** device at the dopant concentration of 8 wt%. The authors claimed that the device performance and operational lifetime of OLEDs based on **Au18** were evaluated by Samsung under industry standard conditions. OLEDs with **Au18** (5 wt%) exhibited an EQE of 17% and a small efficiency roll-off of 6% was observed. Its LT95 (an operational lifetime to 95% of initial luminance) at an initial luminance of ≈8000 cd m^{-2} was measured to be approximately 0.3 h. This corresponds to about 10 h at a practical luminance of 1000 cd m^{-2} and about 500 h at a luminance of 100 cd m^{-2}, which is among the best achieved for Au-based OLED devices.

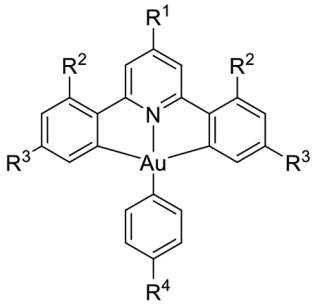

R = H unless specified
Au9: $R^4 = NPh_2$
Au10: $R^4 = NMe_2$
Au11: R^1 = OEt, $R^2 = R^3$ = F, $R^4 = NPh_2$
Au12: R^1 = OEt, $R^2 = R^3$ = F, $R^4 = N(p\text{-}FC_6H_4)_2$
Au13: $R^1 = 2,6\text{-}Me_2\text{-}C_6H_3$, $R^3 = t$Bu, $R^4 = N(p\text{-}t\text{BuC}_6H_4)_2$

Scheme 19. Description of Au(III) complexes **Au9–13**.

2.2.2. Palladium(II) and Pt(II) Complexes

Although palladium(II) and platinum(II) complexes are usually phosphorescent emitters,[12,160,188–197] some of them have also shown TADF behavior.[28,87,193,198–200] In 2015, Li reported vapor-processed OLEDs based on two palladium(II) complexes **Pd1** and **Pd2** (Table 8 and **Scheme 21**), featuring both phosphorescence and TADF emissions.[28] **Pd1** and **Pd2** exhibited temperature-dependent emission bands between 450 and 510 nm that are assigned to $S_1 \rightarrow S_0$ transitions and lower energy phosphorescence emissions arising from $T_1 \rightarrow S_0$ transition. OLEDs prepared using 26mCPy as a host material achieved high EQEs of 20.9% and 20.4% for **Pd1** and **Pd2**, while device based on **Pd1** in CBP reached outstanding operational lifetimes LT_{90} of 170 h with an initial luminance of 1697 cd m^{-2} at a constant current of 20 mA cm^{-2} (Table 9).

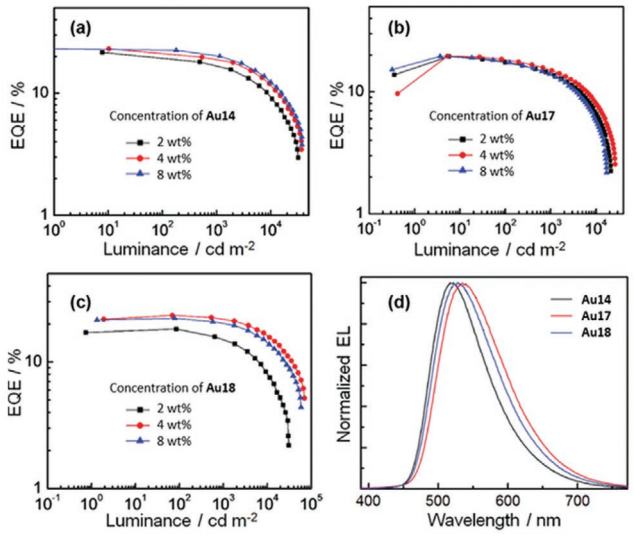

Figure 16. a–c) EQE–luminance characteristics of OLEDs based on **Au14**, **Au17**, and **Au18** with dopant concentrations of 2, 4, and 8 wt%, and d) normalized EL spectra of devices with dopant concentration of 4 wt%. Reproduced with permission.[187] Copyright 2018, Wiley-VCH.

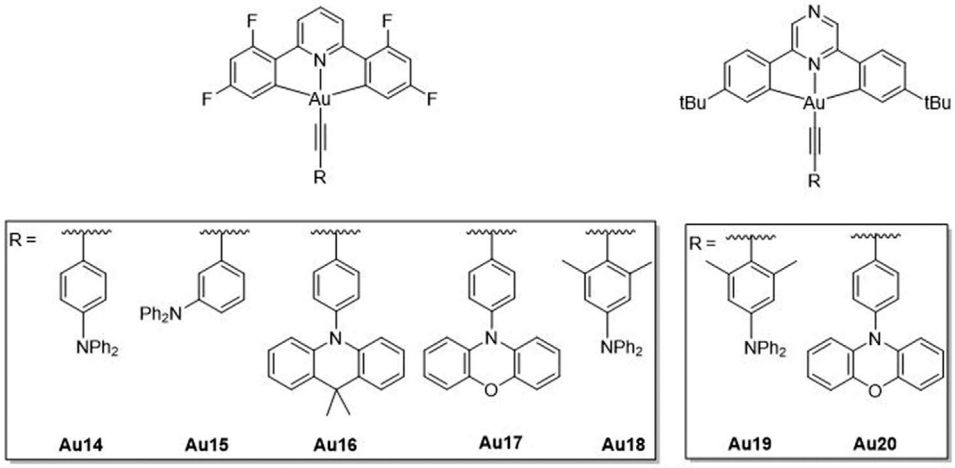

Scheme 20. Description of Au(III) complexes **Au14–20**.

This corresponds to an estimation of over 20 000 h at 100 cd m^{-2}. These devices are among the highest for Pd(II) and comparable to Pt(II) and Ir(III)-based devices.[191,193] A graphical summary of OLED devices based on d^8 Au(III) complexes is given in **Figure 18**. Pd (II) complexes are not included as only two devices were found in the literature, which makes them difficult to compare.

3. Conclusions and Outlook

During the last years, the discovery of TADF emitting transition metal complexes has become a focus of interest for both organometallic and the thin-film lighting communities. Despite the number of good reviews about purely organic TADF materials, [12,64,77,78,81,82,85] the number of reviews focusing on transition metal TADF complexes is relatively scarce. [5,12,31,77,86–89] In addition, the documents in the literature have mainly been focused on the photophysical properties of the complexes, while a comprehensive overview of device performance has been eluded. There are sections dedicated to TADF complexes in reviews about OLEDs and LECs, but in particular, transition metal TADF complexes are seen as an exotic type of devices rather than a family by themselves. In this context, this review presents the state-of-the-art of using TADF transition metal complexes in SSLDs, differentiating OLEDs and LECs.

As OLED devices based on small organic molecules are conquering the lighting market, once again it is worth to highlight the promising results of organometallic TADF emitters. For example, blue-emitting OLEDs with EQEs up to 27.5% were designed by Credgington and co-workers using gold(I) complexes,[129] while green/yellow-emitting OLEDs have reached over 23% of EQE using Cu(I)[115] and Au(I) complexes.[187] Che et al. have successfully prepared red- and white-emitting OLEDs with the highest EQEs of 10.2% and 16.8%, respectively.[113,114] Although these values are lower than those reported for organic TADF emitters—that is, EQE values of 37% for blue[65] and around 30% for green/yellow [10,66] and orange/red[67,201] (**Table 10**), they are remarkable enough to encourage new breakthroughs in the future.

As far as LECs are concerned, they still face a lack of efficiency and stability, explaining why they are still underrepresented. However, they are gathering much attention of the scientific community as these devices present several advantages, such as manufacturing cost and environmental impact. It is worth mentioning that progress has been made

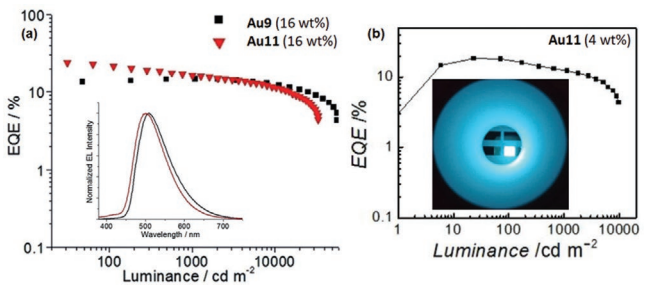

Figure 17. a) EQE versus luminance of solution-processed OLEDs based on **Au9** and **Au11** (16 wt%) using admixture of PVK and OXD-7 as host with the inset showing their EL spectra. b) EQE versus luminance of solution-processed OLEDs based on **Au11** (4 wt%) using PYD2 as host with the inset showing a photo of the device viewed from the inside the integrating sphere.[186] Copyright 2018, Wiley-VCH.

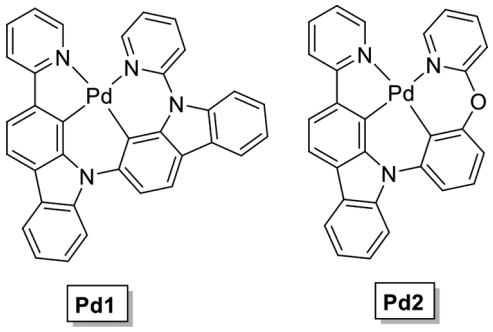

Scheme 21. Description of Pd(II) complexes **Pd1** and **Pd2**.

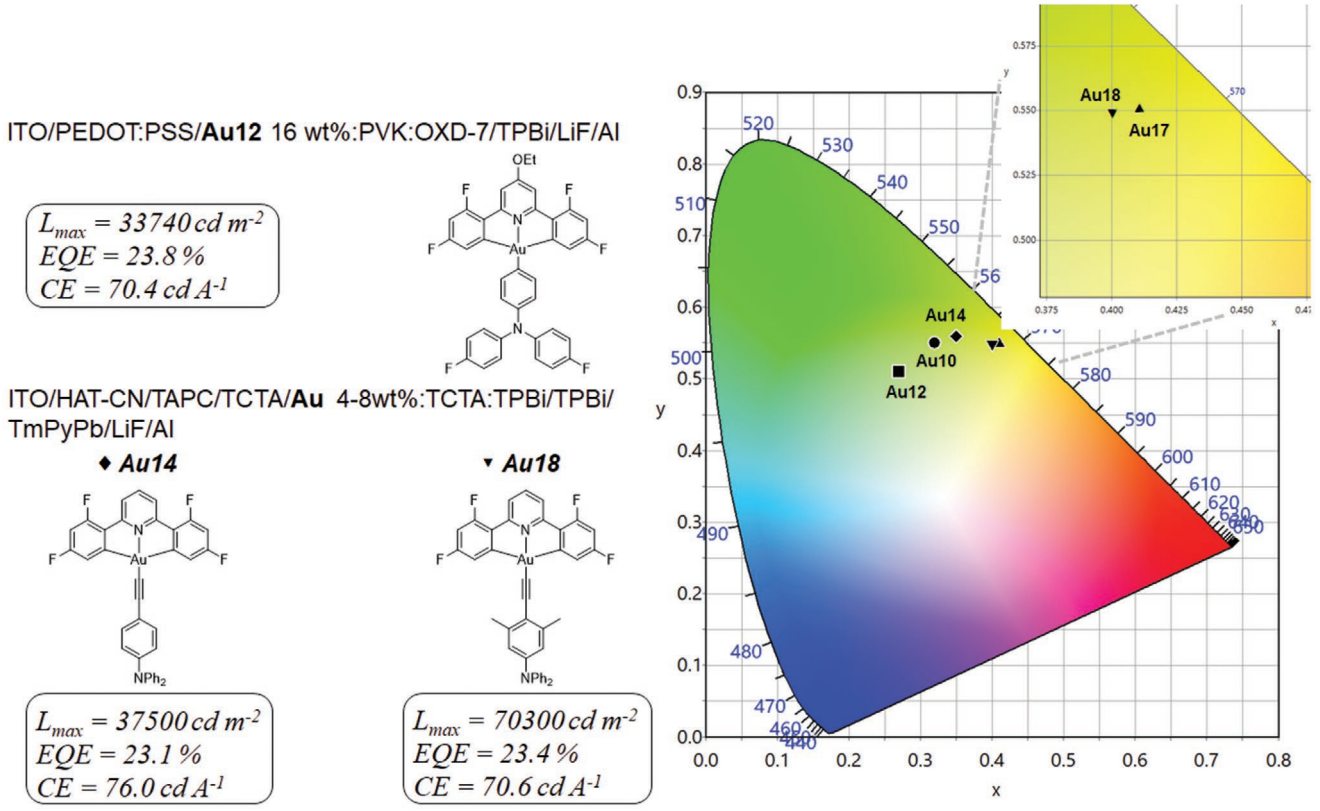

Figure 18. Graphical summary of the benchmark OLEDs devices based on Au(III) complexes; devices with highest efficiencies are represented on the left.

in this field in terms of color tuning and lifetimes, reaching moderate performances using copper(I) complexes. For instance, blue LECs have been reported with blue-emitting copper(I) complexes showing CE of 1.3 cd A^{-1} and L_{max} of 170 cd m^{-2}.[109] Other similar performances have been achieved in green/yellow-emitting LECs (CE of 3.7 cd A^{-1} and L_{max} 370 cd m^{-2})[146] and red LECs (PE of 0.23 lm W^{-1} and irradiance of 97.9 µW cm^{-2}).[150] Noteworthy, promising results have been recently reported on white-emitting LECs based on silver(I) complexes, in which the degradation mechanism involves the formation of silver nanoclusters.[163] Using a new device architecture, the device stability can be enhanced in several orders of magnitude in concert with L_{max} of 35 cd m^{-2} and CE of 0.2 cd A^{-1}.[163] Thus, this paves the way to possible breakthroughs taking into account that other organometallic TADF emitters are still unexplored in LECs. A comparative summary of best TADF LEC-based organometallics and organic TADF-emitting in blue, green/yellow, red, and white is also presented in **Table 11** for the interested reader.

All-in-all, we believe that this review would encourage researchers in both organometallic and SSLD communities to continue drawing a clear picture of the limits to be overcome. TADF transition metal complexes will, for sure, play a fundamental role in the new generation of SSLDs that will be consolidated in the near future.

Table 10. Figures of merit of best OLED devices based on organic and inorganic TADF emitters.

TADF emitter	Color	V_{on} [V]	λ_{max} [nm]	L_{max} [cd m^{-2}]	EQE [%]	CE [cd A^{-1}]	PE [lm W^{-1}]	CIE [x/y]	Ref.
Organic	Blue	2	–	–	36.7	94	98.4	0.18/0.43	[65]
Organic	Green/Yellow	–	–	–	29.6[b)]	–	–	–	[10]
Organic	Red	2.7	615	–	27.5	47.6	53.1	0.58/0.41	[201]
Organic	White	3.0	462, 572	18796	28.4/91	65.4	68.5	0.34/0.35	[202]
Inorganic	Blue	2.6	–	73100	27.5	87.1	75.1	0.24/0.42	[129,167]
Inorganic	Green/Yellow	–	–	70300	23.4	70.6	82.8	0.40/0.55	[187]
Inorganic	Red	–	631	4630	10.2	11.3	4.10	0.61/0.38	[114]
Inorganic	White	–	–	–	16.8	–	22.2	0.37/0.48	[113]

Table 11. Figures of merit of best LEC devices based on organic and inorganic TADF emitters.

TADF emitter	Color	Operating conditions	λ_{max} [nm]	L_{max} [cd m^{-2}]	t_{on} [h]	$t_{1/2}$ [h]	EQE [%]	CE [cd A^{-1}]	PE [lm W^{-1}]	CIE [x/y]	Ref.
Organic	Blue	IVL	495	700	30 s	–	–	0.65	–	–	[203]
Organic	Green/Yellow	7.4 V	580	740	<25 s	–	7.0	16	–	0.46/0.50	[204]
Organic	Red	7.4 V	618	380	<25 s	–	4.67	8	–	0.54/0.44	[204]
Organic	White	8 V	513,630	1220	30	–	–	1.8	–	0.39/0.37	[203]
Inorganic	Blue	–	497	170	–	–	–	1.3	–	0.23/0.28	[102,109]
Inorganic	Green/Yellow	100 A m^{-2}	557	370	0.02	0.82	3.70	–	–	–	[146]
Inorganic	Red	15 mA	675	97.9[a)]	–	20.9	–	–	0.23	0.66/0.32	[150]
Inorganic	White	15 mA	540	35	1.5	80	–	0.2	–	0.40/0.44	[163]

[a)]Luminance given in irradiance [μW cm^{-2}].

Acknowledgements

This work was supported by the "Ministère de la Recherche et des Nouvelles Technologies," CNRS (Centre National de la Recherche Scientifique), and the LABEX SynOrg (ANR-11-LABX-0029). The authors thank Normandie University (G.U.M.) for funding. R.D.C. acknowledges the program "Ayudas para la atracción de talento investigador – Modalidad 1 of the Consejería de Educación, Juventud y Deporte—Comunidad de Madrid with the reference number 2016-T1/IND-1463." R.D.C. acknowledges Spanish MINECO for the Ramón y Cajal program (RYC-2016-20891), the Europa Excelencia program (ERC2019-092825), the 2018 Leonardo Grant for Researchers and Cultural Creators from BBVA Foundation, and FOTOART-CM project funded by Madrid region under programme P2018/NMT-4367. J.F.-C. acknowledges the Marie Skłodowska-Curie Individual Fellowships (H2020-MSCA-IF-2017).

Conflict of Interest

The authors declare no conflict of interest.

Keywords

light-emitting electrochemical cells, organic light-emitting diodes, thermally activated delayed fluorescence, thin-film lighting, transition metal complexes

Received: February 14, 2020
Revised: April 23, 2020
Published online: June 14, 2020

[1] R. Delorme, F. Perrin, *J. Phys. Radium* **1929**, *10*, 177.
[2] G. N. Lewis, D. Lipkin, *J. Am. Chem. Soc.* **1941**, *63*, 3005.
[3] C. A. Parker, C. G. Hatchard, *Trans. Faraday Soc.* **1961**, *57*, 1894.
[4] A. Endo, M. Ogasawara, A. Takahashi, D. Yokoyama, Y. Kato, C. Adachi, *Adv. Mater.* **2009**, *21*, 4802.
[5] Y. Tao, K. Yuan, T. Chen, P. Xu, H. Li, R. Chen, C. Zheng, L. Zhang, W. Huang, *Adv. Mater.* **2014**, *26*, 7931.
[6] D. Volz, *J. Photonics Energy* **2016**, *6*, 020901.
[7] M. Y. Wong, E. Zysman-Colman, in *Light-Emitting Electrochemical Cells: Concepts, Advances and Challenges* (Ed: R. D. Costa), Springer International Publishing, Cham, Switzerland **2017**, pp. 237–266.
[8] H. Yersin, R. Czerwieniec, M. Z. Shafikov, A. F. Suleymanova, in *Highly Efficient OLEDs* (Ed: H. Yersin), Wiley-VCH, Weinheim, Germany **2018**, Ch. 1.
[9] T. J. Penfold, F. B. Dias, A. P. Monkman, *Chem. Commun.* **2018**, *54*, 3926.
[10] H. Kaji, H. Suzuki, T. Fukushima, K. Shizu, K. Suzuki, S. Kubo, T. Komino, H. Oiwa, F. Suzuki, A. Wakamiya, Y. Murata, C. Adachi, *Nat. Commun.* **2015**, *6*, 8476.
[11] W. Helfrich, W. G. Schneider, *J. Chem. Phys.* **1966**, *44*, 2902.
[12] C. Bizzarri, F. Hundemer, J. Busch, S. Bräse, *Polyhedron* **2018**, *140*, 51.
[13] H. Yersin, A. F. Rausch, R. Czerwieniec, T. Hofbeck, T. Fischer, *Coord. Chem. Rev.* **2011**, *255*, 2622.
[14] M. J. Leitl, V. A. Krylova, P. I. Djurovich, M. E. Thompson, H. Yersin, *J. Am. Chem. Soc.* **2014**, *136*, 16032.
[15] K. Masui, H. Nakanotani, C. Adachi, *Org. Electron.* **2013**, *14*, 2721.
[16] K. Sato, K. Shizu, K. Yoshimura, A. Kawada, H. Miyazaki, C. Adachi, *Phys. Rev. Lett.* **2013**, *110*, 247401.
[17] M. K. Etherington, J. Gibson, H. F. Higginbotham, T. J. Penfold, A. P. Monkman, *Nat. Commun.* **2016**, *7*.
[18] Z. E. X. Dance, S. M. Mickley, T. M. Wilson, A. B. Ricks, A. M. Scott, M. A. Ratner, M. R. Wasielewski, *J. Phys. Chem. A* **2008**, *112*, 4194.
[19] B. T. Lim, S. Okajima, A. K. Chandra, E. C. Lim, *Chem. Phys. Lett.* **1981**, *79*, 22.
[20] J. Gibson, A. P. Monkman, T. J. Penfold, *ChemPhysChem* **2016**, *17*, 2956.
[21] F. B. Dias, J. Santos, D. R. Graves, P. Data, R. S. Nobuyasu, M. A. Fox, A. S. Batsanov, T. Palmeira, M. N. Berberan-Santos, M. R. Bryce, A. P. Monkman, *Adv. Sci.* **2016**, *3*, 1600080.
[22] H. Noda, H. Nakanotani, C. Adachi, *Sci. Adv.* **2018**, *4*, eaao6910.
[23] H. Noda, X. K. Chen, H. Nakanotani, T. Hosokai, M. Miyajima, N. Notsuka, Y. Kashima, J. L. Brédas, C. Adachi, *Nat. Mater.* **2019**, *18*, 1084.
[24] S. F. A. Kettle, *Physical Inorganic Chemistry*, Vol 11, Springer, Berlin **1996**.
[25] C. Baleizão, M. N. Berberan-Santos, *J. Chem. Phys.* **2007**, *126*, 204510.
[26] H. Yersin, J. Strasser, *Coord. Chem. Rev.* **2000**, *208*, 331.
[27] C. L. Linfoot, M. J. Leitl, P. Richardson, A. F. Rausch, O. Chepelin, F. J. White, H. Yersin, N. Robertson, *Inorg. Chem.* **2014**, *53*, 10854.
[28] Z.-Q. Zhu, T. Fleetham, E. Turner, J. Li, *Adv. Mater.* **2015**, *27*, 2533.
[29] Y. Sakai, Y. Sagara, H. Nomura, N. Nakamura, Y. Suzuki, H. Miyazaki, C. Adachi, *Chem. Commun.* **2015**, *51*, 3181.
[30] X.-L. Chen, R. Yu, Q.-K. Zhang, L.-J. Zhou, X.-Y. Wu, Q. Zhang, C.-Z. Lu, *Chem. Mater.* **2013**, *25*, 3910.
[31] M. J. Leitl, D. M. Zink, A. Schinabeck, T. Baumann, D. Volz, H. Yersin, *Top. Curr. Chem.* **2016**, *374*, 25.
[32] Y. Olivier, J.-C. Sancho-Garcia, L. Muccioli, G. D'Avino, D. Beljonne, *J. Phys. Chem. Lett.* **2018**, *9*, 6149.
[33] X. K. Chen, D. Kim, J. L. Brédas, *Acc. Chem. Res.* **2018**, *51*, 2215.
[34] T. Chen, L. Zheng, J. Yuan, Z. An, R. Chen, Y. Tao, H. Li, X. Xie, W. Huang, *Sci. Rep.* **2015**, *5*, 10923.
[35] Y. Olivier, B. Yurash, L. Muccioli, G. D'avino, O. Mikhnenko, J. C. Sancho-García, C. Adachi, T.-Q. Nguyen, D. Beljonne, *Phys. Rev. Mater.* **2017**, *1*, 75602.

[36] P. De Silva, C. A. Kim, T. Zhu, T. Van Voorhis, *Chem. Mater.* **2019**, *31*, 6995.
[37] P. K. Samanta, D. Kim, V. Coropceanu, J. L. Brédas, *J. Am. Chem. Soc.* **2017**, *139*, 4042.
[38] X. Liang, Z. L. Tu, Y. X. Zheng, *Chem. – Eur. J.* **2019**, *25*, 5623.
[39] H. Uoyama, K. Goushi, K. Shizu, H. Nomura, C. Adachi, *Nature* **2012**, *492*, 234.
[40] F. B. Dias, T. J. Penfold, A. P. Monkman, *Methods Appl. Fluoresc.* **2017**, *5*, 012001.
[41] C. M. Marian, *Wiley Interdiscip. Rev.: Comput. Mol. Sci.* **2012**, *2*, 187.
[42] T. J. Penfold, E. Gindensperger, C. Daniel, C. M. Marian, *Chem. Rev.* **2018**, *118*, 6975.
[43] E. W. Evans, Y. Olivier, Y. Puttisong, W. K. Myers, T. J. H. Hele, S. M. Menke, T. H. Thomas, D. Credgington, D. Beljonne, R. H. Friend, N. C. Greenham, *J. Phys. Chem. Lett.* **2018**, *9*, 4053.
[44] I. Kim, S. O. Jeon, D. Jeong, H. Choi, W. J. Son, D. Kim, Y. M. Rhee, H. S. Lee, *J. Chem. Theory Comput.* **2020**, *16*, 621.
[45] T. Ogiwara, Y. Wakikawa, T. Ikoma, *J. Phys. Chem. A* **2015**, *119*, 3415.
[46] C. M. Marian, J. Föller, M. Kleinschmidt, M. Etinski, in *Highly Efficient OLEDs* (Ed: H. Yersin), Wiley-VCH, Weinheim, Germany **2018**, Ch. 8.
[47] R. Czerwieniec, M. J. Leitl, H. H. H. Homeier, H. Yersin, *Coord. Chem. Rev.* **2016**, *325*, 2.
[48] K. Shizu, M. Uejima, H. Nomura, T. Sato, K. Tanaka, H. Kaji, C. Adachi, *Phys. Rev. Appl.* **2015**, *3*, 014001.
[49] X. K. Chen, S. F. Zhang, J. X. Fan, A. M. Ren, *J. Phys. Chem. C* **2015**, *119*, 9728.
[50] P. L. Santos, J. S. Ward, P. Data, A. S. Batsanov, M. R. Bryce, F. B. Dias, A. P. Monkman, *J. Mater. Chem. C* **2016**, *4*, 3815.
[51] H. Sun, Z. Hu, C. Zhong, X. Chen, Z. Sun, J. L. Brédas, *J. Phys. Chem. Lett.* **2017**, *8*, 2393.
[52] T. Northey, J. Stacey, T. J. Penfold, *J. Mater. Chem. C* **2017**, *5*, 11001.
[53] J. M. Mewes, *Phys. Chem. Chem. Phys.* **2018**, *20*, 12454.
[54] G. Onida, L. Reining, A. Rubio, *Rev. Mod. Phys.* **2002**, *74*, 601.
[55] A. Dreuw, M. Head-Gordon, *Chem. Rev.* **2005**, *105*, 4009.
[56] K. Sneskov, O. Christiansen, *Wiley Interdiscip. Rev.: Comput. Mol. Sci.* **2012**, *2*, 566.
[57] A. Dreuw, M. Wormit, *Wiley Interdiscip. Rev.: Comput. Mol. Sci.* **2015**, *5*, 82.
[58] H. Lischka, D. Nachtigallová, A. J. A. Aquino, P. G. Szalay, F. Plasser, F. B. C. Machado, M. Barbatti, *Chem. Rev.* **2018**, *118*, 7293.
[59] C. A. Ullrich, *Time-Dependent Density-Functional Theory*, Oxford University Press, Oxford **2011**.
[60] T. J. Penfold, *J. Phys. Chem. C* **2015**, *119*, 13535.
[61] H. Sun, C. Zhong, J. L. Brédas, *J. Chem. Theory Comput.* **2015**, *11*, 3851.
[62] D. Hait, T. Zhu, D. P. McMahon, T. Van Voorhis, *J. Chem. Theory Comput.* **2016**, *12*, 3353.
[63] B. G. Levine, C. Ko, J. Quenneville, T. J. Martínez, *Mol. Phys.* **2006**, *104*, 1039.
[64] T. Chatterjee, K.-T. Wong, *Adv. Opt. Mater.* **2019**, *7*, 1800565.
[65] T.-A. Lin, T. Chatterjee, W.-L. Tsai, W.-K. Lee, M.-J. Wu, M. Jiao, K.-C. Pan, C.-L. Yi, C.-L. Chung, K.-T. Wong, C.-C. Wu, *Adv. Mater.* **2016**, *28*, 6976.
[66] J. W. Sun, J. H. Lee, C. K. Moon, K. H. Kim, H. Shin, J. J. Kim, *Adv. Mater.* **2014**, *26*, 5684.
[67] W. Zeng, H. Y. Lai, W. K. Lee, M. Jiao, Y. J. Shiu, C. Zhong, S. Gong, T. Zhou, G. Xie, M. Sarma, K. T. Wong, C. C. Wu, C. Yang, *Adv. Mater.* **2018**, *30*, 1704961.
[68] Q. Pei, G. Yu, C. Zhang, Y. Yang, A. J. Heeger, *Science* **1995**, *269*, 1086.
[69] Q. Pei, Y. Yang, G. Yu, C. Zhang, A. J. Heeger, *J. Am. Chem. Soc.* **1996**, *118*, 3922.
[70] E. Fresta, R. D. Costa, *J. Mater. Chem. C* **2017**, *5*, 5643.
[71] S. Keller, E. C. Constable, C. E. Housecroft, M. Neuburger, A. Prescimone, G. Longo, A. Pertegás, M. Sessolo, H. J. Bolink, *Dalton Trans.* **2014**, *43*, 16593.
[72] P. L. dos Santos, J. S. Ward, M. R. Bryce, A. P. Monkman, *J. Phys. Chem. Lett.* **2016**, *7*, 3341.
[73] T. Smith, J. Guild, *Trans. Opt. Soc.* **1931**, *33*, 73.
[74] R. Mertens, IHS: OLED TV display revenues to reach $7.5 billion in 2025, https://www.oled-info.com/ihs-oled-tv-display-revenues-reach-75-billion-2025 (accessed: September 2019).
[75] R. Mertens, LG announces its 8.5-Gen OLED TV fab in Guangzhou is now in production, https://www.oled-info.com/lg-announces-its-85-gen-oled-tv-fab-guangzhou-now-production (accessed: September 2019).
[76] J.-F. Tremblay, *The Rise of OLED Displays*, Vol. *94*, Chemical & Engineering News, Hong Kong **2016**.
[77] H. Yersin, *Highly Efficient OLEDs: Materials Based on Thermally Activated Delayed Fluorescence*, Wiley-VCH, Weinheim, Germany **2018**.
[78] Y. Liu, C. Li, Z. Ren, S. Yan, M. R. Bryce, *Nat. Rev. Mater.* **2018**, *3*, 18020.
[79] http://apps.webofknowledge.com./Search.do?product=UA&SID=D1iZUItlRxtdYD4vQpE&search_mode=GeneralSearch&prID=3f7ca059-dd6f-461a-a631-1854131fa6c9 (accessed: November 2019).
[80] L. S. Cui, S. Bin Ruan, F. Bencheikh, R. Nagata, L. Zhang, K. Inada, H. Nakanotani, L. S. Liao, C. Adachi, *Nat. Commun.* **2017**, *8*, 2250.
[81] Z. Yang, Z. Mao, Z. Xie, Y. Zhang, S. Liu, J. Zhao, J. Xu, Z. Chi, M. P. Aldred, *Chem. Soc. Rev.* **2017**, *46*, 915.
[82] M. Godumala, S. Choi, M. J. Cho, D. H. Choi, *J. Mater. Chem. C* **2019**, *7*, 2172.
[83] M. Y. Wong, G. J. Hedley, G. Xie, L. S. Kölln, I. D. W. Samuel, A. Pertegás, H. J. Bolink, E. Zysman-Colman, *Chem. Mater.* **2015**, *27*, 6535.
[84] L. Zhang, K. W. Cheah, *Sci. Rep.* **2018**, *8*, 6.
[85] L. Bergmann, D. M. Zink, S. Bräse, T. Baumann, D. Volz, *Top. Curr. Chem.* **2016**, *374*, 22.
[86] C. Bizzarri, E. Spuling, D. M. Knoll, D. Volz, S. Bräse, *Coord. Chem. Rev.* **2018**, *373*, 49.
[87] G. Li, Z.-Q. Zhu, Q. Chen, J. Li, *Org. Electron.* **2019**, *69*, 135.
[88] J. C. Lima, L. Rodríguez, *Inorganics* **2019**, *7*, 124.
[89] B. Pashaei, S. Karimi, H. Shahroosvand, P. Abbasi, M. Pilkington, A. Bartolotta, E. Fresta, J. Fernandez-Cestau, R. D. Costa, F. Bonaccorso, *Chem. Soc. Rev.* **2019**, *48*, 5033.
[90] D. Volz, M. Wallesch, C. Fléchon, M. Danz, A. Verma, J. M. Navarro, D. M. Zink, S. Bräse, T. Baumann, *Green Chem.* **2015**, *17*, 1988.
[91] O. S. Wenger, *J. Am. Chem. Soc.* **2018**, *140*, 13522.
[92] V. A. Krylova, P. I. Djurovich, B. L. Conley, R. Haiges, M. T. Whited, T. J. Williams, M. E. Thompson, *Chem. Commun.* **2014**, *50*, 7176.
[93] R. Czerwieniec, K. Kowalski, H. Yersin, *Dalton Trans.* **2013**, *42*, 9826.
[94] R. Czerwieniec, H. Yersin, *Inorg. Chem.* **2015**, *54*, 4322.
[95] J. Chen, T. Teng, J. Y. Wang, L. Kang, X. L. Chen, L. J. Xu, R. Yu, C. Z. Lu, *Eur. J. Inorg. Chem.* **2016**, *2016*, 3036.
[96] D. M. Zink, M. Bächle, T. Baumann, M. Nieger, M. Kühn, C. Wang, W. Klopper, U. Monkowius, T. Hofbeck, H. Yersin, S. Bräse, *Inorg. Chem.* **2013**, *52*, 2292.
[97] M. Wallesch, D. Volz, C. Fléchon, D. M. Zink, S. Bräse, T. Baumann, in *Organic Light Emitting Materials and Devices XVIII*, Proc. SPIE, Vol. *9183* (Eds: F. So, C. Adachi), SPIE, Bellingham, WA **2014**, p. 918309.
[98] Y. Okano, H. Ohara, A. Kobayashi, M. Yoshida, M. Kato, *Inorg. Chem.* **2016**, *55*, 5227.
[99] A. Schinabeck, M. J. Leitl, H. Yersin, *J. Phys. Chem. Lett.* **2018**, *9*, 2848.
[100] L. Bergmann, C. Braun, M. Nieger, S. Bräse, *Dalton Trans.* **2018**, *47*, 608.
[101] D. Liang, X.-L. Chen, J.-Z. Liao, J.-Y. Hu, J.-H. Jia, C.-Z. Lu, *Inorg. Chem.* **2016**, *55*, 7467.

[102] M. Elie, F. Sguerra, F. Di Meo, M. D. Weber, R. Marion, A. Grimault, J.-F. Lohier, A. Stallivieri, A. Brosseau, R. B. Pansu, J.-L. Renaud, M. Linares, M. Hamel, R. D. Costa, S. Gaillard, *ACS Appl. Mater. Interfaces* **2016**, *8*, 14678.
[103] M. Elie, M. D. Weber, F. Di Meo, F. Sguerra, J.-F. Lohier, R. B. Pansu, J.-L. Renaud, M. Hamel, M. Linares, R. D. Costa, S. Gaillard, *Chem. - Eur. J.* **2017**, *23*, 16328.
[104] S. Igawa, M. Hashimoto, I. Kawata, M. Yashima, M. Hoshino, M. Osawa, *J. Mater. Chem. C* **2013**, *1*, 542.
[105] M. Osawa, I. Kawata, R. Ishii, S. Igawa, M. Hashimoto, M. Hoshino, *J. Mater. Chem. C* **2013**, *1*, 4375.
[106] M. Osawa, M. Hoshino, M. Hashimoto, I. Kawata, S. Igawa, M. Yashima, *Dalton Trans.* **2015**, *44*, 8369.
[107] M. Osawa, M. Hashimoto, I. Kawata, M. Hoshino, *Dalton Trans.* **2017**, *46*, 12446.
[108] X.-L. Chen, C.-S. Lin, X.-Y. Wu, R. Yu, T. Teng, Q.-K. Zhang, Q. Zhang, W.-B. Yang, C.-Z. Lu, *J. Mater. Chem. C* **2015**, *3*, 1187.
[109] M. D. Weber, E. Fresta, M. Elie, M. E. Miehlich, J. L. Renaud, K. Meyer, S. Gaillard, R. D. Costa, *Adv. Funct. Mater.* **2018**, *28*, 1707423.
[110] W. Sun, Q. Zhang, L. Qin, Y. Cheng, Z. Xie, C. Lu, L. Wang, *Eur. J. Inorg. Chem.* **2010**, *2010*, 4009.
[111] Q. Zhang, J. Ding, Y. Cheng, L. Wang, Z. Xie, X. Jing, F. Wang, *Adv. Funct. Mater.* **2007**, *17*, 2983.
[112] J. Zhang, C. Duan, C. Han, H. Yang, Y. Wei, H. Xu, *Adv. Mater.* **2016**, *28*, 5975.
[113] G. Cheng, G. K. M. So, W. P. To, Y. Chen, C. C. Kwok, C. Ma, X. Guan, X. Chang, W. M. Kwok, C. M. Che, *Chem. Sci.* **2015**, *6*, 4623.
[114] G. K.-M. So, G. Cheng, J. Wang, X. Chang, C.-C. Kwok, H. Zhang, C.-M. Che, *Chem. - Asian J.* **2017**, *12*, 1490.
[115] D. Volz, Y. Chen, M. Wallesch, R. Liu, C. Fléchon, D. M. Zink, J. Friedrichs, H. Flügge, R. Steininger, J. Göttlicher, C. Heske, L. Weinhardt, S. Bräse, F. So, T. Baumann, *Adv. Mater.* **2015**, *27*, 2538.
[116] D. Volz, M. Nieger, J. Friedrichs, T. Baumann, S. Bräse, *Langmuir* **2013**, *29*, 3034.
[117] A. Verma, D. M. Zink, C. Fléchon, J. Leganés Carballo, H. Flügge, J. M. Navarro, T. Baumann, D. Volz, *Appl. Phys. A* **2016**, *122*, 191.
[118] X. Hong, B. Wang, L. Liu, X. X. Zhong, F. B. Li, L. Wang, W. Y. Wong, H. M. Qin, Y. H. Lo, *J. Lumin.* **2016**, *180*, 64.
[119] Z. Wang, J. Zhu, Z. Liu, P. Wu, H. Wang, Z. Zhang, B. Wei, *J. Mater. Chem. C* **2017**, *5*, 6982.
[120] F. Zhang, Y. Guan, X. Chen, S. Wang, D. Liang, Y. Feng, S. Chen, S. Li, Z. Li, F. Zhang, C. Lu, G. Cao, B. Zhai, *Inorg. Chem.* **2017**, *56*, 3742.
[121] L. Lin, D.-H. Chen, R. Yu, X.-L. Chen, W.-J. Zhu, D. Liang, J.-F. Chang, Q. Zhang, C.-Z. Lu, *J. Mater. Chem. C* **2017**, *5*, 4495.
[122] M. Mohankumar, M. Holler, J. F. Nierengarten, J. P. Sauvage, *Chem. - Eur. J.* **2012**, *18*, 12192.
[123] M. Mohankumar, M. Holler, M. Schmitt, J. P. Sauvage, J. F. Nierengarten, *Chem. Commun.* **2013**, *49*, 1261.
[124] M. Mohankumar, F. Monti, M. Holler, F. Niess, B. Delavaux-Nicot, N. Armaroli, J. P. Sauvage, J. F. Nierengarten, *Chem. - Eur. J.* **2014**, *20*, 12083.
[125] M. Mohankumar, M. Holler, E. Meichsner, J.-F. Nierengarten, F. Niess, J.-P. Sauvage, B. Delavaux-Nicot, E. Leoni, F. Monti, J. M. Malicka, M. Cocchi, E. Bandini, N. Armaroli, *J. Am. Chem. Soc.* **2018**, *140*, 2336.
[126] N. Armaroli, G. Accorsi, M. Holler, O. Moudam, J. F. Nierengarten, Z. Zhou, R. T. Wegh, R. Welter, *Adv. Mater.* **2006**, *18*, 1313.
[127] S. M. Kuang, D. G. Cuttell, D. R. McMillin, P. E. Fanwick, R. A. Walton, *Inorg. Chem.* **2002**, *41*, 3313.
[128] D. G. Cuttell, S.-M. Kuang, P. E. Fanwick, D. R. McMillin, R. A. Walton, *J. Am. Chem. Soc.* **2002**, *124*, 6.
[129] D. Di, A. S. Romanov, L. Yang, J. M. Richter, J. P. H. Rivett, S. Jones, T. H. Thomas, M. Abdi Jalebi, R. H. Friend, M. Linnolahti, M. Bochmann, D. Credgington, *Science* **2017**, *356*, 159.
[130] A. S. Romanov, L. Yang, S. T. E. Jones, D. Di, O. J. Morley, B. H. Drummond, A. P. M. Reponen, M. Linnolahti, D. Credgington, M. Bochmann, *Chem. Mater.* **2019**, *31*, 3613.
[131] S. Shi, M. C. Jung, C. Coburn, A. Tadle, D. M. R. Sylvinson, P. I. Djurovich, S. R. Forrest, M. E. Thompson, *J. Am. Chem. Soc.* **2019**, *141*, 3576.
[132] R. Hamze, S. Shi, S. C. Kapper, D. S. Muthiah Ravinson, L. Estergreen, M.-C. Jung, A. C. Tadle, R. Haiges, P. I. Djurovich, J. L. Peltier, R. Jazzar, G. Bertrand, S. E. Bradforth, M. E. Thompson, *J. Am. Chem. Soc.* **2019**, *141*, 8616.
[133] H. Xu, T. Yang, F. Wang, J. Zhang, X. Zhang, H. Wang, B. Xu, *J. Lumin.* **2019**, *205*, 82.
[134] L. Yang, X. Xu, P. Zhang, M. Chen, G. Chen, Y. Zheng, B. Wei, J. Zhang, *Dyes Pigm.* **2019**, *161*, 296.
[135] S. Scholz, D. Kondakov, B. Lüssem, K. Leo, *Chem. Rev.* **2015**, *115*, 8449.
[136] T. Yu, P. Zhang, Y. Zhao, H. Zhang, J. Meng, D. Fan, L. Chen, Y. Qiu, *Org. Electron.* **2010**, *11*, 41.
[137] X. Li, J. Zhang, Z. Zhao, X. Yu, P. Li, Y. Yao, Z. Liu, Q. Jin, Z. Bian, Z. Lu, C. Huang, *ACS Appl. Mater. Interfaces* **2019**, *11*, 3262.
[138] S. Keller, F. Brunner, J. M. Junquera-Hernández, A. Pertegás, M.-G. La-Placa, A. Prescimone, E. C. Constable, H. J. Bolink, E. Ortí, C. E. Housecroft, *ChemPlusChem* **2018**, *83*, 143.
[139] S. T. Parker, J. D. Slinker, M. S. Lowry, M. P. Cox, S. Bernhard, G. G. Malliaras, *Chem. Mater.* **2005**, *17*, 3187.
[140] R. D. Costa, A. Pertegás, E. Ortí, H. J. Bolink, *Chem. Mater.* **2010**, *22*, 1288.
[141] S. Keller, A. Prescimone, H. Bolink, M. Sessolo, G. Longo, L. Martínez-Sarti, J. M. Junquera-Hernández, E. C. Constable, E. Ortí, C. E. Housecroft, *Dalton Trans.* **2018**, *47*, 14263.
[142] S. Keller, A. Pertegás, G. Longo, L. Martínez, J. Cerdá, J. M. Junquera-Hernández, A. Prescimone, E. C. Constable, C. E. Housecroft, E. Ortí, H. J. Bolink, *J. Mater. Chem. C* **2016**, *4*, 3857.
[143] F. Brunner, L. Martínez-Sarti, S. Keller, A. Pertegás, A. Prescimone, E. C. Constable, H. J. Bolink, C. E. Housecroft, *Dalton Trans.* **2016**, *45*, 15180.
[144] A. M. Bünzli, H. J. Bolink, E. C. Constable, C. E. Housecroft, M. Neuburger, E. Ortí, A. Pertegás, J. A. Zampese, *Eur. J. Inorg. Chem.* **2012**, *2012*, 3780.
[145] M. Alkan-Zambada, S. Keller, L. Martínez-Sarti, A. Prescimone, J. M. Junquera-Hernández, E. C. Constable, H. J. Bolink, M. Sessolo, E. Ortí, C. E. Housecroft, *J. Mater. Chem. C* **2018**, *6*, 8460.
[146] F. Brunner, A. Babaei, A. Pertegás, J. M. Junquera-Hernández, A. Prescimone, E. C. Constable, H. J. Bolink, M. Sessolo, E. Ortí, C. E. Housecroft, *Dalton Trans.* **2019**, *48*, 446.
[147] E. Fresta, G. Volpi, M. Milanesio, C. Garino, C. Barolo, R. D. Costa, *Inorg. Chem.* **2018**, *57*, 10469.
[148] R. D. Costa, D. Tordera, E. Ortí, H. J. Bolink, J. Schönle, S. Graber, C. E. Housecroft, E. C. Constable, J. A. Zampese, *J. Mater. Chem.* **2011**, *21*, 16108.
[149] J. M. Carbonell-Vilar, E. Fresta, D. Armentano, R. D. Costa, M. Viciano-Chumillas, J. Cano, *Dalton Trans.* **2019**, *48*, 9765.
[150] E. Fresta, M. D. Weber, J. Fernandez-Cestau, R. D. Costa, *Adv. Opt. Mater.* **2019**, *7*, 1900830.
[151] C. Adachi, R. C. Kwong, P. Djurovich, V. Adamovich, M. A. Baldo, M. E. Thompson, S. R. Forrest, *Appl. Phys. Lett.* **2001**, *79*, 2082.
[152] J. Chen, T. Teng, L. Kang, X. L. Chen, X. Y. Wu, R. Yu, C. Z. Lu, *Inorg. Chem.* **2016**, *55*, 9528.
[153] M. Z. Shafikov, A. F. Suleymanova, R. Czerwieniec, H. Yersin, *Inorg. Chem.* **2017**, *56*, 13274.

[154] M. Z. Shafikov, A. F. Suleymanova, R. Czerwieniec, H. Yersin, *Chem. Mater.* **2017**, *29*, 1708.
[155] H. Yersin, M. J. Leitl, R. Czerwieniec, in *Organic Light Emitting Materials and Devices XVIII*, Proc. SPIE, Vol. *9183* (Eds: F. So, C. Adachi), SPIE, Bellingham, WA **2014**, p. 91830N.
[156] A. Belyaev, T. Eskelinen, T. M. Dau, Y. Y. Ershova, S. P. Tunik, A. S. Melnikov, P. Hirva, I. O. Koshevoy, *Chem. - Eur. J.* **2018**, *24*, 1404.
[157] G. Chakkaradhari, T. Eskelinen, C. Degbe, A. Belyaev, A. S. Melnikov, E. V. Grachova, S. P. Tunik, P. Hirva, I. O. Koshevoy, *Inorg. Chem.* **2019**, *58*, 3646.
[158] C.-W. Hsu, C.-C. Lin, M.-W. Chung, Y. Chi, G.-H. Lee, P.-T. Chou, C.-H. Chang, P.-Y. Chen, *J. Am. Chem. Soc.* **2011**, *133*, 12085.
[159] L.-J. Xu, X. Zhang, J.-Y. Wang, Z.-N. Chen, *J. Mater. Chem. C* **2016**, *4*, 1787.
[160] Y.-P. Li, X.-X. Fan, Y. Wu, X.-C. Zeng, J.-Y. Wang, Q.-H. Wei, Z.-N. Chen, *J. Mater. Chem. C* **2017**, *5*, 3072.
[161] H. X. Shu, J. Y. Wang, Q. C. Zhang, Z. N. Chen, *Inorg. Chem.* **2017**, *56*, 9461.
[162] A. S. Romanov, S. T. E. Jones, L. Yang, P. J. Conaghan, D. Di, M. Linnolahti, D. Credgington, M. Bochmann, *Adv. Opt. Mater.* **2018**, *6*, 1801347.
[163] E. Fresta, J. M. Carbonell-Vilar, J. Yu, D. Armentano, J. Cano, M. Viciano-Chumillas, R. D. Costa, *Adv. Funct. Mater.* **2019**, *29*, 1901797.
[164] R. A. Kirgan, B. P. Sullivan, D. P. Rillema, in *Photochemistry and Photophysics of Coordination Compounds II*, Topics in Current Chemistry, Vol. *281*, Springer, Berlin **2007**, pp. 45–100.
[165] W. E. Van Zyl, J. M. López-De-Luzuriaga, J. P. Fackler, *J. Mol. Struct.* **2000**, *516*, 99.
[166] S. Thompson, J. Eng, T. J. Penfold, *J. Chem. Phys.* **2018**, *149*, 014304.
[167] P. J. Conaghan, S. M. Menke, A. S. Romanov, S. T. E. Jones, A. J. Pearson, E. W. Evans, M. Bochmann, N. C. Greenham, D. Credgington, *Adv. Mater.* **2018**, *30*, 1802285.
[168] J. Föller, C. M. Marian, *J. Phys. Chem. Lett.* **2017**, *8*, 5643.
[169] Q. Zhang, D. Tsang, H. Kuwabara, Y. Hatae, B. Li, T. Takahashi, S. Y. Lee, T. Yasuda, C. Adachi, *Adv. Mater.* **2015**, *27*, 2096.
[170] A. Takahashi, C. Adachi, in *Frontiers in Optics 2005*, Tucson, Arizona, OSA Technical Digest, **2005**, p. JTuC71.
[171] E. Najafi, M. M. Amini, L. Masoomi, S. S. H. Davarani, M. Janghouri, E. Mohajerani, S. W. Ng, *J. Coord. Chem.* **2013**, *66*, 2712.
[172] E. Najafi, M. M. Amini, E. Vessally, M. Gholami, S. W. Ng, *Inorg. Chim. Acta* **2017**, *463*, 61.
[173] K. T. Yeung, W. P. To, C. Sun, G. Cheng, C. Ma, G. S. M. Tong, C. Yang, C. M. Che, *Angew. Chem., Int. Ed.* **2017**, *56*, 133.
[174] K.-T. Chan, T.-L. Lam, D. Yu, L. Du, D. L. Phillips, C.-L. Kwong, G. S. M. Tong, G. Cheng, C.-M. Che, *Angew. Chem. Int. Ed.* **2019**, *58*, 14896.
[175] C. S. Oh, J. Y. Lee, *Dyes Pigm.* **2013**, *99*, 374.
[176] M. Cibian, A. Shahalizad, F. Souissi, J. Castro, J. G. Ferreira, D. Chartrand, J. M. Nunzi, G. S. Hanan, *Eur. J. Inorg. Chem.* **2018**, *2018*, 4322.
[177] S. G. Roh, Y. H. Kim, K. D. Seo, D. H. Lee, H. K. Kim, Y. Il Park, J. W. Park, J. H. Lee, *Adv. Funct. Mater.* **2009**, *19*, 1663.
[178] Y. Hao, W. Meng, H. Xu, H. Wang, X. Liu, B. Xu, *Org. Electron.* **2011**, *12*, 136.
[179] F. Dumur, L. Beouch, M.-A. Tehfe, E. Contal, M. Lepeltier, G. Wantz, B. Graff, F. Goubard, C. R. Mayer, J. Lalevée, D. Gigmes, *Thin Solid Films* **2014**, *564*, 351.
[180] A. S. Berezin, K. A. Vinogradova, V. P. Krivopalov, E. B. Nikolaenkova, V. F. Plyusnin, A. S. Kupryakov, N. V. Pervukhina, D. Y. Naumov, M. B. Bushuev, *Chem. - Eur. J.* **2018**, *24*, 12790.
[181] H. Kunkely, A. Vogler, *J. Chem. Soc., Chem. Commun.* **1990**, *40*, 1204.
[182] F. Borbone, U. Caruso, S. Concilio, S. Nabha, B. Panunzi, S. Piotto, R. Shikler, A. Tuzi, *Eur. J. Inorg. Chem.* **2016**, *2016*, 818.
[183] J. A. do Nascimento Neto, C. C. da Silva, L. Ribeiro, G. A. Vasconcelos, B. Gontijo Vaz, V. S. Ferreira, L. H. K. Queiroz Júnior, L. J. Q. Maia, A. M. Sarotti, F. T. Martins, *New J. Chem.* **2017**, *41*, 12843.
[184] F. Dumur, *Synth. Met.* **2014**, *195*, 241.
[185] J. Fernandez-Cestau, B. Bertrand, M. Blaya, G. A. Jones, T. J. Penfold, M. Bochmann, *Chem. Commun.* **2015**, *51*, 16629.
[186] W. P. To, D. Zhou, G. S. M. Tong, G. Cheng, C. Yang, C. M. Che, *Angew. Chem., Int. Ed.* **2017**, *56*, 14036.
[187] D. Zhou, W. To, Y. Kwak, Y. Cho, G. Cheng, G. S. M. Tong, C. Che, *Adv. Sci.* **2019**, *6*, 1802297.
[188] M. A. Baldo, D. F. O'Brien, Y. You, A. Shoustikov, S. Sibley, M. E. Thompson, S. R. Forrest, *Nature* **1998**, *395*, 151.
[189] H.-X. Shu, J.-Y. Wang, Q.-C. Zhang, Z.-N. Chen, *Inorg. Chem.* **2017**, *56*, 9461.
[190] W. Zhu, L. Fan, *Dyes Pigm.* **2008**, *76*, 663.
[191] P. K. Chow, C. Ma, W. P. To, G. S. M. Tong, S. L. Lai, S. C. F. Kui, W. M. Kwok, C. M. Che, *Angew. Chem., Int. Ed.* **2013**, *52*, 11775.
[192] T. V. Esipova, H. J. Rivera-Jacquez, B. Weber, A. E. Masunov, S. A. Vinogradov, *J. Phys. Chem. A* **2017**, *121*, 6243.
[193] T. Fleetham, G. Li, J. Li, *Adv. Mater.* **2017**, *29*, 1601861.
[194] T. V. Esipova, H. J. Rivera-Jacquez, B. Weber, A. E. Masunov, S. A. Vinogradov, *J. Am. Chem. Soc.* **2016**, *138*, 15648.
[195] R. Karpicz, S. Puzinas, V. Gulbinas, A. Vakhnin, A. Kadashchuk, B. P. Rand, *Chem. Phys.* **2014**, *429*, 57.
[196] Y. Iwasaki, H. Fukagawa, T. Shimizu, *Molecules* **2019**, *24*, 454.
[197] M. Z. Shafikov, R. Daniels, P. Pander, F. B. Dias, J. A. G. Williams, V. N. Kozhevnikov, *ACS Appl. Mater. Interfaces* **2019**, *11*, 8182.
[198] J. Callis, M. Gouterman, Y. Jones, B. Henderson, *J. Mol. Spectrosc.* **1971**, *39*, 410.
[199] P. W. Zach, S. A. Freunberger, I. Klimant, S. M. Borisov, *ACS Appl. Mater. Interfaces* **2017**, *9*, 38008.
[200] Z. Abedin-Siddique, T. Ohno, K. Nozaki, T. Tsubomura, *Inorg. Chem.* **2004**, *43*, 663.
[201] X. Gong, P. Li, Y. Huang, C. Wang, C. Lu, W. Lee, C. Zhong, Z. Chen, W. Ning, C. Wu, S. Gong, C. Yang, *Adv. Funct. Mater.* **2020**, *30*, 1908839.
[202] D. Luo, Q. Chen, Y. Gao, M. Zhang, B. Liu, *ACS Energy Lett.* **2018**, *3*, 1531.
[203] J. Liu, J. Oliva, K. Tong, F. Zhao, D. Chen, Q. Pei, *Sci. Rep.* **2017**, *7*, 1524.
[204] P. Lundberg, Y. Tsuchiya, E. M. Lindh, S. Tang, C. Adachi, L. Edman, *Nat. Commun.* **2019**, *10*, 5307.